Serpentinization as a Tape Recorder of (Dis)Continuous Mantle Exhumation along the Alpine Tethys Ocean-Continent-Transition

Flora Hochscheid, Marc Ulrich, Manuel Muñoz, Philippe Boulvais, Gianreto Manatschal

Serpentinization as a tape recorder of (dis)continuous mantle exhumation along the Alpine Tethys Ocean-Continent-Transition

Flora Hochscheid[a,d*], Marc Ulrich[a], Manuel Muñoz[b], Philippe Boulvais[c], Gianreto Manatschal[a]

[a]*Institut Terre et Environnement de Strasbourg, Université de Strasbourg, CNRS UMR 7063, 5 rue Descartes, 67084 Strasbourg, France*

[b]*Géosciences Montpellier, Université de Montpellier, CNRS UMR 5243, Campus Triolet, 34095 Montpellier, France*

[c]*Géosciences Rennes, UMR-CNRS 6118, University of Rennes, Rennes, France*

[d]*Actual address: Department of Earth and Planetary Sciences, University of California, Berkeley, CA 94720, Berkeley, USA*

**corresponding author: E-mail address: fhochscheid@berkeley.edu*

ABSTRACT

Serpentinization has been widely documented and investigated at mid-ocean ridges (MOR) and subduction zones. In contrast, at magma-poor rifted margins serpentinization has received much less attention, despite its importance in controlling rheology and mass fluxes during breakup and establishing of a steady-state MOR. In this study, we present new petrological and geochemical data on subcontinental exhumed serpentinized peridotites from the spectacularly exposed Platta, Tasna and Totalp nappes in the Eastern Central Alps in SE Switzerland, belonging to the Alpine Tethys Ocean Continent Transition (OCT). The results testify of a complex history of fluid-rock interactions recorded by several serpentinization events starting with lizardite mesh and bastite textures (S1), subsequently followed by a succession of serpentine-filling veins with distinct textures and serpentine polysomes that include spherical polyhedral serpentine (S2); chrysotile ± polygonal ± lizardite banded veins (S3); lamellar antigorite veins and patches (S4) and chrysotile crack-seal (S5). The serpentinization sequence differs at proximal (i.e., continentwards) and distal (i.e., oceanwards) domains of the OCT. At proximal domains of the OCT (Upper Platta, Tasna) serpentinites record the complete serpentinization sequence (S1 to S5), whereas at distal domains (Lower Platta) serpentinization is restricted to pseudomorphic mesh and bastite (S1) and chrysotile crack-seal (S5). We attribute this discrepancy to contrasted mechanisms of mantle exhumation along the OCT. While at proximal domains mantle is unroofed along continuous and single large offset detachment faults allowing for the formation of all serpentine generations, mantle exhumation at distal domains is a more discontinuous process, controlled by sequential out-of-sequence detachment and flip-flop faults preventing the full development of all serpentine generations. In this frame, the nature and order of formation of the serpentine polysomes are directly controlled by the conditions of serpentinization (i.e., temperature, mantle composition and fluid/rock ratio).

We propose that this new conceptual model can be extrapolated to serpentinization at slow to ultra-slow MORs, where close similarities in the serpentinization sequences have been recently reported.

Keywords: *serpentinization; magma-poor rifted margin; mantle exhumation; serpentine geochemistry; fluid-rock interaction*

1. INTRODUCTION

At slow and ultra-slow spreading ridges (<40 $mm.yr^{-1}$), mantle peridotites are either exhumed at the seafloor along large offset normal faults, also referred to as detachment faults (Karson and Rona 1990; Cannat 1993; Cann et al., 1997; Lavier et al., 1999; Smith et al., 2006), or flip-flop faults (Sauter et al., 2013). Mantle exhumation at MORs is closely linked to hydrothermal activity that significantly modifies the mineralogy of mantle peridotites, turning them into serpentinites (e.g., Bonatti, 1968; Aumento et al., 1971; Früh-Green et al., 1990, 1996; Paulick et al., 2006; Bach et al., 2004, 2006; Schwarzenbach et al., 2016, 2021). The serpentinization process stores about 13 wt.% H_2O, leading to a strong volume expansion (up to ~40%, O'Hanley, 1992; Klein and Roux, 2020), and a density drop from 3.3 to 2.6 $g.cm^{-3}$. Serpentinization also results in strain localization along faults and the subsequent rapid exhumation from depths of 3-4 km to the seafloor (Raleigh and Paterson, 1965; Christensen, 1972, 2004; Escartin et al., 1997, 2001; Morrow et al., 2000; Reinen et al., 1994).

While serpentinization and mantle-fluid interactions at Mid-Ocean Ridges (MORs) were largely documented over the past two decades, at magma-poor Ocean-Continent Transitions (OCT) these processes remain less well understood, despite the ubiquity of serpentinites at these settings. The presence of serpentinites at OCTs was first proposed from the Apennines (Elter, 1969) before it has been proofed along the Iberia margin (ODP Leg 103, Boillot et al., 1980; 1989). Since then, more and more occurrences have been reported and described from present-day OCTs (Agrinier et al., 1996; Albers et al., 2021; Beslier et al., 2004; Bonatti et al., 1986; Hopkinson et al., 2004; Kodolányi et al., 2012; Nicholls et al., 1981) as well as from fossil examples (Lagabrielle and Bodinier, 2008; Manatschal and Müntener, 2009; Picazo et al., 2013). At present, it is assumed that ~50% of the world rifted margins are formed by serpentinized exhumed mantle (Minshull, 2009).

Similar to MOR settings, serpentinization plays also at OCTs a key-role during mantle exhumation (e.g., Whitmarsh et al., 2001; Gillard et al., 2019). However, the nature of the mantle strongly differs between the two settings: while lherzolites are common in OCTs, harzburgites are dominant in MORs. How far the more fertile, pyroxene-rich composition of the mantle at OCTs controls the serpentization pathways and the nature of secondary mineral phases is yet little understood and will be discussed in this paper. Previous studies have demonstrated that temperature of serpentinization also differs between OCTs and MORs. At slow spreading centers, seawater-mantle interaction takes place in the range of 200-400 °C (e.g., Barnes et al., 2009; Früh-Green et al., 2004; Vesin et al., 2024), while serpentinization at OCT is assumed to occur at T<250 °C (Agrinier et al., 1996; Schwarzenbach et al., 2013, 2016; Vesin et al., 2023). This discrepancy is mainly attributed to the presence of punctual gabbroic intrusions in the mantle section at slow spreading centers that significantly increase the local geothermal gradient that can range between 45 and 150 °C km^{-1} (Bach et al., 2011; Cannat et al., 2019). At OCTs, the volume of intrusive magma increases oceanward, suggesting that the thermal gradient increases in the same direction reaching at its oceanward termination similar conditions like those at ultraslow MORs (Cannat et al., 2009, 2019). The extent of serpentinization is likely controlled by access of seawater at depth, which is influenced by the presence or absence of magma. Low temperature of serpentinization was estimated from samples from the Iberia Abyssal Plain OCT (60-190°C, e.g., Agrinier et al., 1996; Vesin et al., 2023) and the Newfoundland OCT (100-130°C, Vesin et al., 2023). Higher temperatures of serpentinization were primary reported at the MAR (>350°, e.g., Agrinier and Cannat, 1997), but recent in-situ oxygen data in MOR serpentinites indicate lower temperatures (~290 and 115 °C; Vesin et al., 2024). These new temperatures only partly cover the range of those expected at OCTs. As the mantle composition, geothermal gradients and depths of fluid penetration differ between

OCTs and MORs, these two systems may record distinct histories of fluid-rock interaction, mass fluxes and deformation. However, to date, only very few studies looking more systematically at serpentinization reactions and sequences exist at OCTs.

The large variety of serpentine textures reported for MOR settings has been interpreted in terms of variation in the conditions and mechanisms of serpentinization, including temperature, fluid/rock ratio, fluid chemistry and/or tectonic unroofing (e.g., Andreani et al., 2007; Dilek et al., 1997; Rouméjon et al., 2015, 2019). To date, detailed investigations of serpentine textures at magma-poor OCTs remain scarce and mostly incomplete, mainly due to the limited accessibility of the exhumed mantle in present-day OCTs and the complexity of restoring remnants of fossil OCTs emplaced in collisional orogens back to their pre-orogenic position (Albers et al., 2021; Tichadou et al., 2021).

In this study we investigate serpentinized peridotites from the Jurassic OCT of the Alpine Tethys realm now exposed in the southeastern Swiss Alps. We discuss the serpentine textures in terms of fluid/rock ratio, fluid chemical composition, mass fluxes and temperature conditions, and integrate the importance of tectonic modes during the exhumation of subcontinental mantle at the seafloor. We propose a conceptual model to explain serpentinization sequences at OCTs and discuss how our results can reconcile observations made at MORs.

2. GEOLOGICAL SETTING

Remnants of the Jurassic OCT of the Alpine Tethys are exposed as so called ophiolitic nappes in the Central Alps in southeastern Switzerland (Figure 1A and C; Manatschal and Nievergelt, 1997; Müntener et al., 2004, 2010). They represent remnants of the Adriatic-European conjugate margins (Figure 1B; Florineth and Froitzheim, 1994; Manatschal, 2004). In our study, we focus on three sites, the Platta and Totalp nappes, both deriving from

142 the SE OCT of the Adriatic margin, and the Tasna nappe, which derives from the conjugate
143 European margin (Manatschal and Müntener, 2009; Figure 1).

144

145 **2.1. The Platta nappe**

146 The Platta nappe belongs to the lower Austro-Alpine and South Pennine nappe stack that
147 was emplaced during Late Cretaceous along top to the NW thrust faults (Figure 1C). The
148 Platta nappe is subdivided into two units separated by a main reactivated pre-Alpine shear
149 zone (Figure 1D; Epin et al., 2019). The Upper Platta Unit, in the hanging wall, was
150 originally located in a more proximal position in the OCT (Figure 1D). This unit consists of
151 mantle rocks (the Upper Serpentinite Unit; Figure 2A) derived from the inherited
152 subcontinental Adriatic mantle (i.e., Schaltegger et al., 2002; Müntener et al., 2004, 2010;
153 Picazo et al., 2016; Epin et al., 2019). The Lower Platta Unit, in the footwall of the main
154 shear zone, was originally located in a more distal position (Figure 1D). This unit consists of
155 a large mantle domain (i.e., the Lower Serpentinite Unit, Figure 2A) locally intruded by
156 gabbros dated at 161 ±1 Ma (Schaltegger et al., 2002) and covered by lavas of late Middle to
157 early Late Jurassic age (165 to ~155 Ma; Desmurs et al., 2001; Amann et al., 2020).
158 Contrarily to peridotites from the Upper Platta Unit that are almost free from any syn-
159 exhumation melt imprint and equilibrated at ~920 °C, peridotites from the Lower Platta Unit
160 have been largely percolated by MORB-type melts during final rifting and breakup, leading
161 to a significantly higher equilibrium temperature of 1100 ± 50 °C (Müntener et al., 2010).
162 Slivers of continental origin also occur in the Platta nappe and have been interpreted as
163 extensional allochthons (Froitzheim and Manatschal, 1996). Mantle rocks in the Platta nappe
164 display ophicalcites at their contact with mafic rocks and deep-water sediments (Figure 2C;
165 Dietrich, 1970, Coltat et al., 2021), and were weakly affected by Alpine metamorphism
166 (lower greenschist facies, <350°C; Trommsdorff and Evans, 1974, Frey and Mählmann,

1999, Coltat et al., 2021b). However, an increase in Alpine metamorphism from north to south is documented by the transition from lizardite-chrysotile to antigorite. In the northern Platta nappe, temperatures were assumed to remain below 150°C, whereas in the Malenco nappe, south of the Engadine line, temperatures reached up to 400°C (Figure 1C; Dietrich, 1969; Trommsdorff and Evans, 1977; Trommsdorff, 1983; Burkhard and O'Neil, 1988; Vils et al., 2011).

2.2. The Totalp nappe

The Totalp nappe is located to the north of the Platta nappe (Figure 1B). It belongs to the Late Cretaceous Upper Austro-Alpine and South Pennine nappe stack that was thrust northward over the Middle and Lower Pennine units during the late Eocene, (Froitzheim and Manatschal, 1996; Figure 1C). The slightly more complex polyphase Alpine tectonic overprint makes that its position in the former OCT is less well defined than that of the Platta nappe. However, there is consensus in admitting that the Totalp nappe is derived from the SE OCT of the Alpine Tethys (Weissert and Bernoulli, 1985). The Totalp nappe consists of serpentinized spinel lherzolites, locally containing pyroxenites and ophicalcites, resulting from the carbonation of serpentine under static conditions at the seafloor. The ophicalcites preserve depositional contacts with Upper Jurassic to Lower Cretaceous pelagic sediments (Figure 3; Picazo et al., 2013). Magmatic rocks are very rare and mainly consist of flaser gabbros and dolerite dykes (Peters and Mathews, 1963). The Alpine metamorphic overprint is below prehnite pumpellyite facies at around 250°C (Peters, 1965). Serpentinized mantle is often crosscut by calcite veins, and similarly to the Platta nappe, relics of the pre-Alpine contacts between exhumed mantle rocks, ophicalcites and deep-water sediments are locally well-preserved (Weissert and Bernoulli, 1985; Bernoulli and Weissert, 1985; Picazo et al., 2013). Results from $^{40}Ar/^{39}Ar$ dating on phlogopite from pyroxenites gave a cooling

192 temperature ≤300°C and exhumation age of 160 ± 8 Ma (Peters and Stettler, 1987a,b).

193

194 **2.3. The Tasna nappe**

195 The Tasna nappe was derived from the European OCT (Figure 1B; Florineth and
196 Froitzheim, 1994; Manatschal et al., 2006; Ribes et al., 2019). It belongs to the Tertiary
197 Alpine nappe stack made of Austro-Alpine and Pennine units (Figure 1C) emplaced during
198 the Eocene to Oligocene (Ribes et al., 2019). As for the Platta and Total nappes, the Tasna
199 nappe exposes primary contacts between exhumed and serpentinized mantle rocks and
200 sediments (Figure 3). The Alpine metamorphism did not exceed 350°C (greenschist facies;
201 Florineth and Froitzheim, 1994; Bousquet et al., 2008). The Tasna nappe is made of a wedge
202 of continental crust separated from the underlying mantle by a detachment fault, referred to
203 as the Lower Tasna Detachment (LTD; Froitzheim and Rubatto, 1998, Figure 4C). The
204 Upper Tasna Detachment (UTD) is the top-basement fault responsible for the exhumation of
205 the crust and mantle rocks at the seafloor (Froitzheim and Rubatto, 1998, Manatschal et al.,
206 2004, 2006). It is overlain by the undeformed post-rift sediments (Figure 4C) interpreted as
207 Upper Jurassic (Ribes et al., 2019). Mantle rocks consist of highly serpentinized spinel
208 lherzolites with abundant spinel websterite layers and preserving a high temperature
209 foliation marked by spinel grains (Manatschal et al., 2006). The $^{40}Ar/^{39}Ar$ dating of
210 phlogopite provides an age of 170.5 ± 0.4 Ma (Manatschal et al., 2006), similar to that
211 obtained for mantle exhumation at Totalp (160 ± 8 Ma; Peters and Stettler, 1987a). The
212 clinopyroxene compositions and the calculated equilibrium temperatures of mantle
213 peridotites from Tasna are similar to those from the Upper Platta unit and Totalp,
214 demonstrating that all of these ultramafic units belonged to the same, inherited mantle
215 domain (Manatschal et al., 2006; Picazo et al., 2016).

216

3. MATERIALS AND METHODS

3.1. Sampling and analytical strategies

A total of 40 moderately to completely serpentinized peridotites have been sampled (Table 1). The sampling was done with the aim of characterizing fluid-rock interactions at the two opposed positions along the OCT of the former Alpine Tethys, i.e., at the proximal domain (continentwards, Upper Platta, Tasna and Totalp) and the distal domain (oceanwards, Lower Platta; Figure 1D). A comprehensive set of petrographical and geochemical analyzes was performed on each sample, including: i) petrographic observations in thin sections; ii) X-ray diffraction, to identify minerals and their respective proportions in serpentinites; iii) bulk-rock major and trace element analyses. Among the samples, 18 were selected for: i) Raman spectroscopy to identify serpentine polysomes, and ii) in situ major and trace element analyses to constrain fluid-rock interactions during mantle exhumation.

3.2. X-Ray Diffraction

XRD analyses were performed on sample powders using a Bruker D8 advance Eco diffractometer at the Institut Terre et Environnement de Strasbourg (ITES, University of Strasbourg). A large X-ray beam was emitted by a copper source with a 40 kV accelerating voltage and a 25 mA current. Intensities were recorded at 0.014° 2θ step intervals from 3 to 80° 2θ, with a dwell time of 0.8 s. Size of the divergence slit was 0.4°. Table 1 provides the quantitative mineralogical compositions determined by Rietveld refinement using Profex-BGMN software (Doebelin and Kleeberg 2015), as well as the list of the reference structures used for refinement. The diffraction patterns, Rietveld refinements and the references of mineral structures used for the refinements are given in supplementary materials.

3.3. Raman spectroscopy

Raman spectra were acquired on 30 µm thick polished thin sections, using a HORIBA LabRAM ARAMIS spectrometer at the Laboratoire des sciences de l'ingénieur, de l'informatique et de l'imagerie (ICube, University of Strasbourg). A 100x objective (Olympus) and a 632 nm (Ar+) laser at 9 mW were used, resulting in a laser spot size of ~1 µm. All analyses were performed using integration times of 15 or 30 s to optimize the signal/noise ratio. Raman spectra were recorded in two wavelength intervals: 100-1120 cm^{-1} for structural bonding characterization and 3500-3750 cm^{-1} for the characterization of hydroxyl bonds. The serpentine polysomes were identified by comparison with reference spectra taken from the literature, in particular on the stretching range of the OH groups (e.g., Auzende et al., 2004; Groppo et al., 2006; Tarling et al., 2018; Compagnoni et al., 2021).

3.4. Bulk-rock chemistry

The major element concentrations were measured on pressed pellets of calcined powder (i.e. after loss on ignition) using a micro-X-ray fluorescence (µ-XRF) Bruker M4 Tornado at ITES. For each sample, 10 measurements were performed at random location on each pellet to ensure the reproducibility at the pellet surface. A collimated Rh source operating at 700 µA with an accelerating voltage of 50 kV was used, resulting in a 1 mm spot-size in diameter at the sample surface. Two energy-dispersive silicon drift detectors of 125 eV resolution, and with an active area of 60 mm^2 each were used to measure fluorescence spectra (300 s counting time per spectrum). Measurements were performed in a vacuum chamber at 2 mbar to minimize air absorption and ensure the best signal/noise ratio.

The bulk-rock trace element concentrations were determined at ITES using an Inductively Coupled Plasma Mass Spectrometry (ICP-MS) Thermo Scientific X series II instrument and ICAP RQ Thermo Scientific instrument. The analytical procedure was adapted from the method of Chauvel et al., (2011): about 100 mg of rock powder was

267 precisely weighed and dissolved in Savillex beakers in a HF-HNO_3-$HClO_4$ (5:1:1) mixture,
268 during a minimum of 7 days at 140 °C on a hot plate. The solution was then evaporated, and
269 the residue was taken in a 3:1 3M HCl-H_3BO_3 mixture for 12 hours in a hot plate at 90 °C to
270 avoid any fluoride precipitation. This mixture was then evaporated and further dissolved in
271 concentrated HNO_3. After another evaporation, the residue was finally diluted in 40 ml of 7
272 M HNO_3.

273 Analyzes performed on international standard are consistent with preferred reference
274 values from GeoREM for UB-N serpentinite (Govindaraju, 1982). Differences between
275 reference values from the literature and our analyses of UB-N are ±1.1% for all other major
276 oxides except for Na_2O, K_2O, P_2O_5 and TiO_2 which are present in very low concentrations.
277 For most trace element concentration, the deviation from the reference value of UB-N is in
278 average ±5% (See Supplementary Table 3).

279

280 **3.5. Mineral chemistry**

281 The major element concentrations were measured on 30 μm-thick polished sections using a
282 µ-XRF Bruker M4 Tornado at ITES. Measurements were performed using a Rh anode
283 operating at 400 µA with an accelerating voltage of 50 kV. Polycapillary lenses were used to
284 focus the X-ray beam down to 20 µm full-width-at-half-maximum at the sample surface.
285 The counting time per point was set to 180 s. µ-XRF spectra were calibrated after repeated
286 analyses of Smithsonian National Museum of Natural History mineral standards
287 (Jarosewich, et al., 1980) of diopside (NMNH 117733) and San Carlos olivine (NMNH
288 111312-44), and some in-house mineral standards of clinochlore, chrysotile and antigorite.
289 Total Fe content was calculated on a divalent basis, as FeO_{tot}.

290 The structural formulae for lizardite, chrysotile, polygonal and polyhedral

serpentines was calculated on the basis of 7 oxygens. Antigorite has a distinct formula $Mg_{3m-3}Si_{2m}O_{5m}(OH)_{4m-6}$ that slightly differs from the idealized serpentine formula ($Mg_3SiO_5(OH)_4$), where m is the number of tetrahedra along an entire wavelength of the crystalline structure. Here, the structural formula of antigorite was calculated based on m = 17 (Mellini et al., 1987). The Fe^{2+} and Fe^{3+} contents of serpentine mineral were estimated following the approach of Ulrich et al., (2020) based on the initial study of Beard and Frost (2017). The calculations assume a full dioctahedral substitution, i.e., ferric iron is accommodated in the serpentine by substitution for divalent cation plus the addition of a vacancy in the octahedral sheet.

Serpentine trace element compositions were acquired on 30 µm polished thin sections by laser ablation inductively coupled plasma mass spectrometry (LA-ICP-MS) at Géosciences Montpellier (University of Montpellier, AETE regional facility of the OSU OREME). The instrument includes a pulsed 193 nm ArF excimer laser (Compex 102 instrument from LambdaPhysik) coupled to a ThermoScientific Element XR mass spectrometer. Laser ablation was performed with an energy density of 12 J/cm^2 at a frequency of 6 Hz. Few laser pulses with a spot size of 130 μm were applied before each ablation to clean up the sample surface. Then each acquisition was performed with a total of 240 pulses with a spot size of 110 μm, sufficient to obtain a long and stable signal for integration. The ablated material was transported using a constant He flow of 1 l/min and mixed with Ar flow of 0.6 l/min in a cyclone coaxial mixer before entering the ICP torch and being ionized. The ions are then sampled, accelerated and focused before being separated and analyzed in the mass spectrometer. ^{29}Si content known from prior μ-XRF analyses were used as internal standard and concentrations were calibrated against the NIST 612 rhyolitic glass using reference values from Pearce et al., 1997. In order to evaluate the precision of the measurements the reference basalt glass BIR-1G was analyzed repeatedly

316 each 5 samples to (the complete dataset, including standard reference values, is available in
317 supplementary materials). Data reduction was operated with Matlab-based SILLS program
318 (Guillong et al., 2008), following the standard methods of Pettke et al. (2012). Detection
319 limits were between 1 ppb and <0.3 ppm for most trace elements.
320
321 **4. RESULTS**
322 **4.1. Petrographic description**
323 All samples analyzed in this study derived from the proximal domain (Tasna, Totalp and
324 Upper Platta) are spinel-lherzolites, while those from the distal domain (Lower Platta) are
325 dominantly plagioclase-bearing lherzolites. Macroscopically, all samples are extensively
326 serpentinized (Figure 5). This is confirmed by microscopic observations (Figure 6) and
327 Rietveld refinements made on X-Ray diffraction patterns (Table 1), showing that most of the
328 samples contain ~96% (n=40) serpentine. Rare exceptions were found at Tasna and mostly
329 Totalp, where relics of primary clinopyroxene and more occasionally olivine are preserved.
330 The serpentinites from the Lower and Upper Platta nappe are typically of a dark
331 green color (Massive serpentinite; Figure 5A). Serpentinites from the Lower Platta, display
332 rare imprint of several serpentine veins. Some serpentinites contain clasts of massive dark
333 serpentinite that are locally embedded in a fibrous and light-green colored serpentine matrix
334 (Figure 5B). For the Upper Platta (proximal domain) serpentinites are occasionally crosscut
335 by centimeter-thick light green serpentine veins (Figure 5A), and most samples are
336 characterized by several generations of serpentine veins (Figure 5C). At Tasna (Figure 5D,
337 E) and Totalp (Figure 5F), massive serpentinites are locally surrounded by a late foliated
338 serpentinite, characterized by a light blueish color and a fibrous aspect. At Totalp, some
339 relics of primary minerals are present, like olivine in the center of mesh texture (Figure 5G)
340 or clinopyroxene in massive dark serpentinite (Figure 5H). It should be noted that some

samples contain minute amounts of calcite (<1 %, Table 1) when picked up in the vicinity of ophicalcites (e.g., Picazo et al., 2013).

Based on microscopic observations and Raman spectra made on thin sections, we firstly described the textures and determined the polysomes of serpentine. Secondly, we attributed the succession of serpentine to a sequential evolution regarding the position along the OCT, i.e., proximal and distal domains.

4.1.1. Serpentine mesh and bastite textures S1

Serpentine mesh and bastite textures constitute the bulk and first generation of serpentinization in most samples from all domains. They correspond to the pseudomorphic replacement of olivine and pyroxenes by serpentine mesh (Figure 6 A, B) and bastite textures (Figure 6 C, D). Some relics of primary minerals, especially clinopyroxene and to a lesser extent olivine, can be occasionally preserved in samples from Totalp (Figure 6B, E). In these samples, olivine is preserved within the mesh network and hydration of clinopyroxene has progressed with the development of serpentine veins along cleavages. Orthopyroxene relicts are scarcely observed in our samples, at the opposite of spinel grains which are preserved even in the most serpentinized samples and only show minor evidence of hydrothermal alteration with the local formation of chlorite aureoles. The dominant serpentine polysome is lizardite, as shown by the typical OH stretching bands at 3685 cm^{-1} and 3707 cm^{-1} on Raman spectra (Figure 6). In all these samples, magnetite is ubiquitous, with amounts between 0.38 and 5% (Table 1). Magnetite mainly occurs as small grains (<5 µm) disseminated along the mesh rims, and also observed in cleavages and surrounding the bastite grains (Figures 5 and 6C).

4.1.2. Serpentine veins

366 The background mesh and bastite textures (S1, lizardite type) are usually crosscut by at least
367 one generation of serpentine veins in the distal domain, and usually several generations of
368 serpentine veins in the proximal domain. We have identified four main generations of
369 serpentine veins representing a serpentinization sequence.

370

371 *Spherical serpentine (S2):* The second generation of serpentine, here referred to as "spherical
372 serpentine S2", was occasionally observed in partially serpentinized samples from Totalp and
373 Tasna and barely in fully serpentinized samples from Upper Platta. It forms a typical spherical
374 texture that is characterized in microscopic view in crossed-polarized light by an extinction
375 cross in the polarization directions (Figure 6 E, F, H). Such typical spherical texture and the
376 Raman signature (Figure 6) are robust features in favor of a polyhedral serpentine. This
377 serpentine polysome occurs in a few of our samples, mainly in clinopyroxene cleavages
378 (Figure 6E, F) and occasionally as veins crosscutting the previous serpentine mesh and bastite
379 S1 (Figure 6H). The occurrence of small andradite grains (~10 µm diameter) is closely
380 associated to polyhedral serpentine veins, almost exclusively at the vicinity of clinopyroxenes
381 (Figure 6F, H).

382

383 *Banded veins (S3):* The third generation of serpentine (S3, Figure 6G), is usually observed in
384 serpentinites from proximal domains and very sparsely and rarely in serpentinites from the
385 distal part (Lower Platta). It consists of veins ranging from tens of µm- to cm-thick. The
386 centimetric veins are observable at the macroscopic scale and are characterized by a fibrous
387 green texture (e.g., Figure 5A). These veins are made of finely spaced bands of low
388 birefringence that alternate between white and black colors under the cross-polarized light
389 (Figure 6G, H). All bands are parallel to each other and mimic the irregular shape of the vein
390 margins, preserving the initial geometry of the fracture. The Raman spectra shows that

391 serpentine polysomes filling these banded veins are diverse. Although recent studies have
392 shown that the distinction between lizardite and polygonal serpentine is not obvious using
393 Raman spectroscopy (Tarling et al., 2018, Compagnoni et al., 2021). Based on the Raman
394 spectra, most of the banded veins exhibiting the typical OH stretching bands at 3685 cm^{-1}
395 and 3707 cm^{-1} are filled by lizardite. Other spectra showing two peaks at 3692 cm^{-1} and
396 3700 cm^{-1} (Figure 6) rather correspond to polygonal serpentine, whereas only rare
397 occurrences of chrysotile were observed (main peaks at 3689 cm^{-1} and 3699 cm^{-1}).
398
399 *Lamellar veins (S4):* The fourth generation of serpentine (S4) is exclusively observed at
400 Tasna and Upper Platta (proximal domains). Only one has been observed in a sample from
401 Lower Platta (distal domain) and none from Totalp (proximal domain). It consists of
402 disoriented serpentine lamellae with a first order grey to pale yellow birefringence under the
403 cross-polarized light. It occurs mostly as veins crosscutting the pseudomorphic mesh and
404 bastite and serpentine veins, which are highlighted by magnetite grains at the serpentine vein
405 rims (Figure 7). Lamellar veins are typically between 50 and 150 µm-thick, but they can also
406 form large patches interconnected by veins of the same textures (Figure 7). Lamellar veins
407 appear to spread within the mesh textures, resulting in blurred rims (Figure 7D). The Raman
408 spectral signature indicates that these lamellar veins are made of a mixture of antigorite and
409 chrysotile, with peaks at 3670 $cm^{-1,}$ 3690 $cm^{-1}$and 3700 cm^{-1} (Figure 7). Occasionally, some
410 of these veins and patches display an additional peak at 3685 cm^{-1}, which likely indicates the
411 local presence of small lizardite grains. Some carbonates, identified as calcite, are
412 occasionally observed inside some of these lamellar veins (Figure 7C).
413
414 *Fibrous veins (S5):* The last generation of serpentine (S5) is systematically observed in
415 samples from Lower Platta and regularly observed in the other units. It forms crack-seal

structures characterized by lens-shape extending along several mm-long and tens of µm width (Figure 7 D). This serpentine polysome displays a typical fibrous aspect. The fibers are preferentially oriented perpendicular to the vein edge and are characterized by a high birefringence under cross-polarized light. The characteristic shoulder at 3690 cm^{-1} preceding a peak at 3701 cm^{-1} matches the Raman spectral signature of chrysotile in high wavelength domain (Figure 7D).

To sum up, the different serpentine textures and polysomes described in this section are presented as an evolutionary sequence, comprised of five stages of serpentinization (Figure 8).

4.2. Bulk-rock geochemistry

Most samples show typical concentrations of SiO_2 and MgO for serpentinites (41.33 wt.% and 38.96 wt.% in average, respectively; Figure 9). They cover a wide range of concentrations in CaO (0.04-4.1 wt.%) and Al_2O_3 (0.21-7.73 wt.%). The presence of clinopyroxene and/or plagioclase in the samples can explain the high CaO measured in bulk, while higher Al_2O_3 content attests of the presence of spinel or plagioclase. Figure 10 presents the MgO/SiO_2 and Al_2O_3/SiO_2 ratios of serpentinites from Totalp, Tasna, Upper and Lower Platta (Hart and Zindler, 1986; Jagoutz et al., 1979). The serpentinized peridotites plot along the terrestrial mantle array. Most samples display fertile compositions (Al_2O_3/SiO_2 >0.05) while only few samples derive from a refractory protolith. Mg# is around 0.94 for most serpentinites (Figure 10), close to the Mg# values of initial peridotites (Müntener et al., 2010). Ni and Cr concentrations are mainly in the range 1500-2500 µg/g and 2000-3500 µg/g, respectively (Figure 11). Interestingly, samples with abundant veining are characterized by high Mg# (up to 0.96, corresponding to samples with low FeO_{tot}, <5 wt.%; Figures 8 and 10) and very low Cr and Ni concentrations (<500 µg/g Table 2; Figure

11).

Bulk-rock serpentinites normalized to Chondrite-C1 display homogeneous patterns, characterized by flat Heavy to Middle rare earth elements (REE) with relatively fertile compositions with $HREE_N$ >2 and depletion in Light (L)REE ($(La/Sm)_N$ = 0.80, in average n=40; Figure 12). Some samples from Tasna and Platta differ from the overall trends by highly depleted HREE concentrations ($HREE_N$ ~0.1-1 C1-Chondrite; Figure 12) and positive Eu anomalies (Eu/Eu* = 1.41 in average, n=40). Spider diagrams show enrichment in fluid mobile elements (FME), as highlighted by positive anomalies in Cs, B and Li. Locally, a slight enrichment in U is observed (up to 10 times PM in Tasna serpentinites), Pb and Sr (0.1-1 time PM in Upper and Lower Platta and Tasna serpentinites).

4.3. Serpentine geochemistry

4.3.1. Major elements

In average, serpentine mesh contains 40.91 wt% SiO_2 (Si = 1.91 apfu), 1.40 wt% Al_2O_3 (Al = 0.08 apfu), 38.87 wt% MgO (Mg = 2.74 apfu) and 5.30 wt% FeO_{tot} (Fe_{tot} = 0.21 apfu), giving a Mg# of ~0.93. Bastite texture slightly differs in composition relative to mesh texture, with less SiO_2 (39.81 wt%; Si = 1.9 apfu), MgO (37.49 wt%; Mg = 2.6 apfu) and FeO_{tot} (4.74 wt%; Fe_{tot} = 0.18 apfu) and more Al_2O_3 (4.12 wt%; Al = 0.23 apfu), because they retain part of Al from primary pyroxene (Table 3). Consequently, serpentine mesh plots close to the Mg-pure lizardite or chrysotile end-members in the Si versus Mg+Fe diagram (Figure 13A), whereas bastite composition extends along the Tschermak trend (Al replacing an octahedral and tetrahedral cation; Figure 13A, B). Bastite has Mg# near identical to mesh textures (0.94 in average, Table 3; Figure 14).

The polyhedral serpentine (S2) is generally characterized by lower FeO_{tot} content (4.19 wt%, Fe_{tot} ~0.16 apfu) at given SiO_2 and MgO concentrations relative to serpentine

466 mesh (S1; 3A). As a consequence, this second generation of serpentine has higher Mg#
467 values (>0.94 in average; Figure 14). It is also characterized by relatively high Al_2O_3
468 concentrations (2.84 wt%, Al = 0.16 apfu) and thus plots between mesh and bastite
469 serpentines along the Tschermak trend (Figure 13A, B).

470 The banded serpentine veins (S3) mainly plot within the field defined by serpentine
471 mesh (S1) in the Si versus Mg+Fe diagram (Figure 13C, Table 3). However, these banded
472 veins can be distinguished by higher Mg# values (>0.95 Table 3, Figure 14) due to lower
473 Fe_{tot} content relative to the two previous generations. More specifically, the banded veins
474 can be subdivided into two groups based on their Mg# and Raman signature (Figures 14 and
475 15): the first group made of polygonal serpentine is characterized by Mg# of ~0.95 (Fe_{tot} =
476 0.07-0.28 apfu, Mg = 2.6-2.8 apfu), whereas the second group made of lizardite has Mg#
477 >0.97 (Fe_{tot} <0.10 apfu, Mg = 2.7-2.9 apfu). The banded veins also contain Al apfu higher
478 than the serpentine mesh S1 at a given Si apfu (Al ~0.1 versus ~0.05, respectively at Si
479 ~1.95 apfu). Some veins even extend along the Tschermak trend towards the bastite field
480 (Figure 13C, D).

481 The lamellar antigorite veins and patches (S4) display the highest SiO_2 concentrations
482 of all serpentine generations (42.48 ± 1.08 wt%, Si = 1.99 apfu), and Mg+Fe in the range of
483 9.79-2.93, close to the pure antigorite end-member (Figure 13C). Interestingly, unlike the
484 gradual increase in Mg# described in previous generations of serpentine from the initial mesh,
485 antigorite veins have lower Mg# (<0.95 in average) due to higher Fe concentrations (FeO_{tot} =
486 4.15 wt% in average, Fe_{tot} = 0.16 apfu, Figure 14). Al_2O_3 concentrations are low (1.15 ± 1.07
487 wt.%, Al = 0.06 apfu).

488 The last generation of serpentine veins (crack-seal filled by chrysotile; S5) have
489 Mg+Fe content within the range of previous generations of serpentine veins, with
490 nevertheless slightly higher MgO = 39.76 ± 0.97 wt.% and lower FeO_{tot} = 3.99 ± 1.18 wt.%

concentrations (Mg = 2.79 apfu, Fe_{tot} = 0.16 apfu, Mg# = 0.95; Figures 13C and 14). They also show very similar SiO_2 and Al_2O_3 concentrations to those of the antigorite (SiO_2 = 42.17 ± 0.94 wt.%, Si = 1.98 apfu; Al_2O_3 = 0.76 ± 0.62 wt.%, Al = 0.04 apfu; Figure 13D).

Interestingly, none of the serpentine composition plots along the brucite trend (Figure 13). This is consistent with the fact that brucite was never observed in our samples, neither on microscopic observations nor through the different techniques used (i.e. XRD and Raman spectroscopy).

4.3.2. Trace elements

The representative trace element concentrations of each serpentine generation are given in Table 4, Figures 16 and 17. REE and spider diagrams of all samples analyzed in this study are given in supplementary materials. The REE concentrations of serpentine polysomes (Figures 16 and 17) vary between 0.001 and <10 times the chondrite C1 and mimic the REE pattern of their respective bulk-rocks. They are similar in shape and concentration to exhumed mantle peridotites from other places in the Alps (e.g., the Chenaillet unit, Lafay et al., 2017). At sample scale, the REE patterns of the diverse serpentine polysomes are similar in shape: LREE-depleted ($(La/Sm)_N$ ~0.35), with relatively flat middle (MREE) to HREE patterns. Noteworthy a progressive depletion from the first to the last serpentine generation is documented. Two samples from the Lower and Upper Platta units exhibit very different REE concentrations, both forming a U-shaped pattern characterized by enrichment of LREE and HREE over MREE and strong positive Eu anomalies (Eu/Eu*>2; Figures 16 and 17).

At sample scale, the primitive mantle-normalized patterns of serpentine minerals and veins exhibit similar shapes, with a global depletion relative to the PM. As for concentrations in bulk-rock, all serpentines are enriched in FME with positive anomalies in Cs, B, As, Sr and Li (concentrations between 0.1 and >100 times the PM; Figures 16 and 17). Additionally, a significant enrichment in U relative to Th is observed (U/Th = 14.84 in

516 average; N = 183).

517

518 **5. DISCUSSION**

519 In this study, we report a sequence of four stages of serpentinization with distinct five
520 serpentine textures and specific chemical compositions (Figure 8). These stages are likely
521 indicative of a variety of fluid-rock interactions during mantle exhumation along the OCT of
522 the Alpine Tethys. In the following, we first discuss each of the serpentinization stages in
523 terms of local variations of temperature, pressure, fluid/rock ratio and fluid chemistry with
524 the aim to determine the variation of fluid-rock interactions from initial to more advance
525 mantle exhumation, recorded from proximal to distal parts across the OCT (Figure 19).
526 Finally, we compare serpentinization sequences as documented at OCTs with
527 serpentinization sequences observed at present-day MORs.

528

529 **5.1. Serpentinization as a tape recorder of multi-stage mantle exhumation**

530 *5.1.1. Stage 1: Formation of mesh and bastite textures (serpentine S1)*

531 Pseudomorphic serpentine mesh and bastite textures, here referred to as serpentine S1
532 (Figure 8), are not only the oldest, but also the most common textures found in serpentinites
533 from OCTs. Previous studies proposed that serpentinization at magma-poor rifted margins
534 likely begins when the subcontinental lithospheric mantle is still capped by a thin, <6 km
535 thick hyperextended continental crust (Manatschal, 2004; Epin et al., 2019; Hochscheid et
536 al., 2022). Serpentinizing fluids at OCTs are assumed to reach down to ~6 km depth below
537 seafloor through circulation along high-angle normal faults, as indicated by refraction
538 seismic experiments (Boddupalli et al., 2022). At such depth, a combination of anisotropic
539 thermal contraction and tectonic stresses induce micro-fractures into the mantle rocks
540 allowing the channeling of fluids necessary for serpentinization (Rouméjon and Cannat,

2014). These micro-fractures are at the origin of a connected porosity allowing the transport of hydrothermal fluids resulting in a typical mesh texture even at low fluid/rock ratio (<F/R mass ratio 1; e.g., Moody, 1976; Wicks and Whittaker, 1977; Rouméjon and Cannat, 2014). This is evidenced by trace element patterns that mimic those of the primary minerals showing lower trace element concentrations (Figure 16D, H). In addition, compared to mineral precursor serpentine minerals are also enriched in up to several orders of magnitude in FME (Cs, B, Li, ± Rb), evidencing an imprint of oceanic hydration. The FME enrichments in serpentine minerals from the Alpine OCT are similar to those of serpentinites from the Iberia and Newfoundland rifted margins (Kodolányi et al., 2012; Vesin et al., 2023). Experimental studies have shown that the hydrolysis of olivine is optimal at temperature <300 °C, whereas orthopyroxene react faster than olivine at greater temperatures (Martin and Fyfe, 1970; Janecky and Seyfried, 1986; Allen and Seyfried, 2003; Bach et al., 2004). In our partially serpentinized samples from Totalp and Tasna, relics of clinopyroxene are preserved in both units, olivine relics are frequently observed at Totalp while it is rarely preserved in other units (Figure 6). Similar observations were also reported by Müntener et al., (2010) for serpentinized peridotites from Upper and Lower Platta, where some relics of clinopyroxene were observed while olivine is completely serpentinized. In addition, spinel is almost free of chlorite aureoles, indicating low temperatures of serpentinization as the alteration of spinel to chlorite typically occurs at temperature above 400°C. Therefore, based on petrological evidence and the temperatures of serpentinization estimated for Iberia-Newfoundland passive margins and the Mid-Atlantic Ridge (15°20'N Fracture zone and Hess Deep; see Vesin et al., (2024) and references therein), we propose that an uppermost temperature limit of ±300 °C can be assumed for this initial stage of serpentinization.

5.1.2. Stage 2: Serpentine veining (serpentine S2 and S3)

Formation of polyhedral serpentine veins (S2): The first generation of veins coincides with the formation of polyhedral serpentine (S2, Figure 8) that exhibits a typical spherical texture (Figure 6). These veins are mainly located in clinopyroxene relics and bastite cleavages, where a systematic association with andradite grains is reported. The S2 veins mostly occur in partially serpentinized samples, especially at Totalp, while in fully serpentinized samples S2 veins are scarce. The polyhedral serpentine (S2) veins contain significant Al (~0.16 apfu in average; Table 3). Such Al enrichment together with precipitation of andradite are consistent with the alteration of Al-rich mineral phases like clinopyroxene. Spinel and plagioclase are also important Al carriers in peridotites but the textural vicinity of polyhedral serpentine-andradite assemblage with clinopyroxene rather indicates that the latter is the source of Al. In addition, hydrothermal alteration turns spinel into ferritchromite rims and chlorite aureoles, where all Al released from spinel is consumed by the formation of chlorite (e.g., Mellini et al., 2005). Similarly, in plagioclase lherzolite from the Lower Platta unit, Al derived from plagioclase is consumed by the formation of chlorite as evidenced by petrographic observations (e.g., Müntener et al., 2010). Most trace element concentrations are significantly depleted (except for boron) in polyhedral S2 veins showing 1 to 2 orders of magnitude lower concentrations relative to bastite (S1) and primary clinopyroxene precursors (Figure 16D, H). This suggests a high fluid/rock ratio. Therefore, it is likely that the saturation degree of the serpentinizing fluids forming polyhedral S2 veins is low. Our results agree with Andreani et al., (2008), who proposed that the formation of polyhedral serpentine veins require: (i) an open space, (ii) a temperature <200-300 °C, and (iii) Al content > 0.1 apfu.

Relatively to bastite (S1), polyhedral serpentine (S2) veins are enriched in Si and Mg and depleted in Ca and Fe (Figure 13; Table 3). This may be explained by the preferential absorption of Ca and Fe by andradite (Plümper et al., 2014). The absence of magnetite

associated to polyhedral serpentine (S2) veins is thus likely a consequence of andradite formation, since andradite consumes the Fe that is released either during pyroxenes serpentinization or after magnetite dissolution. Plümper et al., (2014) assume that andradite forms as a consequence of a Ca-metasomatism process in which the addition of Ca, here likely released after clinopyroxene serpentinization, destabilizes the magnetite. In addition, the oxidation of Fe for incorporation into andradite likely contributes to decrease fO_2, as proposed by Beard et al., (2000) in serpentinites from Hole 1068 (Abyssal Plain). This lowered fO_2 likely affects the stability of magnetite, which allow proposing that magnetite dissolution in favor to andradite resulted from both processes. Plümper et al., (2014) also showed that no additional source of Ca is required if the protolith contains between 8 and 12% of clinopyroxene. The subcontinental mantle exposed in the Platta, Tasna and Totalp nappes was originally composed of fertile, i.e., clinopyroxene-rich lherzolites (Müntener et al., 2010). Therefore, it is likely that serpentinization of these spinel or plagioclase lherzolites released enough Ca and Fe to form andradite synchronously with polyhedral serpentine. According to Frost and Beard (2007), the andradite + serpentine assemblage is strongly dependent on silica and calcium activities and on pH rather than temperature. However, these authors claim that a temperature range of 200-230 °C is most favorable for the formation of andradite, which becomes the main Ca-bearing phase in serpentinites as long as CO_2 activity remains low, inhibiting the formation of calcite (Béard et al., 2000; Kodolànyi et al., 2012). This temperature range is consistent with that reported by Plümper et al., (2014), who showed that clinopyroxene can be replaced by an assemblage of serpentine + andradite at temperatures <280 °C and low pressure (<0.5 kbar). As mentioned above, andradite is systematically observed at the rims of polyhedral serpentine, the latter mostly occurring in clinopyroxene and cpx-bastite cleavages (Figure 6F, G).

Considering that serpentine S1 formed at ±300 °C and at ≤6 km depth, serpentine S2

most likely formed shallower and under lower temperature (± <280 °C, and <5 km). The presence of andradite closely associated to polyhedral serpentine (S2) is indicative for reducing conditions as iron oxidation prior incorporation into andradite keeps fO_2 of the serpentinizing fluid relatively low and can be accompanied by considerable generation of molecular hydrogen (Plümper et al., 2014). Even if textural and chemical evidence suggests that polyhedral serpentine (S2) formed under slightly lower temperatures than serpentine S1, serpentine S2 is nevertheless assumed to develop during an early stage of fluid-rock interaction, likely soon after or simultaneously to pseudomorphic mesh and bastite S1 formation (Figure 19B – S2).

Formation of banded veins (S3): Banded veins S3 are frequently observed crosscutting the previous serpentine generations (S1 and S2 Figure 6, Table 1). Similar occurrences of banded veins have been reported in oceanic serpentinites (e.g., Andreani et al., 2004, 2007; Rouméjon et al., 2015). The nature of the filling serpentine polysomes, however, can evolve from an unstable (proto-serpentine, chrysotile, polygonal) to a more stable serpentine polymorph (lizardite) as suggested by experimental studies of Grauby et al., (1998) and Normand et al., (2002) and recently strengthened by Raman spectroscopy on naturals samples (Tarling et al., 2021). At sufficient degree of supersaturation (i.e., open system), several metastable phases like chrysotile may crystallize (Normand et al., 2002). However, if the degree of supersaturation of the fluid is not maintained sufficiently high, the transition from a metastable to a more stable form (i.e., chrysotile -> polygonal -> lizardite) can occur spontaneously (Viti and Mellini, 1997; Normand et al., 2002).

In our samples, banded veins (S3) are mostly made of lizardite and polygonal serpentine, whereas chrysotile remains scarce. The banded veins made of polygonal serpentine contains more Fe_{tot} and less Mg than banded veins made of lizardite (Figure 14).

Therefore, we attribute this isochemical evolution to the decreasing degree of supersaturation of the solution with respect to serpentine in a response to an increase of fluid/rock ratios, and a longer interaction time with the serpentinizing fluid as proposed by Normand et al., (2002) and Andreani et al., (2007). This is also supported by lower concentrations of most trace elements compared to the primary mesh and bastite S1, accompanied by an increase in FME like B (Figure 16). According to Andreani et al., (2007), we propose that the formation of these banded veins (S3) begins when the ultramafic rocks are almost fully serpentinized, at shallower depth than the first two serpentine generations (S1 and S2), likely at <3 km depth along a detachment fault (Gillard et al., 2019). At this point, there is not enough results to discriminate if the banded veins attested of crack opening due to: i) an accommodation of volume expansion due to serpentinization, or ii) the incremental stress release during unroofing of serpentinites (e.g., Ramsay, 1980; O'Hanley, 1992; Andreani et al., 2004).

5.1.3. Stage 3: Local overpressure and/or SiO_2-rich fluid circulation – formation of antigorite (S4)

Antigorite (S4) was identified in some fully serpentinized samples from Upper Platta, Tasna and in one sample from Lower Platta. It mostly occurs as patches, replacing the mesh texture, or as veins opening in all directions (Figure 7A). Locally, these veins opened in pull-apart mode, showing a close relation with small chrysotile fibers (Figure 7B). This is highlighted by the Raman spectra signature of antigorite (S4), which is systematically a mixture between serpentine chrysotile and antigorite, with typical peaks at 3670 cm^{-1}, 3690 cm^{-1} and 3700 cm^{-1} (Figure 7). In addition, antigorite (S4) is frequently crosscut by later chrysotile crack-seal (S5) (Figure 7D). Those antigorite veins may have been initially filled with chrysotile, suggesting the replacement of the latter by the former. Such replacement

666 was also documented in samples from MORs (Hébert et al., 1990; Kodolànyi et al., 2012;
667 Klein et al., 2017; Ribeiro Da Costa et al., 2008; Rouméjon et al., 2015, 2019) and the
668 Guatemala forearc (Kodolànyi and Pettke, 2011). In Alpine ophiolites, antigorite is mostly
669 considered as a fingerprint of Alpine prograde metamorphism (Dietrich, 1969; Burkhard and
670 O'Neil, 1988; Scambelluri et al., 1995; Früh-Green et al., 2001; Debret et al., 2013; Lafay et
671 al., 2013; Piccardo, 2013; Liu et al., 2020), and was, for long time, considered to be an
672 evidence of HT-HP conditions of formation of serpentine (e.g., Ulmer and Trommsdorff,
673 1995; Wunder et al., 1997; Evans, 2004). Thus, high fluid-rock interaction temperatures and
674 an additional heat source linked to melt emplacement (e.g., Béard et al., 2009; Frassi et al.,
675 2022) have been invoked to explain antigorite at spreading ridges. However, neither
676 evidence for the former nor the latter have been found at the Tasna and Upper Platta. At both
677 units, where antigorite is observed, magmatic additions are extremely rare and are not
678 observed in the vicinity of the sample locations. In contrast, at lower Platta, where numerous
679 gabbroic bodies and mafic dikes intruded the mantle, antigorite is absent, except of one
680 sample. Therefore, the antigorite formation in our samples can hardly be attributed to the
681 heat released by melt intrusions.

682 Alternatively, antigorite occurrences at Hess Deep (East Pacific Rise; Rouméjon et
683 al., 2019), Atlantis Massif (Mid-Atlantic Ridge, MAR; Rouméjon et al., 2018, 2019), Puerto
684 Rico Trench (Klein et al., 2017) and the Southwest Indian Ridge (SWIR; Rouméjon et al.,
685 2015) were explained by interaction of the predating serpentine with Si-rich hydrothermal
686 fluids derived from the alteration of mafic bodies (dikes and gabbros) or pyroxenes. Linking
687 the antigorite formation to Si-metasomatism of mafic magmatic additions is hardly
688 reconciled with observations and data from Tasna and Upper Platta, since such rocks are not
689 observed in the field. However, peridotites from both Tasna and Upper Platta are pyroxene-
690 rich, and at both sites pyroxenes are largely replaced by serpentine (Figure 6). Therefore, the

691 silica released after pyroxene alteration may have contributed to the formation of antigorite,
692 which is consistent with the fact that some samples plot below the peridotite melting residue
693 line in Figure 10. Kodolànyi and Pettke (2011) provided a detailed study on the major role
694 played by SiO_2 during the chrysotile to antigorite transition. The authors suggest that if no
695 brucite is produced during antigorite formation, either SiO_2 addition or Mg and Fe removal
696 are needed to balance antigorite growth at the expense of chrysotile. This can explain the
697 absence of brucite in our samples. Another hypothesis is that the chrysotile/lizardite-to-
698 antigorite transition is linked to deformation or fluid infiltration. Ribeiro Da Costa et al.,
699 (2008) argued that chrysotile could be replaced by antigorite through a dissolution-
700 recrystallization process favored by intense shearing stress at relatively low temperatures
701 (<300 °C). Alternatively, Kodolànyi and Pettke (2011) proposed also that the replacement of
702 chrysotile by antigorite occurred by dissolution (and precipitation) at T~300 °C due to fluid
703 infiltration (i.e., fluid-assisted chrysotile-antigorite transition). The recent discovery of
704 seismic events in the footwall of oceanic core complexes showing compressional focal
705 mechanisms (Parnell-Turner et al., 2017) may reflect a small amount of shortening due to
706 the plate unbending at very shallow levels along an exhumed detachment fault (see also
707 model of Sandiford et al., 2021). Therefore, we can barely exclude that local shortening
708 during unbending of the downward concave detachment resulting in local overpressure did
709 not affect the replacement of lizardite/chrysotile by antigorite, although we agree that this
710 transition is rather promoted by (SiO_2-rich) fluid circulation.

711 The transition from oceanic serpentine to antigorite formed in subduction zones is
712 accompanied by a strong mobility of some trace elements, in particular fluid mobile
713 elements (FME) like B, Li, Cs and Sr (e.g., Deschamps et al., 2012; Peters et al., 2017,
714 Pettke and Bretscher, 2022). A loss of such elements was documented in several places in
715 the Alps, such as the Lanzo Massif (Debret et al., 2013) or the Piedmont zone (Chenaillet –

716 Queyras – Montviso; Lafay et al., 2013) of the Western Alps. These elements are transferred
717 to the mantle wedge during the lizardite to antigorite transition. The ophiolitic nappes in
718 Eastern Switzerland and Northern Italy, i.e., Totalp, Platta and Malenco discussed here
719 (Figure 1C), recorded a prograde and increasing Alpine metamorphism from north to south
720 (Peters and Mathews, 1963; Dietrich, 1969, 1970; Vils et al., 2011). These units remained,
721 however, in the hanging wall of the subduction zone and were not subducted, preserving
722 them from high P-T conditions. This suggests that Alpine serpentinization, if it existed in
723 any of these units, remained rare (Manatschal and Müntener, 2006; Picazo et al., 2013). This
724 may explain why antigorite from Upper Platta and Tasna displays no depletion in FME in
725 contrast to the subducted serpentinites, and why it shows concentrations of B, Li, Cs and Sr
726 within the range of earlier serpentines (S1 to S3; Figure 18). In addition, the shapes of the
727 antigorite spider-diagrams are also comparable to patterns of serpentine mesh within a
728 sample, albeit with an order of magnitude of depletion (Figures 16 and 17).

729 These results are much in favor of a formation of the antigorite by recrystallization of
730 earlier serpentine generations during mantle exhumation, promoted by SiO_2-rich fluid
731 circulation, as stated above, rather than a subduction-derived origin. This recrystallization
732 may be accompanied by magnetite dissolution, which could explain why magnetite is so
733 scarce in association with antigorite (Figure 7A). Based on constant Mg# measured in
734 serpentine mesh and antigorite in abyssal peridotites, Rouméjon et al., (2019) postulated that
735 antigorite does not integrate additional iron, even if magnetite is dissolved with mesh.
736 However, a constant increase in Mg# is observed in our samples from S1 to S3 (Figure 14),
737 while Mg# decreases in antigorite (S4), suggesting that slight amount of iron may be
738 integrated in antigorite veins and patches during serpentine mesh recrystallization.

739

740 *5.1.4. Stage 4: Stress relaxation – formation of crack-seal (S5)*

Chrysotile crack-seal (S5) are the last generation of serpentine veins and are ubiquitous in our samples. They are also commonly recognized as the latest serpentinization event during mantle exhumation at MORs (e.g., Andreani et al., 2007; Rouméjon et al., 2015, 2018). Evans (2004) proposed that formation of cross-fiber chrysotile (i.e., crack-seal S5) is not really different from slip-fiber chrysotile (i.e., banded veins S3), although the latter is promoted by the presence of fluids rather than shear stress. We propose that the formation of chrysotile crack-seal (S5) occurred mainly at shallower depths than banded veins, but probably in similar levels than antigorite (S4). They are certainly formed as the consequence of late strain release during mantle exhumation at seafloor.

5.2. Serpentine REE compositions: evidence of fluid-dominated systems

Serpentine REE compositions mostly reflect those of their magmatic mineral precursors (olivine, clinopyroxene and orthopyroxene; see Figures 16 and 17 and supplementary materials). Regarding the REE compositions of serpentinite whole rocks, they cover the range of peridotite compositions reported by Müntener et al. (2010). The variation of the $(La/Sm)_N$ ratio from primitive-like to highly-depleted signatures is due to variable degrees of partial melting or refertilization by syn-rift melt percolation (case of Lower Platta peridotites). It is a pre-serpentinization feature, consistently with what was documented along the Iberia passive margin (Kodolányi et al., 2012; Vesin et al., 2023). Hence, REE contents of serpentinite samples are inherited from the magmatic processes that affected the subcontinental mantle prior its exhumation at seafloor. Interestingly, two samples from the Lower and the Upper Platta units show particular U-shaped REE patterns with a strong positive Eu anomaly (Figure 17). Similar patterns were reported in oceanic serpentinites, and two main processes have been proposed in the literature: i) plagioclase crystallization during melt percolation (i.e., refertilization process; Müntener et al., 2004, 2010; Rampone et al.,

766 1998, 2020); or ii) large fluid-fluxes during serpentinization (Paulick et al., 2006).
767 Regarding the first assumption, the crystallization of melt-derived plagioclase could be
768 consistent with the formation of LREE-enriched serpentinites in the Lower Platta unit since
769 the latter was largely impregnated by melts during Jurassic rifting (Müntener et al., 2004).
770 However, this explanation cannot account for serpentinites from the Upper Platta, since this
771 unit remained preserved from syn-rift melt percolation (Müntener et al., 2010). Therefore,
772 serpentinization was likely responsible of the U-shape REE pattern which, by comparison,
773 resembles those black smokers (e.g., Rainbow and Logatchev, Figure 17; Klinkhammer et
774 al., 1994; Douville et al., 2002). Paulick et al., (2006) proposed that such shapes in
775 serpentines are only possible under very high fluid/rock ratios so that the LREE
776 concentration is entirely controlled by the fluid, erasing the LREE-depleted character of the
777 protolith. At the opposite, HREE are less affected since their concentrations in hydrothermal
778 fluids are negligible relative to the initial peridotite. Accordingly, the U-shape patterns
779 observed in two serpentinites may resulted from intense fluid-rock interactions, similar to
780 some mature hydrothermal systems described along MOR (Paulick et al., 2006). This
781 inference is consistent with the recent discovery of a well-preserved fossil ultramafic-hosted
782 hydrothermal system, namely the Marmorera-Cotschen hydrothermal system in the Lower
783 Platta unit (i.e., distal domain; Coltat et al., 2019, 2021; Hochscheid et al., 2022).
784
785 **5.3. Serpentinization across the OCT**
786 *5.3.1. Contrasting serpentinization from proximal to distal domains in the OCT*
787 An important result of this study is that the full sequence of all serpentine generations (S1 to
788 S5) is only observed in the proximal part of the OCT at Upper Platta and Tasna (Figure
789 19C). In contrast, at the Lower Platta, which is derived from a more distal part of the OCT,
790 only serpentine (S1) and chrysotile crack-seal (S5) can be observed (Figure 19C).

Interestingly, serpentinites from the Chenaillet unit, which is interpreted to be located more oceanward (distal) than the Lower Platta unit (see Figure 1D), is dominated by mesh ± bastite textures (S1) and devoid of serpentine veins (Schwartz et al., 2013; Lafay et al., 2013). This suggests that intensity of veining in serpentinites decreases oceanwards. Possible controlling factors are: i) mantle composition, which changes from proximal to distal from spinel to plagioclase lherzolites (Müntener et al., 2004, 2010), and ii) thermal gradients and presence of magma, which increase from proximal to distal. Both may account for a different rheology of the serpentinized basement and different composition of secondary minerals (e.g., Klein et al., 2013). Likewise, local magmatic intrusions could potentially increase the temperature of serpentinization and change the serpentinization rates (e.g., Rimstidt et al., 2012) and thus the degree of serpentinization at the distal domain. However, there is no difference in mineralogy nor degree of serpentinization between samples from the proximal and distal OCT, allowing us to propose that mantle composition and temperature seem not to be the main factors controlling the presence of serpentine generations. Alternatively, intensity of veining and the occurrence of serpentine generations (S1 to S5) may be linked to the mechanism of mantle exhumation. Indeed, Sauter et al., (2013), Epin et al., (2018, 2019), Reston (2018), and Gillard et al., (2019) showed that mantle exhumation processes differ from proximal to distal domains of the OCT and at MORs. While at proximal OCTs mantle exhumation is mainly controlled by large offset detachment faults, at distal domains fault offsets tend to decrease and a transition to out-of-sequence detachments, and flip-flop faulting is observed. As a consequence, in the proximal domain (e.g., Tasna and Upper Platta) continuous mantle exhumation sequences, favor the development of all serpentine generations S1 to. In contrast, sequential flip-flop faulting or out of sequence detachment faulting at distal domains (i.e., Lower Platta) have the tendency to omit the development of intermediary serpentine generations (S2, S3 S4), allowing solely the

development of the initial (S1) and final (S5) serpentine generations (Figure 19B). It is therefore conceivable that the local absence of the intermediate serpentine (S2 to S4) at more distal domains (e.g., Chenaillet; proto-oceanic domain, Figure 1D) reflects the involvement of flip-flop detachment faults (i.e., flip-flop exhumation mode, Figure 19A). This is also in line with the studies of Reston et al., (2011), Epin et al., (2019), Gillard et al., (2019), and Theunissen et al., (2022) showing evidence that mantle exhumation processes are undoubtedly more complex and discontinuous at distal parts of OCTs. Our simple model shown in Figure 19 proposes that occurrence of all serpentine generations S1 to S5 indicates exhumation along one single exhumation fault, while complicated, polyphase flip-flop systems have the tendency to omit intermediate generations (S2 to S4).

Exceptions to this model may exist. At Totalp, that belongs to the proximal OCT, not all serpentine generations are observed. The mantle rocks in this unit are particularly well preserved, displaying serpentinization degrees ~60 %. This is expected to occur for peridotites located near a fossil hydration front, in a rock-dominated hydration system. Serpentines consist essentially of lizardite in pseudomorphic mesh and bastite (S1), polyhedral serpentine (S2) inside orthopyroxene cleavages and few banded veins (S3). The low degree of serpentinization may also indicate that only small amounts of fluid penetrated the mantle, which could explain the absence of some serpentine generations (S3 to S5, Figure 19C). Limited fluid-rock interactions at Totalp are also evidenced by very low FME concentrations (except B, Sb and Li) in bulk rock (Figure 11).

5.3.2. Serpentinization at OCT and MOR: similarities and differences

Mantle exhumation is a common process at slow and ultra-slow spreading centers and at OCTs of magma-poor rifted margins (e.g., Cannat, 1993; Blackman et al., 2002; Cannat et al., 2009; Sauter et al., 2013). Recent studies have proposed that at ultra-slow MOR settings,

841 mantle exhumation involves successive detachment faults (flip-flop model; Sauter et al.,
842 2013 along the SWIR) similarly to distal parts of OCTs (e.g., Iberia-Newfoundland; Reston
843 et al., 2011, Theunissen et al., 2022), Australia-Antarctica (Gillard et al., 2016) and Lower
844 Platta (Epin et al., 2019). In contrast to ultra-slow spreading systems and distal OCTs, at
845 slow spreading MORs and proximal OCTs flip-flop detachment systems have not so far
846 been identified (Cannat et al., 2019; Epin et al., 2019).

847 Similarities in hydrothermal processes and conditions of serpentinization at slow to
848 ultra-slow MORs and OCT are suggested by the occurrence of similar serpentine polysomes.
849 Studies at 30°N (Atlantis massif; Rouméjon et al., 2018), 23°N (the Kane fracture zone,
850 MARK area Dilek et al., 1997; Andreani et al., 2007), and along the (slow) MAR, at 62-
851 65°E, as well as along the SWIR corresponding to a magma-poor end-member of an ultra-
852 slow MOR (Rouméjon and Cannat, 2014; Rouméjon et al., 2015) show similarities with
853 observations made at serpentinites from the Iberian OCT (Alt, 1993; Agrinier et al., 1996;
854 Beard and Hopkinson, 2000, Kodolànyi et al., 2012; Vesin et al., 2023). All studies revealed
855 that serpentinites recorded multiple serpentinization events, involving a large variety of
856 serpentine veins, textures and polysomes. However, the proportion, morphology and texture
857 of serpentine veins can differ depending on the setting. Along the SWIR 62-65°E and the
858 Atlantis Massif (hole M0076B; Rouméjon et al., 2015, 2018) described very similar
859 serpentine sequences with the same serpentine polysomes to those reported at proximal OCT
860 domains (Upper Platta, Tasna) reported in this study. This supports the idea that the presence
861 or absence of serpentine generations are not controlled by the conditions of serpentinization
862 (temperature and composition of mantle peridotites) but more likely by the mechanisms of
863 mantle exhumation, i.e., exhumation along a single large offset fault vs along flip-flop faults
864 (see model in Figure 19). This is also supported by observations made along the SWIR,
865 where mantle exhumation occurred during the past 7-10 Myr by flip-flop faulting (Sauter et

al., 2013). As predicted by our model, only a minor part (~25%) of the analyzed samples are overprinted by several serpentine veins (Rouméjon et al., 2015, 2018) with most of the samples composed only by pseudomorphic mesh and bastite textures (S1). Similar observations were also reported from the Atlantis Massif (Rouméjon et al., 2015, 2018).

5.3.3. Polyhedral serpentine: a fingerprint of OCTs?

A substantial difference between OCTs and MORs is the composition of the peridotites undergoing serpentinization. The nature of mantle constituting the OCT typically consists of spinel and plagioclase lherzolites, while at MORs the mantle is mostly harzburgitic (e.g., Andreani et al., 2007; Rouméjon et al., 2018). One notable difference in the serpentine paragenesis between OCT and MOR settings is the occurrence of polyhedral serpentine. In our samples, polyhedral serpentine occurs either in veins crosscutting the mesh texture or in alteration of pyroxenes, while it was not reported in Atlantis massif serpentinites and expected to occur rarely (<15 %) in latest serpentine veins at SWIR (Rouméjon et al., 2015, 2018). In serpentinites from MARK, however, serpentine polyhedral is described as the latest generation of veins (Andreani et al., 2007; 2008). According to Andreani et al., (2008), all Fe in polyhedral serpentine is ferrous, which is in favor of a formation under reducing conditions. This is therefore more consistent with a formation at depth rather than close to the seafloor, where oxidizing conditions are more likely. Its close association with andradite, as reported above, is also in favor of reducing conditions (Plümper et al., 2014).

The reason why polyhedral serpentine formed deeper in OCT serpentinites relative to those at MOR is thus unclear. A possible explanation could be the availability of Al that may control the formation of polyhedral serpentine (Andreani et al., 2008). The nature of the protolith may thus play a role in the early crystallization of polyhedral serpentine. The OCT peridotites from the Alps are fertile lherzolites that are up to 3-4 times more enriched in Al

than the harzburgites that outcrop mainly at MAR and SWIR (Figure 9). In lherzolite, Al is mainly stored in clinopyroxene, spinel and occasionally plagioclase. As in the distal OCT lherzolite was refertilized by melt percolation, forming secondary clinopyroxene-plagioclase assemblage. As stated above (section 5.1.2), we postulate that Al released during spinel and plagioclase alteration is unlikely to contribute to the formation of polyhedral serpentine. Rather, we assume that clinopyroxene contains enough Al to form polyhedral serpentine. This is consistent with the systematic observation of polyhedral at the vicinity of clinopyroxene relicts. Consequently, we assume that OCT lherzolites are more suitable to form polyhedral serpentine and associated andradite at early time of serpentinization relative to MOR harzburgites where Al and Ca are significantly more depleted. The distribution of serpentine generations (S1 to S5) occurring in exhumed mantle rocks depend on the exhumation mode (e.g., long-offset vs flip-flop). The development of polyhedral serpentine in the early stages of serpentinization may be related to the fertility of the protolith.

6. CONCLUSION

In this study we present new petrological and geochemical investigations of 18 serpentinized peridotites out of a set of 40 samples collected in the OCT of the former Alpine Tethys, nowadays exposed in the Central Alps in SE Switzerland. Our results show that serpentinites record complex serpentinization sequences, resulting of successive episodes of fluid-rock interactions related to the progressive mantle exhumation. Four stages of serpentinization are identified giving rise to five serpentine generations with first pseudomorphic serpentine mesh and bastite made of lizardite (S1), which are then crosscut by several serpentine veins with different vein textures and serpentine polysomes (S2 to S5). These include spherical polyhedral serpentine (S2), banded (chrysotile ± polygonal ± lizardite) serpentine veins (S3), lamellar antigorite veins and patches (S4) and chrysotile crack-seal (S5). A major observation

is that while in proximal (i.e., continentwards) parts of the OCT all serpentine sequences were formed (S1 to S5), in distal domains (i.e., oceanwards) of the OCT only the initial and final serpentine generations (S1 and S5) can be found. We explain this observation with a simple model (Figure 19), suggesting that omission of intermediate serpentinization stages (S2 to S4) is reflecting a change in the mechanisms of mantle exhumation. In this model, a complete serpentinization sequence (S1 to S5) is formed, if the mantle is exhumed continuously along a single large offset detachment fault, as is the case at proximal domains of OCTs or at some oceanic core complexes at slow-spreading ridges. At the opposite, an incomplete serpentinization sequence (S1 and S5) is recorded where mantle exhumation process is discontinuous and controlled by either out-of-sequence detachments or flip-flop faults as is the case at distal OCTs or ultra-slow spreading centers. Our model can explain why serpentinization sequences observed at proximal OCTs present close similarities with those observed at large offset faults at slow MORs as well as the similar observations made at distal OCTs and ultra-slow MORs. Our study suggest that formation of serpentine generations is controlled by the mode of exhumation (i.e., continuous vs discontinuous), while the formation of each serpentine generation is controlled by the conditions of serpentinization, (i.e, temperature and pressure, composition of mantle peridotites, fluid rock ratios).

FUNDINGS

This work was supported by the French Ministry of Research, INSU-CNRS SYSTER program (BLING project, Marc Ulrich), and the M5 consortium (Gianreto Manatschal). This work has been published under the framework of the IdEx University of Strasbourg (SURVIE project, 2021).

ACNOWLEDGMENTS

Amélie Aubert (ITES) is thanked for her help during XRD analyses and René Boutin for his support for the ICP-AES/MS analyses at (ITES - University of Strasbourg). We also gratefully acknowledge Jérémy Battringer for his support during Raman data acquisition (ICUBE). Olivier Bruguier (Géosciences Montpellier) is warmly thanked for their help during the measurement of in situ trace element concentrations. We also thank Mathilde Cannat for valuable discussion. We highly appreciate the thoughtful comments of Thomas Pettke and one anonymous reviewer, which helped to clarify several aspects in this manuscript improving its quality. Lastly, we thank the efficient editorial handling by Georg Zellmer and Sarah Sherlock.

DATA AVAILABILITY

The data underlying this article are available in the article and in its online supplementary material.

REFERENCES

Agrinier, P. and Cannat, M. (1997). Oxygen-isotope constraints on serpentinization processes in ultramafic rocks from the Mid-Atlantic Ridge (23 N). *Notes*, 47:95-1.

Agrinier, P., Cornen, G., Beslier, M. O., and Whitmarsh, R. B. (1996). Mineralogical and oxygen isotopic features of serpentinites recovered from the ocean/continent transition in the Iberia Abyssal Plain. In*Proceedings-Ocean Drilling Program Scientific Results* (pp. 541-552). National science foundation.

Albers, E., Bach, W., Pérez-Gussinyé, M., McCammon, C., and Frederichs, T. (2021). Serpentinization-driven H2 production from continental break-up to mid-ocean ridge

spreading: unexpected high rates at the West Iberia margin.*Frontiers in Earth Science*,*9*, 673063.

Allen, D. E., and Seyfried Jr, W. E. (2003). Compositional controls on vent fluids from ultramafic-hosted hydrothermal systems at mid-ocean ridges: An experimental study at 400 C, 500 bars.*Geochimica et Cosmochimica Acta*,*67*(8), 1531-1542.

Alt, J. C., Schwarzenbach, E. M., Früh-Green, G. L., Shanks III, W. C., Bernasconi, S. M., Garrido, C. J., ... and Marchesi, C. (2013). The role of serpentinites in cycling of carbon and sulfur: Seafloor serpentinization and subduction metamorphism.*Lithos*,*178*, 40-54.

Amann, M., Ulrich, M., Manatschal, G., Pelt, E., Epin, M. E., Autin, J., and Sauter, D. (2020). Geochemical characteristics of basalts related to incipient oceanization: The example from the Alpine-Tethys OCTs.*Terra Nova*,*32*(1), 75-88.

Anders, E., and Grevesse, N. (1989). Abundances of the elements: Meteoritic and solar.*Geochimica et Cosmochimica acta*,*53*(1), 197-214.

Andreani, M., Baronnet, A., Boullier, A. M., and Gratier, J. P. (2004). A microstructural study of a "crack-seal" type serpentine vein using SEM and TEM techniques.*European Journal of Mineralogy*,*16*(4), 585-595.

Andreani, M., Escartin, J., Delacour, A., Ildefonse, B., Godard, M., Dyment, J., Fallick, A. E., and Fouquet, Y. (2014). Tectonic structure, lithology, and hydrothermal signature of the Rainbow massif (Mid-Atlantic Ridge 36° 14′ N).*Geochemistry, Geophysics, Geosystems*,*15*(9), 3543-3571.

Andreani, M., Grauby, O., Baronnet, A., and Muñoz, M. (2008). Occurrence, composition and growth of polyhedral serpentine.*European Journal of Mineralogy*,*20*(2), 159-171.

Andréani, M., Mével, C., Boullier, A. M., and Escartin, J. (2007). Dynamic control on serpentine crystallization in veins: Constraints on hydration processes in oceanic peridotites.*Geochemistry, Geophysics, Geosystems*,*8*(2).

Auzende, A. L., Daniel, I., Reynard, B., Lemaire, C., and Guyot, F. (2004). High-pressure behaviour of serpentine minerals: a Raman spectroscopic study.*Physics and Chemistry of Minerals*,*31*, 269-277.

Bach, W., Garrido, C. J., Paulick, H., Harvey, J., and Rosner, M. (2004). Seawater-peridotite interactions: First insights from ODP Leg 209, MAR 15 N.*Geochemistry, Geophysics, Geosystems*,*5*(9).

Bach, W., Paulick, H., Garrido, C. J., Ildefonse, B., Meurer, W. P., and Humphris, S. E. (2006). Unraveling the sequence of serpentinization reactions: petrography, mineral chemistry, and petrophysics of serpentinites from MAR 15 N (ODP Leg 209, Site 1274).*Geophysical research letters*,*33*(13).

Bach, W., Rosner, M., Jöns, N., Rausch, S., Robinson, L. F., Paulick, H., and Erzinger, J. (2011). Carbonate veins trace seawater circulation during exhumation and uplift of mantle rock: Results from ODP Leg 209.*Earth and Planetary Science Letters*,*311*(3-4), 242-252.

Barnes, J. D., Paulick, H., Sharp, Z. D., Bach, W., and Beaudoin, G. (2009). Stable isotope (δ18O, δD, δ37Cl) evidence for multiple fluid histories in mid-Atlantic abyssal peridotites (ODP Leg 209).*Lithos*,*110*(1-4), 83-94.

Bau, M. (1991). Rare-earth element mobility during hydrothermal and metamorphic fluid-rock interaction and the significance of the oxidation state of europium.*Chemical Geology*,*93*(3-4), 219-230.

Beard, J. S., and Frost, B. R. (2017). The stoichiometric effects of ferric iron substitutions in serpentine from microprobe data.*International Geology Review*,*59*(5-6), 541-547.

Beard, J. S., Frost, B. R., Fryer, P., McCaig, A., Searle, R., Ildefonse, B., ... and Sharma, S. K. (2009). Onset and progression of serpentinization and magnetite formation in olivine-rich troctolite from IODP Hole U1309D.*Journal of Petrology*,*50*(3), 387-403.

Beard, J. S., and Hopkinson, L. (2000). A fossil, serpentinization-related hydrothermal vent, Ocean Drilling Program Leg 173, Site 1068 (Iberia Abyssal Plain): Some aspects of mineral and fluid chemistry.*Journal of Geophysical Research: Solid Earth*,*105*(B7), 16527-16539.

Bernoulli, D., and Weissert, H. (1985). Sedimentary fabrics in Alpine ophicalcites, south Pennine Arosa zone, Switzerland.*Geology*,*13*(11), 755-758.

Beslier, M. O., Royer, J. Y., Girardeau, J., Hill, P. J., Boeuf, E., Buchanan, C., ... and Thomas, S. (2004). A wide ocean-continent transition along the south-west Australian margin: first

results of the MARGAU/MD110 cruise.*Bulletin de la Société Géologique de France*,*175*(6), 629-641.

Blackman, D. K., Karson, J. A., Kelley, D. S., Cann, J. R., Früh-Green, G. L., Gee, J. S., ... and Williams, E. A. (2002). Geology of the Atlantis Massif (Mid-Atlantic Ridge, 30 N): Implications for the evolution of an ultramafic oceanic core complex.*Marine Geophysical Researches*,*23*, 443-469.

Boddupalli, B., Minshull, T. A., Bayrakci, G., Lymer, G., Klaeschen, D., and Reston, T. J. (2022). Insights into exhumation and mantle hydration processes at the deep Galicia margin from a 3D high-resolution seismic velocity model.*Journal of Geophysical Research: Solid Earth*,*127*(7), e2021JB023220.

Boillot, G., Féraud, G., Recq, M., and Girardeau, J. (1989). Undercrusting by serpentinite beneath rifted margins.*Nature*,*341*(6242), 523-525.

Boillot, G., Grimaud, S., Mauffret, A., Mougenot, D., Kornprobst, J., Mergoil-Daniel, J., and Torrent, G. (1980). Ocean-continent boundary off the Iberian margin: a serpentinite diapir west of the Galicia Bank.*Earth and Planetary Science Letters*,*48*(1), 23-34.

Bonatti, E. (1968). Ultramafic rocks from the mid-Atlantic ridge.*Nature*,*219*(5152), 363-364.

Bousquet, R., Oberhänsli, R., Goffé, B., Wiederkehr, M., Koller, F., Schmid, S. M., Schuster, R., Engi, M., Berger, A.,& Martinotti, G. (2008). Metamorphism of metasediments at the scale of an orogen: a key to the Tertiary geodynamic evolution of the Alps.*Geological Society, London, Special Publications*,*298*(1), 393-411.

Burkhard, D. J. and O'Neil, J. R. (1988). Contrasting serpentinization processes in the Eastern Central Alps. *Contributions to Mineralogy and Petrology*, 99(4):498-506.

Cann, J. R., Blackman, D., Smith, D., McAllister, E., Janssen, B., Mello, S., Avgerinos, E., Pascoe, A., and Escartin, J. (1997). Corrugated slip surfaces formed at ridge-transform intersections on the Mid-Atlantic Ridge. *Nature*, 385(6614):329-332.

Cannat, M. (1993). Emplacement of mantle rocks in the seafloor at mid-ocean ridges.*Journal of Geophysical Research: Solid Earth*,*98*(B3), 4163-4172.

Cannat, M., Manatschal, G., Sauter, D., and Peron-Pinvidic, G. (2009). Assessing the conditions of continental breakup at magma-poor rifted margins: What can we learn from slow spreading mid-ocean ridges? *Comptes Rendus Geoscience*, 341(5):406-427.

Cannat, M., Sauter, D., Lavier, L., Bickert, M., Momoh, E., and Leroy, S. (2019). On spreading modes and magma supply at slow and ultraslow mid-ocean ridges. *Earth and Planetary Science Letters*, 519:223-233.

Chauvel, C., Bureau, S., and Poggi, C. (2011). Comprehensive chemical and isotopic analyses of basalt and sediment reference materials. *Geostandards and Geoanalytical Research*, 35(1):125-143.

Christensen, N. I. (1972). The abundance of serpentinites in the oceanic crust. *The Journal of Geology*, 80(6):709-719.

Christensen, N. I. (2004). Serpentinites, peridotites, and seismology. *International Geology Review*, 46(9):795-816.

Coltat, R., Boulvais, P., Riegler, T., Pelleter, E., and Branquet, Y. (2021). Element distribution in the root zone of ultramafic-hosted black smoker-like systems: Constraints from an Alpine analog. *Chemical Geology*, 559.

Coltat, R., Branquet, Y., Gautier, P., Rodriguez, H. C., Poujol, M., Pelleter, E., McClenaghan, S., Manatschal, G., and Boulvais, P. (2019). Unravelling the root zone of ultramafic-hosted black smokers-like hydrothermalism from an Alpine analog. *Terra Nova*, 31:549-561.

Compagnoni, R., Cossio, R., and Mellini, M. (2021). Raman anisotropy in serpentine minerals, with a caveat on identification.*Journal of Raman Spectroscopy*,*52*(7), 1334-1345.

Debret, B., Andreani, M., Godard, M., Nicollet, C., Schwartz, S., and Lafay, R. (2013). Trace element behavior during serpentinization/de-serpentinization of an eclogitized oceanic lithosphere: A LA-ICPMS study of the Lanzo ultramafic massif (Western Alps).*Chemical Geology*,*357*, 117-133.

Debret, B., Nicollet, C., Andreani, M., Schwartz, S., and Godard, M. (2013b). Three steps of serpentinization in an eclogitized oceanic serpentinization front (Lanzo massif-Western Alps). *Journal of Metamorphic Geology*, 31(2):165-186.

Desmurs, L., Manatschal, G., and Bernoulli, D. (2001). The Steinmann Trinity revisited: mantle exhumation and magmatism along an ocean-continent transition: the Platta nappe, Eastern Switzerland. *Contributions to Mineralogy and Petrology*, 144:365-382.

Dietrich, V. J. (1969). Die Ophiolithe des Oberhalbsteins (Graubünden) und das Ophiolithmaterial der ostschweizerischen Molasseablagerungen: ein petrographischer Vergleich(Doctoral dissertation, ETH Zurich).

Dietrich, V. (1970). Die Stratigraphie der Platta-Decke: Fazielle Zusammenhänge zwischen Oberpenninikum und Unterostalpin. Geologisches Institut der Eidg. Technischen Hochschule und der Universität Zürich.

Dilek, Y., Coulton, A., and Hurst, S. D. (1997). Serpentinization and hydrothermal veining in peridotites at site 920 in the Mark area. In*Proceedings-Ocean Drilling Program Scientific Results*(pp. 35-60). National Science Foundation.

Doebelin, N. and Kleeberg, R. (2015). Profex: a graphical user interface for the rietveld refinement program BGMN. *Journal of applied crystallography*, 48(5):1573-1580.

Douville, E., Charlou, J. L., Oelkers, E. H., Bienvenu, P., Colon, C. F. J., Donval, J. P., Fouquet, Y., Prieur, D., and Appriou, P. (2002). The Rainbow vent fluids (36°14N, MAR): the influence of ultramafic rocks and phase separation on trace metal content in Mid-Atlantic Ridge hydrothermal fluids. *Chemical Geology*, 184:37-48.

Elter, G. (1971). Schistes lustrés et ophiolites de la zone piémontaise entre Orco et Doire Baltée (Alpes Graies). Hypothèses sur l'origine des ophiolites.*Géologie Alpine*,*47*, 147-169.

Epin, M.-E. and Manatschal, G. (2018). Three-dimensional architecture, structural evolution, and role of inheritance controlling detachment faulting at a hyperextended distal margin: The example of the Err detachment system (SE Switzerland). *Tectonics*, 37(12):4494-4514.

Epin, M. E., Manatschal, G., Amman, M., Ribes, C., Clausse, A., Guffon, T., and Lescanne, M. (2019). Polyphase tectono-magmatic evolution during mantle exhumation in an ultra-distal, magma-poor rift domain: example of the fossil Platta ophiolite, SE Switzerland. *International Journal of Earth Sciences*, 108:2443-2467.

Escartin, J., Hirth, G., and Evans, B. (1997). Effects of serpentinization on the lithospheric strength and the style of normal faulting at slow-spreading ridges. *Earth and Planetary Science Letters*, 151(3-4):181-189.

Escartin, J., Hirth, G., and Evans, B. (2001). Strength of slightly serpentinized peridotites: Implications for the tectonics of oceanic lithosphere. *Geology*, 29(11):1023-1026.

Evans, B. W. (2004). The serpentinite multisystem revisited: chrysotile is metastable.*International Geology Review*,*46*(6), 479-506.

Florineth, D., and Froitzheim, N. (1994).Transition from continental to oceanic basement in the Tasna Nappe: evidence for Early Cretaceous opening of the Valais Ocean.

Frassi, C., Chighine, G., Mauro, D., Biagioni, C., Zaccarini, F., and Marroni, M. (2022). Pervasive crystallization of antigorite in northern apennine ophiolites: the example of Montecarelli peridotites (Tuscany, Central Italy). *Ofioliti*, 47(1).

Frey, M., and Ferreiro Mählmann, R. (1999). Alpine metamorphism of the Central Alps.*Schweizerische mineralogische und petrographische Mitteilungen*,*79*(1), 135-154.

Froitzheim, N., Schmid, S., and Conti, P. (1994). Repeated change from crustal shortening to orogen-parallel extension in the Austroalpine units of Graub" unden.*Eclogae Geologicae Helvetiae*,*87*(2), 559-612.

Froitzheim, N., and Manatschal, G. (1996). Kinematics of Jurassic rifting, mantle exhumation, and passive-margin formation in the Austroalpine and Penninic nappes (eastern Switzerland).*Geological society of America bulletin*,*108*(9), 1120-1133.

Froitzheim, N. and Rubatto, D. (1998). Continental breakup by detachment faulting: field evidence and geochronological constraints (Tasna nappe, Switzerland). *Terra Nova*, 10(4):171-176.

Frost, B. R. and Beard, J. S. (2007). On silica activity and serpentinization. *Journal of petrology*, 48(7):1351-1368.

Früh-Green, G. L., Connolly, J. A., Plas, A., Kelley, D. S., and Grobéty, B. (2004). Serpentinization of oceanic peridotites: implications for geochemical cycles and biological activity. *The subsea- floor biosphere at mid-ocean ridges*, 144:119-136.

Früh-Green, G. L., Plas, A., and Lécuyer, C. (1996). Petrologic and stable isotope constraints on hydrothermal alteration and serpentinization of the EPR shallow mantle at Hess Deep (Site 895). In*Proceedings-Ocean Drilling Program Scientific Results*(pp. 255-292). National Science Foundation.

Früh-Green, G. L., Scambelluri, M., & Vallis, F. (2001). O–H isotope ratios of high pressure ultramafic rocks: implications for fluid sources and mobility in the subducted hydrous mantle.*Contributions to Mineralogy and Petrology*,*141*(2), 145-159.

Früh-Green, G. L., Weissert, H., and Bernoulli, D. (1990). A multiple fluid history recorded in Alpine ophiolites.*Journal of the Geological Society*,*147*(6), 959-970.

Gillard, M., Autin, J., and Manatschal, G. (2016). Fault systems at hyper-extended rifted margins and embryonic oceanic crust: Structural style, evolution and relation to magma. *Marine and Petroleum Geology*, 76:51-67.

Gillard, M., Tugend, J., Müntener, O., Manatschal, G., Karner, G. D., Autin, J., Sauter, D., Figueredo, P. H., and Ulrich, M. (2019). The role of serpentinization and magmatism in the formation of decoupling interfaces at magma-poor rifted margins.*Earth-Science Reviews*,*196*, 102882.

Govindaraju, K. (1982). Report (1967–1981) on four ANRT rock reference samples: diorite DR-N, serpentine UB-N, bauxite BX-N and disthene DT-N.*Geostandards Newsletter*,*6*(1), 91-159.

Grauby, O., Baronnet, A., Devouard, B., Schoumacker, K., and Demirdjian, L. (1998, April). The chrysotile-polygonal serpentine-lizardite suite synthesized from a 3MgO-2SiO2-excess H2O gel. In*The 7th International Symposium on Experimental Mineralogy, Petrology, and Geochemistry, Orléans, Abstracts. Terra Nova, supplement*(Vol. 1, p. 24).

Groppo, C., Rinaudo, C., Cairo, S., Gastaldi, D., and Compagnoni, R. (2006). Micro-raman spectro-scopy for a quick and reliable identification of serpentine minerals from ultramafics. *European Journal of Mineralogy*, 18(3):319-329.

Guillong, M., Meier, D. L., Allan, M. M., Heinrich, C. A., Yardley, B. W., et al. (2008). Appendix a6: Sills: A Matlab-based program for the reduction of laser ablation ICP-MS data of

homogeneous materials and inclusions. *Mineralogical Association of Canada Short Course*, 40:328-333.

Hart, S. R., and Zindler, A. (1986). In search of a bulk-Earth composition.*Chemical Geology*, *57*(3-4), 247-267.

Hébert, R., Constantin, M., Robinson, P., et al. (1991). Primary mineralogy of leg 118 gabbroic rocks and their place in the spectrum of oceanic mafic igneous rocks. In *Von Herzen, RP, Robinson, PT, et al., Proc. ODP, Sci. Results*, volume 118, pages 3-20.

Hochscheid, F., Coltat, R., Ulrich, M., Munoz, M., Manatschal, G., and Boulvais, P. (2022). The Sr isotope geochemistry of oceanic ultramafic-hosted mineralizations. *Ore Geology Reviews*, page 104824.

Hopkinson, L., Beard, J., and Boulter, C. (2004). The hydrothermal plumbing of a serpentinite-hosted detachment: evidence from the West Iberia non-volcanic rifted continental margin. *Marine Geology*, 204(3-4):301-315.

Jagoutz, E., Palme, H., Baddenhausen, H., Blum, K., Cendales, M., Dreibus, G., Spettel, B., Lorenz, V., and Wänke, H. (1979). The abundances of major, minor and trace elements in the earth's mantle as derived from primitive ultramafic nodules. In: Lunar and Planetary Science Conference, 10th, Houston, Tex., March 19-23, 1979, Proceedings. Volume 2.(A80-23617 08-91) New York, Pergamon Press, Inc., 1979, p. 2031-2050. Research supported by the Deutsche Forschungsgemeinschaft.(Vol. 10, pp. 2031-2050).

Janecky, D. and Seyfried, W. (1986). Hydrothermal serpentinization of peridotite within the oceanic crust: Experimental investigations of mineralogy and major element chemistry. *Geochimica et Cosmochimica Acta*, 50(7):1357-1378.

Jarosewich, E., Nelen, J., and Norberg, J. A. (1980). Reference samples for electron microprobe analysis. *Geostandards Newsletter*, 4(1):43-47.

Karson, J. A. and Rona, P. A. (1990). Block-tilting, transfer faults, and structural control of magmatic and hydrothermal processesin the tag area, Mid-Atlantic Ridge 26°N. *Geological Society of America Bulletin*, 102(12):1635-1645.

Klein, F., Bach, W., and McCollom, T. M. (2013). Compositional controls on hydrogen generation during serpentinization of ultramafic rocks. *Lithos*, 178:55-69.

Klein, F., Marschall, H. R., Bowring, S. A., Humphris, S. E., and Horning, G. (2017). Mid-ocean ridge serpentinite in the Puerto Rico trench: From seafloor spreading to subduction. *Journal of Petrology*, 58(9):1729-1754.

Klein, F. and Roux, V. L. (2020). Quantifying the volume increase and chemical exchange during serpentinization. *Geology*, 48:552-556.

Klinkhammer, G., Elderfield, H., Edmond, J., and Mitra, A. (1994). Geochemical implications of rare earth element patterns in hydrothermal fluids from mid-ocean ridges. *Geochimica et Cosmochimica Acta*, 58(23):5105-5113.

Kodolányi, J., & Pettke, T. (2011). Loss of trace elements from serpentinites during fluid-assisted transformation of chrysotile to antigorite—An example from Guatemala. *Chemical Geology*, *284*(3-4), 351-362.

Kodolányi, J., Pettke, T., Spandler, C., Kamber, B. S., and Gméling, K. (2012). Geochemistry of ocean floor and fore-arc serpentinites: constraints on the ultramafic input to subduction zones. *Journal of Petrology*, *53*(2), 235-270.

Lafay, R., Baumgartner, L. P., Stephane, S., Suzanne, P., German, M.-H., and Torsten, V. (2017). Petrologic and stable isotopic studies of a fossil hydrothermal system in ultramafic environment (Chenaillet ophicalcites, Western Alps, France): processes of carbonate cementation. *Lithos*, 294:319-338.

Lafay, R., Deschamps, F., Schwartz, S., Guillot, S., Godard, M., Debret, B., and Nicollet, C. (2013). High-pressure serpentinites, a trap-and-release system controlled by metamorphic conditions: Example from the Piedmont zone of the Western Alps. *Chemical Geology*, 343:38-54.

Lagabrielle, Y. and Bodinier, J.-L. (2008). Submarine reworking of exhumed subcontinental mantle rocks: field evidence from the lherz peridotites, french pyrenees. *Terra Nova*, 20(1):11-21.

Lamadrid, H., Zajacz, Z., Klein, F., and Bodnar, R. (2021). Synthetic fluid inclusions xxiii. effect of temperature and fluid composition on rates of serpentinization of olivine. *Geochimica et Cosmochimica Acta*, 292:285-308.

Lavier, L. L., Roger Buck, W., and Poliakov, A. N. (1999). Self-consistent rolling-hinge model for the evolution of large-offset low-angle normal faults. *Geology*, 27(12):1127-1130.

Liu, W., Cao, Y., Zhang, J., Zhang, Y., Zong, K., and Jin, Z. (2020). Thermo-structural evolution of the Val Malenco (Italy) peridotite: A petrological, geochemical and microstructural study. *Minerals*, 10(11):962.

Manatschal, G. (2004). New models for evolution of magma-poor rifted margins based on a review of data and concepts from West Iberia and the Alps. *International Journal of Earth Sciences*, 93:432-466.

Manatschal, G., Engström, A., Desmurs, L., Schaltegger, U., Cosca, M., Müntener, O., and Bernoulli, D. (2006). What is the tectono-metamorphic evolution of continental break-up: the example of the Tasna Ocean–Continent Transition. *Journal of Structural Geology*, *28*(10), 1849-1869.

Manatschal, G. and Müntener, O. (2009). A type sequence across an ancient magma-poor ocean-continent transition: the example of the Western Alpine Tethys ophiolites. *Tectonophysics*, 473(1-2):4-19.

Manatschal, G. and Nievergelt, P. (1997). A continent-ocean transition recorded in the Err and Platta nappes (Eastern Switzerland). *Eclogae Geologicae Helvetiae*, 90(1):3-28.

Martin, B. and Fyfe, W. (1970). Some experimental and theoretical observations on the kinetics of hydration reactions with particular reference to serpentinization. *Chemical Geology*, 6:185-202.

Mellini, M., Trommsdorff, V., and Compagnoni, R. (1987). Antigorite polysomatism: behaviour during progressive metamorphism. *Contributions to Mineralogy and Petrology*, 97(2):147-155.

Mellini, M., Rumori, C., and Viti, C. (2005). Hydrothermally reset magmatic spinels in retrograde serpentinites: formation of “ferritchromit” rims and chlorite aureoles. Contributions to Mineralogy and Petrology, 149, 266-275.

Minshull, T. A. (2009). Geophysical characterisation of the ocean-continent transition at magma-poor rifted margins. *Comptes Rendus Geoscience*, 341(5):382-393.

Morrow, C., Moore, D. E., and Lockner, D. (2000). The effect of mineral bond strength and adsorbed water on fault gouge frictional strength. *Geophysical research letters*, 27(6):815-818.

Müntener, O., Manatschal, G., Desmurs, L., and Pettke, T. (2010). Plagioclase peridotites in ocean-continent transitions: refertilized mantle domains generated by melt stagnation in the shallow mantle lithosphere. *Journal of Petrology*, 51(1-2):255-294.

Müntener, O., Pettke, T., Desmurs, L., Meier, M., and Schaltegger, U. (2004). Refertilization of mantle peridotite in embryonic ocean basins: trace element and Nd isotopic evidence and implications for crust-mantle relationships. *Earth and Planetary Science Letters*, 221(1-4):293-308.

Müntener, O. and Piccardo, G. B. (2004). Melt migration in ophiolitic peridotites: The message from Alpine-Apennine peridotites and implications for embryonic ocean basins. *Geological Society Special Publication*, 218:69-89.

Nicholls, I., Ferguson, J., Jones, H., Marks, G., and Mutter, J. (1981). Ultramafic blocks from the ocean floor Southwest of Australia. *Earth and Planetary Science Letters*, 56:362-374.

Niu, Y. (2004). Bulk-rock major and trace element compositions of abyssal peridotites: implications for mantle melting, melt extraction and post-melting processes beneath mid-ocean ridges. *Journal of Petrology*, 45(12):2423-2458.

Normand, C., Williams-Jones, A. E., Martin, R. F., and Vali, H. (2002). Hydrothermal alteration of olivine in a flow-through autoclave: Nucleation and growth of serpentine phases. *American Mineralogist*, 87(11-12):1699-1709.

O'Hanley, D. S. (1992). Solution to the volume problem in serpentinization. *Geology*, 20(8):705-708.

O'Hanley, D. S. and Dyar, M. D. (1998). The composition of chrysotile and its relationship with lizardite. *The Canadian Mineralogist*, 36(3):727-739.

O'Hanley, D. S. and Offler, R. (1992). Characterization of multiple serpentinization, woodsreef, new south wales. *The Canadian Mineralogist*, 30(4):1113-1126.

Parnell-Turner, R., Sohn, R. A., Peirce, C., Reston, T. J., MacLeod, C. J., Searle, R. C., and Simão, N. M. (2017). Oceanic detachment faults generate compression in extension. *Geology*, 45(10), 923-926.

Paulick, H., Bach, W., Godard, M., De Hoog, J., Suhr, G., and Harvey, J. (2006). Geochemistry of abyssal peridotites (Mid-Atlantic Ridge, 15°N, ODP leg 209): implications for fluid/rock interaction in slow spreading environments. *Chemical geology*, 234(3-4):179-210.

Pearce, N. J., Perkins, W. T., Westgate, J. A., Gorton, M. P., Jackson, S. E., Neal, C. R., & Chenery, S. P. (1997). A compilation of new and published major and trace element data for NIST SRM 610 and NIST SRM 612 glass reference materials. *Geostandards newsletter*, *21*(1), 115-144.

Peters, P. C. and Mathews, J. (1963). Gravitational radiation from point masses in a keplerian orbit. *Physical Review*, 131(1):435.

Peters, T. (1965). A water-bearing andradite from the Totalp serpentine (Davos, Switzerland). *American Mineralogist: Journal of Earth and Planetary Materials*, *50*(9), 1482-1486.

Peters, T. and Stettler, A. (1987a). Radiometric age, thermobarometry and mode of emplacement of the Totalp peridotite in the Eastern Swiss Alps. *Schweizerische Mineralogische und Petrographische Mitteilungen*, 67(3):285-294.

Peters, T. and Stettler, A. (1987b). Time, physico-chemical conditions, mode of emplacement and geologic setting of the Totalp peridotite in the Eastern Swiss Alps. *Schweiz. Mineral. Petrogr. Mitt*, 67:285-294.

Pettke, T., and Bretscher, A. (2022). Fluid-mediated element cycling in subducted oceanic lithosphere: The orogenic serpentinite perspective. *Earth-science reviews*, *225*, 103896.

Pettke, T., Oberli, F., Audétat, A., Guillong, M., Simon, A. C., Hanley, J. J., and Klemm, L. M. (2012). Recent developments in element concentration and isotope ratio analysis of individual fluid inclusions by laser ablation single and multiple collector icp-ms. *Ore Geology Reviews*, 44:10-38.

Picazo, S., Manatschal, G., Cannat, M., and Andréani, M. (2013). Deformation associated to exhumation of serpentinized mantle rocks in a fossil Ocean Continent Transition: The Totalp unit in SE Switzerland). *Lithos*, 175:255-271.

Picazo, S., Müntener, O., Manatschal, G., Bauville, A., Karner, G., and Johnson, C. (2016). Mapping the nature of mantle domains in Western and Central Europe based on clinopyroxene and spinel chemistry: Evidence for mantle modification during an extensional cycle. *Lithos, 266*, 233-263.

Piccardo, G. B. (2013). Subduction of a fossil slow–ultraslow spreading ocean: a petrology-constrained geodynamic model based on the Voltri Massif, Ligurian Alps, Northwest Italy. *International Geology Review*, *55*(7), 787-803.

Plümper, O., Beinlich, A., Bach, W., Janots, E., and Austrheim, H. (2014). Garnets within geode-like serpentinite veins: Implications for element transport, hydrogen production and life-supporting environment formation. *Geochimica et Cosmochimica Acta*, 141:454-471.

Raleigh, C. and Paterson, M. (1965). Experimental deformation of serpentinite and its tectonic implications. *Journal of Geophysical Research*, 70(16):3965-3985.

Rampone, E., Borghini, G., and Basch, V. (2020). Melt migration and melt-rock reaction in the Alpine-Apennine peridotites: Insights on mantle dynamics in extending lithosphere. *Geoscience Frontiers*, 11(1):151-166.

Rampone, E., Hofmann, A. W., and Raczek, I. (1998). Isotopic contrasts within the internal Liguride Ophiolite (N. Italy): the lack of a genetic mantle-crust link. *Earth and Planetary Science Letters*, 163:175-189.

Ramsay, J. G. (1980). The crack-seal mechanism of rock deformation. *Nature*, 284(5752):135-139.

Reinen, L. A., Weeks, J. D., and Tullis, T. E. (1994). The frictional behavior of lizardite and antigorite serpentinites: Experiments, constitutive models, and implications for natural faults. *Pure and Applied Geophysics*, *143*, 317-358.

Reston, T. (2018). Flipping detachments: The kinematics of ultraslow spreading ridges. *Earth and Planetary Science Letters*, 503:144-157.

Reston, T. J. and McDermott, K. G. (2011). Successive detachment faults and mantle unroofing at magma-poor rifted margins. *Geology*, 39(11):1071-1074.

Ribeiro Da Costa, I., Barriga, F. J., Viti, C., Mellini, M., and Wicks, F. J. (2008). Antigorite in deformed serpentinites from the Mid-Atlantic Ridge. *European Journal of Mineralogy*, 20(4):563-572.

Ribes, C., Petri, B., Ghienne, J.-F., Manatschal, G., Galster, F., Karner, G. D., Figueredo, P. H., Johnson, C. A., and Karpoff, A.-M. (2020). Tectono-sedimentary evolution of a fossil ocean-continent transition: Tasna nappe, Central Alps (SE Switzerland). *GSA Bulletin*, 132(7-8):1427-1446.

Rimstidt, J. D., Brantley, S. L., and Olsen, A. A. (2012). Systematic review of forsterite dissolution rate data. *Geochimica et Cosmochimica Acta*, 99:159-178.

Rouméjon, S., Andreani, M., and Früh-Green, G. L. (2019). Antigorite crystallization during oceanic retrograde serpentinization of abyssal peridotites. *Contributions to Mineralogy and Petrology*, 174(7):1-25.

Rouméjon, S. and Cannat, M. (2014). Serpentinization of mantle-derived peridotites at mid- ocean ridges: Mesh texture development in the context of tectonic exhumation. *Geochemistry, Geophysics, Geosystems*, 15(6):2354-2379.

Rouméjon, S., Cannat, M., Agrinier, P., Godard, M., and Andreani, M. (2015). Serpentinization and fluid pathways in tectonically exhumed peridotites from the Southwest Indian Ridge (62–65 E). *Journal of Petrology*, *56*(4), 703-734.

Rouméjon, S., Williams, M. J., and Früh-Green, G. L. (2018). In-situ Oxygen isotope analyses in serpentine minerals: Constraints on serpentinization during tectonic exhumation at slow-and ultraslow-spreading ridges. *Lithos*, 323:156-173.

Salters, V. J. and Stracke, A. (2004). Composition of the depleted mantle. *Geochemistry, Geophysics, Geosystems*, 5(5).

Sandiford, D., Brune, S., Glerum, A., Naliboff, J., and Whittaker, J. M. (2021). Kinematics of foot-wall exhumation at oceanic detachment faults: solid-block rotation and apparent unbending. *Geochemistry, Geophysics, Geosystems*, 22(4):e2021GC009681.

Sauter, D., Cannat, M., Rouméjon, S., Andreani, M., Birot, D., Bronner, A., Brunelli, D., Carlut, J., Delacour, A., Guyader, V., et al. (2013). Continuous exhumation of mantle-derived rocks at the Southwest Indian Ridge for 11 million years. *Nature Geoscience*, 6(4):314-320.

Scambelluri, M., Fiebig, J., Malaspina, N., Müntener, O., and Pettke, T. (2004). Serpentinite subduction: implications for fluid processes and trace-element recycling. *International Geology Review*, 46(7):595-613.

Schaltegger, U., Desmurs, L., Manatschal, G., Müntener, O., Meier, M., Frank, M., and Bernoulli, D. (2002). The transition from rifting to sea-floor spreading within a magma-poor rifted margin: Field and isotopic constraints. *Terra Nova*, 14(3):156-162.

Schwartz, S., Guillot, S., Reynard, B., Lafay, R., Debret, B., Nicollet, C., Lanari, P., and Auzende, A. L. (2013). Pressure-temperature estimates of the lizardite/antigorite transition in high pressure serpentinites. *Lithos*, 178:197-210.

Schwarzenbach, E. M., Caddick, M. J., Beard, J. S., and Bodnar, R. J. (2016). Serpentinization, element transfer, and the progressive development of zoning in veins: evidence from a partially serpentinized harzburgite. *Contributions to Mineralogy and Petrology*, 171:1-22.

Schwarzenbach, E. M., Früh-Green, G. L., Bernasconi, S. M., Alt, J. C., and Plas, A. (2013). Serpentinization and carbon sequestration: A study of two ancient peridotite-hosted hydro-thermal systems. *Chemical Geology*, 351:115-133.

Schwarzenbach, E. M., Vogel, M., Früh-Green, G. L., and Boschi, C. (2021). Serpentinization, Carbonation, and Metasomatism of Ultramafic Sequences in the northern Apennine Ophiolite (NW Italy). *Journal of Geophysical Research: Solid Earth*, 126.

Smith, D. K., Cann, J. R., & Escartín, J. (2006). Widespread active detachment faulting and core complex formation near 13 N on the Mid-Atlantic Ridge. *Nature*, *442*(7101), 440-443.

Tarling, M. S., Rooney, J. S., Viti, C., Smith, S. A., and Gordon, K. C. (2018). Distinguishing the Raman spectrum of polygonal serpentine. *Journal of Raman Spectroscopy, 49(12),* 1978-1984.

Tarling, M. S., Smith, S. A., Rooney, J. S., Viti, C., and Gordon, K. C. (2021). A common type of mineralogical banding in serpentine crack-seal veins. *Earth and Planetary Science Letters*, 564:116930.

Theunissen, T. and Huismans, R. S. (2022). Mantle exhumation at magma-poor rifted margins controlled by frictional shear zones. *Nature Communications*, 13(1):1-12.

Tichadou, C., Godard, M., Muñoz, M., Labaume, P., Vauchez, A., Gaucher, E. C., & Calassou, S. (2021). Mineralogical and geochemical study of serpentinized peridotites from the North-Western Pyrenees: New insights on serpentinization along magma-poor continental passive margins. *Lithos*, *406*, 106521.

Trommsdorff, V. (1983). Metamorphose magnesiumreicher Gesteine: kristallischer Vergleich von Natur, Experiment und thermodynamischer Datenbasis. *Fortschritte der Mineralogie*, *61*(2), 283-308.

Trommsdorff, V. and BW, E. (1974). Alpine metamorphism of peridotitic rocks.

Trommsdorff, V. and Evans, B. W. (1977). Antigorite-ophicarbonates: contact metamorphism in valmalenco, italy. *Contributions to Mineralogy and Petrology*, 62(3):301-312.

Trümpy, R. & Dössegger, R., (1972). Permian of Switzerland. *Rotliegend, Essays on European Lower Permian. Brill, Leiden*, 189-213.

Tucholke, B. E., Sawyer, D. S., & Sibuet, J. C. (2007). Breakup of the Newfoundland–Iberia rift. *Geological Society, London, Special Publications*, *282*(1), 9-46.

Ulmer, P. and Trommsdorff, V. (1995). Serpentine stability to mantle depths and subduction-related magmatism. *Science*, 268(5212):858-861.

Ulrich, M., Muñoz, M., Boulvais, P., Cathelineau, M., Cluzel, D., Guillot, S., and Picard, C. (2020). Serpentinization of new caledonia peridotites: from depth to (sub-)surface. *Contributions to Mineralogy and Petrology*, 175(9):1-25.

Vesin, C., Rubatto, D., Pettke, T., and Deloule, E. (2023). Multistage hydration during oceanic serpentinisation revealed by in situ oxygen isotope and trace element analyses. Geochimica et Cosmochimica Acta, 355, 13-31.

Vesin, C., Rubatto, D., and Pettke, T. (2024). The history of serpentinisation at mid-ocean ridges: Insights from in situ trace elements coupled with oxygen and boron isotopes. Chemical Geology, 122060.

Vils, F., Müntener, O., Kalt, A., and Ludwig, T. (2011). Implications of the serpentine phase transition on the behaviour of beryllium and lithium-boron of subducted ultramafic rocks. *Geochimica et Cosmochimica Acta*, 75(5):1249-1271.

Viti, C. and Mellini, M. (1997). Contrasting chemical compositions in associated lizardite and chrysotile in veins from Elba, Italy. *European Journal of Mineralogy*, 9(3):585-596.

Weissert, B. J. H. and Bernoulli, D. (1985). A transform margin in the Mesozoic Tethys: evidence from the Swiss Alps. *Geologische Rundschau*, 74:665-679.

Whitmarsh, R., Manatschal, G., and Minshull, T. (2001). Evolution of magma-poor continental margins from rifting to seafloor spreading. *Nature*, 413(6852):150-154.

Wicks, F. J. and Whittaker, E. (1977). Serpentine textures and serpentinization. *The Canadian Mineralogist*, 15(4):459-488.

Wunder, B. and Schreyer, W. (1997). Antigorite: High-pressure stability in the system MgO-SiO2-H2O (MSH). *Lithos*, 41(1-3):213-227.

Figures

Figure 1: A) Present-day location of ophiolitic units of the Central-Western Alps and Apennines (modified after Manatschal and Müntener, 2009). B) Schematic reconstruction of the Piemonte-Ligurian oceanic basin at Late Jurassic time, with the location of the major ophiolitic sequences (modified after Manatschal and Müntener, 2009). C) Simplified geological map of the Pennine and Austro-Alpine nappes showing sample locations (modified after Froitzheim et al., 1994). D) Distribution of subcontinental and infiltrated mantle domains along the ocean-continent-transition of the Alpine Tethys (modified after Müntener and Piccardo, 2004). CH: Chenaillet; PL: Platta; TA: Tasna; TO: Totalp.

Figure 2: A) Geological map of the Platta nappe with sample locations (modified after Schaltegger et al., 2002). B) Photograph of the Falotta area, and C) interpretative drawing of the Falotta area showing the various lithologies and their respective structural relations (the basalts overlie the lower Platta Unit made of serpentinized mantle separated by a rift-related detachment surface.

Figure 3: A) Geological map of the Totalp area with sample locations (modified after Picazo et al., 2013). B) South-north oriented cross-section across the Totalp area showing Alpine thrusts and folds. C) Photograph of massive serpentinite outcrop . D) Photograph of the serpentinite wall near Weissfluhjoch (samples Tot 19-01,02).

Figure 4: A) Simplified geological map of the western Engadine window in SE Switzerland and Austria and location of the Tasna nappe (modified after Trümpy and Doessegger, 1972; Florineth and Froitzheim, 1994; Manatschal et al., 2006). B) Panoramic view of the Tasna ocean-continent-zone. C) Geological interpretation of the Tasna area showing the serpentinized mantle that is separated from the continental crust (in the SSW) and post-rift

1449 sediments (in the NNE) by rift-related detachment faults. The base of the mantle is an Alpine
1450 thrust fault (modified from Florineth and Froitzheim, 1994; Manatschal et al., 2006).

1451 Figure 5: Representative photographs of the diversity of textures in serpentinites sampled in
1452 the three distinct sites (Platta, Totalp, Tasna). A) Massive dark green serpentinite crosscut by
1453 a fibrous serpentine vein of pale green color (Fal 18-02, Upper Platta unit). B) Clasts of
1454 massive dark serpentinite embedded in a serpentine matrix of a fibrous texture (Fal 18-12,
1455 Lower Platta Unit). C) Green serpentinite crosscut by several generations of thick dark and
1456 thin green pale serpentine veins (Fal 18-08, Upper Platta unit). D) Massive dark green
1457 serpentinite (Tas 19-03) surrounded by a foliated pale green fibrous serpentinite (Tas 19-04,
1458 Tasna Unit). E) Massive green serpentinite from Totalp (Tot 19-01). F) Blueish serpentine
1459 fibers (Tot 19-04). G) Massive serpentinite sample crosscut by thick dark serpentine veins
1460 forming a mesh texture (Tot 19-05, Totalp Unit). H) Pyroxene relics in a massive dark green
1461 serpentinite (Tot 19-09).

1462 Figure 6: Photomicrographs of serpentinite thin sections showing the diversity of serpentine
1463 textures and their respective Raman spectra. P: point where the Raman spectra was done. All
1464 photos were taken under plane-polarized light (PPL; A, C) or cross-polarized light (XPL; B,
1465 D to H). A-B) First generation of serpentine (S1) made of lizardite, forming a typical mesh
1466 texture replacing olivine grains, or C) Bastite texture replacing primary pyroxene associated
1467 with magnetite grains. D) Bastite under XPL, cut by serpentine veins. E) Second generation
1468 of serpentine formed of polyhedral serpentine (S2) in clinopyroxene cleavage. F) Focus on S2
1469 serpentine vein in clinopyroxene cleavage showing the close association of this serpentine
1470 polysome and the formation of andradite grains. G) Third generation of serpentine (S3) with a
1471 typical banded vein texture made of polygonal serpentine crosscutting the bastite and mesh
1472 textures (S1). H) Polyhedral serpentine (S2) and andradite at rims of bastite (S1), cut by a
1473 banded vein (S3).

1474 Figure 7: A) Microphotography under plane polarized ligth (PPL) and cross polarized light
1475 (XPL) of a serpentinite sample from the lower Platta unit (Fal 18-06) showing the primary
1476 mesh texture (S1) crosscut by successive generations of serpentine veins. B) Focus on the
1477 primary serpentine mesh (S1) and associated magnetite grains crosscut by a thick fracture
1478 opened in pull-apart mode and filled by antigorite (S4) with a typical lamellar texture. C)-D)
1479 Focus of A) showing the chronology of formation of serpentine polysomes between lizardite
1480 mesh (S1), lamellar antigorite vein (S4), chrysotile crack-seal (S5) and late calcite veins.

1481 Figure 8: Representative microphotographs and schematical representations of the five
1482 different types of serpentines described in this study.

1483 Figure 9: Binary diagrams of bulk-rock compositions of serpentinites (recalculated in
1484 anhydrous basis) from Upper and Lower Platta, Tasna and Totalp showing MgO versus A)
1485 SiO_2, B) Fe_2O_3, C) CaO and D) Al_2O_3. Our data are compared to serpentinized peridotites
1486 from Platta and Malenco (Müntener et al., 2010), the Iberia Margin (Kodolànyi et al., 2012,
1487 Albers et al., 2021), Newfoundland, Mid Atlantic Ridge (MAR) and Hess Deep (Kodolányi et
1488 al.,, 2012). South West Indian Ridge (SWIR; Rouméjon et al., 2015). DMM: Depleted
1489 MORB Mantle Salters and Stracke, (2004).

1490 Figure 10: Bulk rock major element ratios of Al_2O_3/SiO_2 (anhydrous) versus MgO/SiO_2
1491 (anhydrous) of serpentinites. The blue line corresponds to the Terrestiral array (Jagoutz et al.,
1492 1979; Hart and Zindler, 1986). References are the same as in Figure 9.

1493 Figure 11: Mg# versus bulk-rock Ni (A) and Cr (B) concentrations (in µg/g) of serpentinites
1494 from Upper and Lower Platta, Tasna and Totalp. References are the same as in Figure 9.

1495 Figure 12: Representative rare earth element (REE) patterns normalized the Chondrite C1
1496 (left) and Primitive Mantle (PM)-normalized extended trace element patterns (right) of bulk-

rock serpentinites from Tasna, Totalp and Platta (green: Upper Platta, brown: Lower Platta), in comparison with bulk-rock serpentinites from Iberia (orange field) and Newfoundland (purple field), data from Kodolànyi et al., (2012).

Figure 13: A-C) Plots of Mg + Fe versus Si and B-D) Al versus Si. All cations are given in per formula units and are calculated based on 7 oxygen atoms in the serpentine formula, except for antigorite, which was calculated based on 6.823 oxygens and converted to 7 oxygens for comparison with other serpentine polysomes. Lz/Ctl: pure Mg lizardite/chrysotile endmember. Atg: pure Mg antigorite endmember. Data of Chenaillet serpentinites are from Schwartz et al., (2013) and those of Malenco antigorites are from Liu et al., (2020). Data from Iberia and newfoundland margin are from Vesin et al., (2023).

Figure 14: Comparison of Mg# values in the suite of serpentine minerals and veins from this study, independently of their respective locations. The thick bars illustrate the typical variation range of Mg# for each serpentine polysomes.

Figure 15: Fe_{tot} versus Mg of serpentine banded veins showing two tendencies depending on the nature of the serpentine polysomes (polygonal serpentine versus lizardite).

Figure 16: Representative rare earth element (REE) patterns normalized to C1-Chondrite (left) and PM-normalized extended trace element patterns (right) of serpentine minerals and veins depending on their localities. Blue field correspond to serpentinites Grade 0 (sub-greenschist facies conditions) from the Chenaillet (data from Lafay et al., 2013).

Figure 17: Rare earth element (REE) patterns normalized to C1-Chondrite (A-C), and extended trace elements patterns normalized to Primitive mantle (B-D) of serpentine minerals and veins of two serpentinite samples for the Lower (Mar 18-01) and the Upper Platta (Fal 18-06) units, showing U-shaped patterns with strong Eu positive anomaly. The compositions

of MARK serpentinites (Hole 1268A, Atlantic ridge) and hydrothermal fluids from Rainbow and Logatchev are shown for comparison (Paulick et al., 2006).

Figure 18: A) Li versus B and B) Cs versus Sr (µg/g) in the suite of serpentine minerals and veins from this study compared to other serpentinites from the Alps (Malenco Liu et al., (2020), Chenaillet Lafay et al., (2013) and from Iberia margin and Newfoundland margin from (Kodolànyi et al., 2012 and Vesin et al., 2023). The two black arrows illustrate the depletion trend of FME during the prograde Alpine metamorphism.

Figure 19: A) Simplified cross-section across an ocean continent transition (OCT) highlighting a long detachment fault continentwards (red) and flip-flop faults (blue) oceanwards (Figure modified from Gillard et al., 2016). B) Conceptual model proposed for the footwall vs. flip-flop mantle exhumation in OCT and the related C) type sequence of serpentinization: At proximal domains of the OCT, mantle exhumed along a continuous detachment fault, from ±6 km depth up to the seafloor, favors intense fluid-rock interactions and the development of a complete serpentinization sequence. At distal domains of the OCT, the mantle is exhumed discontinuously through asymmetric detachment faults (flip-flop). At this setting, one or more serpentine generations are missing, forming an incomplete serpentinization sequence.

Tables

Table 1: Location and description of the 40 serpentinized peridotites and serpentinites from the Eastern central Alps analyzed in this study. Mineral phases and their respective proportions (in wt.%) were obtained by X-ray diffraction on sample powders and estimated by Rietveld refinement using Profex software (Doebelin et al., 2015). Srp: serpentine, Mgt: magnetite, Cc: calcite, Chl: chlorite, And: andradite, Tr: tremolite, Ol: olivine, Cpx: clinopyroxene, Opx: orthopyroxene, Spl: spinel, b: banded; f: fibrous; g: granular; l: lamellar; s: spherical. *selected samples for detailed mineralogical and geochemical investigations.

Table 2: Bulk-rock major and trace element concentrations of the 40 serpentinized peridotites collected in the different units.

Table 3: Representative major element concentrations (in wt.%) of serpentine minerals and veins measured by µXRF. The structural formula for all serpentine minerals and veins have been calculated on the basis of 7 oxygens, except for antigorite for which calculations have been done on the basis of 6.823 oxygen, corresponding to m=17 in the antigorite general formulae $Mg_{3m-3}Si_{2m}O_{5m}(OH)_{4m-6}$.

Table 4: Representative trace element concentrations (in ppm) of serpentine minerals measured by HR-LA-ICP-MS.

Supplementary materials

Supplementary Figure 1: Serpentinites bulk-rock REE and spiders diagrams for all samples analyzed in this study.

Supplementary Table 1: In-situ major element concentrations measured in serpentine minerals and veins in all samples.

Supplementary Table 2: In-situ trace element concentrations measured in serpentine minerals and veins in all samples.

Supplementary Table 3: Bulk-rock major and trace element concentrations measured in UB-N standard by µXRF and ICP-MS.

Table 1: Location and description of the 40 serpentinized peridotites and serpentinites from the Eastern central Alps analyzed in this study. Mineral phases and their respective proportions (in wt.%) were obtained by X-ray diffraction on sample powders and estimated by Rietveld refinement using Profex software (Doebelin et al., 2015). Srp: serpentine, Mgt: magnetite, Cc: calcite, Chl: chlorite, And: andradite, Tr: tremolite, Ol: olivine, Cpx: clinopyroxene, Opx: orthopyroxene, Spl: spinel, b: banded; f: fibrous; g: granular; l: lamellar; s: spherical. *selected samples for detailed mineralogical and geochemical investigations.

Unit	Sample	Texture	Latitude	Longitude	Srp	Mag	Cal	Clc	Adr	Tr	Ol	Cpx	Opx	Spl	Pseudomorphic textures	Veins texture	Antigorite
Rietveld references					chrysotile 2M1 ICCD, lizardite 1TMellini	profex-BGMN database	profex-BGMN database	profex-BGMN database	profex-BGMN database	profex-BGMN database	Forsterite profex-BGMN database	diopside profex-BGMN database	enstatite profex-BGMN database	profex-BGMN database			
Upper Platta	Fal18-02a*	Vein	46°32’51.17"N	9°40'9.42"E	99.9	-	-	-	-	-	-	-	-	-		b, g, s	
	Fal18-02b	Massive+veins	46°32’51.17"N	9°40'9.42"E	97.8	1.8	<1	-	-	-	-	-	-	<1	X	b	

	Fal18-03*	Massive	46°32’51.08"N	9°40’10.14"E	99.6	<1	<1	-	-	-	-	-	-	-	X	b, g, l, s	
	Fal18-04	Vein	46°32’51.12"N	9°40'9.94"E	99.9	-	-	-	-	-	-	-	-	-		b	
	Fal18-05	Vein	46°32’51.13"N	9°40’9.92"E	99.7	<1	-	-	-	-	-	-	-	-		b	
	Fal18-06*	Massive	46°32’51.25"N	9°40’10.02"E	95.0	5	<1	-	-	-	-	-	-	<1	X	l, f	X
	Fal18-07	Massive	46°32’51.25"N	9°40’10.02"E	81.0	1.3	-	-	-	-	<1	10.9	6.1	<1	X	b, g	
	Fal18-08	Massive + veins	46°32’56.63"N	9°40’7.09"E	97.0	2.3	-	-	-	-	-	-	-	-		b, g	
	Fal18-09	Massive	46°32’56.63"N	9°40’7.09"E	99.8	<1	-	-	-	-	-	-	-	<1	X	f	
	Fal18-	Massive	46°32’56.63"N	9°40’7.09"E	98.9	1.1	-	-	-	-	-	-	-	<1		b, g, f	

	10	+ve ins															
Lower Platta	Fal18-11*	Massive	46°32’44.74" N	9°39’38.65"E	99.3	<1	-	-	-	-	-	-		<1	X	f	
	Fal18-12	Massive	46°32’43.75" N	9°39’33.72"E	85.7	<1	1.6	8.1	-	4.5	-	-	-	-	X	f	
	Fal18-13*	Massive	46°32’42.24" N	9°39’34.87"E	99.5	<1	<1	-	-	-	-	-	-	<1	X	b, f, s	
	Fal18-14	Massive	46°32’29.95" N	9°39'40.02" E	99.9	<1	-	-	-	-	-	-	-	<1	X	f	
	Mar18-01*	Massive +ve ins	46°30’19.19" N	9°37’41.28"E	98.8	1.2	<1	-	-	-	-	-			X	b, l, f	X
Total p	Tot19-01	Massive	46°49' 56.97" N	9°48' 18.71" E	58.9	1	-	-	-	-	30.2	7.6	2.2	<1	X	b, s	
	Tot19-02	Massive	46°49' 56.97" N	9°48' 18.71" E	91.1	-	-		2.3	-	<1	6.8			X	b, s	

	*																
	Tot19-03a*	Massive+veins	46°50'18.49" N	9°48'13.85" E	92.0	<1	-	-	3	-	-	3.5	<1	<1	X	b	
	Tot19-03b	Vein	46°50'18.55" N	9°48'13.94" E	99.9	-	-	-	-	-	-	-	-	-		b	
	Tot19-04*	Massive+veins	46°50'18.40" N	9°48'14.23" E	96.7	0.38	-					2.92			X	b,s	
	Tot19-05	Massive	46°50'18.40" N	9°48'14.23" E	90.8	<1	-	-	-	-	<1	5.8	1.8	<1	X	b,s	
	Tot19-07*	Massive	46°50'19.58" N	9°48'16.68" E											X	b	
	Tot19-09*	Massive	46°54'56.61" N	9°51'27.98" E	97.1	<1	-	-	-	-	1.5	<1	-	<1	X	b,s	
	Tot19-1	Foliated	46°50'23.31" N	9°48'24.48" E	95.9	<1	-	-	3.7	-	-	-	-	-	X	s	

	0a																
	Tot19-10b*	Massive	46°50'24.37" N	9°48'26.62" E	98.7	<1	<1	-	-	-	-	-	-	-	X	b, s	
Tasna	Tas19-01	Massive	46°50’17.28’’ N	10°15'37.79" E	94.0	1.3	<1	-	-	2.2	-	-	-	<1	X	b	
	Tas19-02*	Foliated	46°49’24.33" N	10°15'6.11" E	98.7	<1	<1	-	-	-	-	-	-	<1	X	b, g, f	X
	Tas19-03*	Massive	46°49'35.23" N	10°15'4.26" E	96.3	<1	<1	-	-	<1	<1	1.3	-	-	X	b, g, f, s	
	Tas19-04*	Massive + veins	46°49'35.08" N	10°15'4.12" E	94.1	<1	<1	-	<1	1.2	-	3.3	-	-	X	b, g, l	X
	Tas19-06a	Vein	46°49'34.70" N	10°15'4.69" E	99.9	-	-	-	<1	-	-	-	-	-		b	
	Tas19-06	Massive + ve	46°49'34.70" N	10°15'4.69" E	98.2	<1	<1	-	-	-	-	-	-	-	X	b	

	b	ins															
	Tas19-07	Vein	46°49'34.73" N	10°15'5.02" E	99.9	-	-	-	-	-	-	-	-	-		-	
	Tas19-08*	Massive+veins	46°49'34.59" N	10°15'4.74" E	99.4	<1	<1	-	-	-	-	<1	-	-	X	b	
	Tas19-09	Vein	46°49'34.38" N	10°15'4.30" E	99.9	-	-	-	-	-	-	-	-	-		-	
	Tas19-10*	Massive+viens	46°49'27.28" N	10°16'9.17" E	98.5	<1	-	-	-	-	-	2.7	-	<1	X	b	
	Tas19-11	Vein	46°49'54.23" N	10°14'56.57" E	97.9	<1	-	-	-	-	<1	-	-	<1	X	b,l,s	
	Tas19-12	Massive	46°49'54.06" N	10°14'56.78" E	98.7	<1	<1	-	-	-	-	<1	-	-	X	b,f,s	
	Tas19-13	Massive	46°50'0.71" N	10°15'9.73" E	99.7	<1	-	-	-	-	-	-	-	-	X	b,f	
	Tas	Mas	46°50'	10°15'	90.1	<1	<1	-	-	-	2	6.7	-	-	X	b,f,	

	19-14	sive	1.07" N	9.70" E												s	
	Tas19-15	Massive	46°50'1.07" N	10°15'9.70" E	99.5	<1	-	-	-	-	-	-	-	-	X	b	

Table 2: Bulk-rock major and trace element concentrations of the 40 serpentinized peridotites colleced in the different units.

Unit	Sample	SiO_2	TiO_2	Al_2O_3	Fe_2O_3	MnO	MgO
Upper Platta	Fall-18-02a	40.18	0.110	1.90	3.50	0.06	39.
	Fall-18-02b	36.13	0.110	2.45	10.42	0.12	35.
	Fall-18-03	38.52	0.113	2.26	8.32	0.17	36.
	Fall-18-04	41.13	0.102	1.33	3.09	0.08	39.
	Fall-18-05	38.82	0.081	2.08	10.60	0.18	34.
	Fall-18-06	39.71	0.011	0.21	7.37	0.12	37.
	Fall-18-07	39.85	0.255	3.14	8.59	0.11	33.
	Fall-18-08	38.15	0.041	1.66	9.26	0.10	38.
	Fall-18-09	39.21	0.074	3.33	6.92	0.12	36.
	Fall-18-10	38.09	0.041	1.41	8.41	0.13	38.
Lower Platta	Fall-18-11	39.91	0.027	0.32	7.37	0.10	38.
	Fall-18-12	35.50	0.107	3.29	8.79	0.13	30.
	Fall-18-13	39.06	0.076	3.00	9.96	0.13	33.
	Fall-18-14	38.84	0.074	2.16	8.78	0.12	37.
	Nar-18-01	38.20	0.022	0.88	9.82	0.15	36.
Total p	Tot-19-01	38.66	0.155	0.89	8.07	0.13	34.
	Tot-19-02	38.62	0.119	3.09	7.83	0.12	32.
	Tot-19-03a	38.38	0.098	2.32	8.52	0.13	35.
	Tot-19-03b	38.00	0.011	5.77	8.60	0.08	37.
	Tot-19-04	38.65	0.117	2.80	8.39	0.13	34.
	Tot-19-05	38.13	0.119	2.99	8.46	0.13	33.
	Tot-19-07	38.19	0.208	2.90	9.46	0.11	32.
	Tot-19-09	38.36	0.181	3.09	8.58	0.14	35.
	Tot-19-10a	37.20	0.118	2.81	8.62	0.12	34.
	Tot-19-10b	38.52	0.116	2.76	8.36	0.12	36.
Tasna	Tas-19-01	n.d	n.d	n.d	n.d	n.d	n.d
	Tas-19-02	37.50	0.097	3.31	8.16	0.13	33.
	Tas-19-03	38.73	0.133	2.91	8.46	0.13	33.
	Tas-19-04	37.03	0.112	3.02	9.22	0.12	34.
	Tas-19-05	38.52	0.113	2.68	9.06	0.12	33.
	Tas-19-06a	40.22	0.027	2.40	9.91	0.07	34.
	Tas-19-06b	38.44	0.071	1.87	8.50	0.13	36.
	Tas-19-07	39.57	0.019	3.57	8.06	0.07	33.
	Tas-19-08	38.61	0.039	1.97	8.99	0.13	34.
	Tas-19-09	40.70	0.033	1.88	9.97	0.10	33.
	Tas-19-10	38.71	0.088	2.15	7.92	0.12	36.
	Tas-19-11	38.27	0.133	2.55	7.98	0.13	36.
	Tas-19-12	38.54	0.122	2.74	8.60	0.12	34.
	Tas-19-13	38.79	0.106	2.21	7.94	0.08	37.
	Tas-19-14	39.98	0.122	2.29	9.03	0.12	32.
	Tas-19-15	37.81	0.022	0.38	7.57	0.08	40.

	53	06	86	65	89	60	15	17	83	20	80	19	82	08	99	00	49	66	35	50	85	92	38	09	69		48	84	44	52	45	94	62	43	36	29	36	01	97	66	03
CaO	0.07	0.03	0.11	0.00	0.20	0.44	3.61	0.00	0.02	0.01	0.00	7.46	0.21	0.03	0.00	3.32	5.99	1.71	0.02	2.89	3.07	2.79	1.15	3.17	0.19	n.d	2.08	2.43	0.05	0.18	0.78	0.41	0.35	0.22	0.10	0.92	0.02	0.28	0.10	3.83	0.09
K_2O	b.d.l	b.d.l	b.d.l	b.d.l	b.d.l	b.d.l	0.01	b.d.l	b.d.l	b.d.l	b.d.l	b.d.l	b.d.l	b.d.l	b.d.l	b.d.l	b.d.l	b.d.l	b.d.l	b.d.l	b.d.l	b.d.l	b.d.l	b.d.l	b.d.l	n.d	b.d.l	b.d.l	b.d.l	b.d.l	b.d.l	b.d.l	b.d.l	b.d.l	b.d.l	b.d.l	b.d.l	b.d.l	b.d.l	b.d.l	b.d.l
Na_2O	0.24	0.08	0.11	0.12	0.08	0.49	0.00	0.06	0.20	0.17	0.16	0.04	0.45	0.24	0.03	0.03	0.00	0.14	0.00	0.07	0.08	0.14	0.10	0.03	0.00	n.d	0.05	0.18	0.09	0.22	0.52	0.13	0.08	0.00	0.14	0.15	0.50	0.00	0.19	0.07	0.20
Cr_2O_3	0.01	0.48	0.42	0.02	0.49	0.33	0.36	0.38	0.45	0.52	0.43	0.41	0.44	0.42	0.29	0.44	0.47	0.43	0.01	0.40	0.35	0.45	0.38	0.41	0.34	n.d	0.41	0.44	0.45	0.45	0.04	0.30	0.03	0.44	0.04	0.33	0.49	0.36	0.41	0.47	0.35
NiO	0.02	0.29	0.26	0.03	0.27	0.26	0.22	0.26	0.29	0.30	0.00	0.22	0.28	0.27	0.25	0.22	0.17	0.26	0.02	0.24	0.22	0.24	0.22	0.21	0.21	n.d	0.00	0.00	0.00	0.00	0.00	3.38	0.00	0.00	0.00	0.25	0.14	0.24	0.25	0.32	0.27
LOI	14.74	13.34	13.75	15.02	13.20	13.80	10.51	12.84	13.06	13.58	12.74	13.84	13.20	12.84	13.84	12.04	10.87	12.17	13.24	11.92	12.66	11.82	12.74	13.08	13.52	n.d	12.72	11.67	14.07	12.74	13.05	12.73	13.07	12.81	14.07	13.19	13.22	12.91	12.89	12.30	13.30
Total	100.36	98.51	100.91	100.50	100.88	100.35	100.12	100.92	100.51	100.86	99.85	100.05	100.65	100.84	100.48	100.15	100.15	99.77	100.51	100.14	100.12	100.15	100.00	100.03	100.88	n.d	99.92	99.92	100.60	100.61	100.45	103.91	100.42	100.70	100.38	100.12	100.80	100.92	100.89	100.17	100.10
Mg#	0.95	0.86	0.89	0.96	0.85	0.90	0.87	0.88	0.90	0.89	0.90	0.86	0.86	0.88	0.87	0.88	0.88	0.88	0.92	0.88	0.88	0.86	0.88	0.88	0.89	n.d	0.89	0.88	0.88	0.88	0.95	0.89	0.95	0.88	0.95	0.89	0.89	0.88	0.90	0.86	0.90
Trace (p																																									

pm)																																								
Li	8.2	11.9	21.8	5.7	3.0	7.2	10.4	4.6	7.3	2.4	15.4	10.4	10.6	11.3	2.8	4.5	3.8	2.8	2.4	0.9	5.1	10.8	10.4	24.7	24.6	14.3	10.7	1.3	7.4	8.5	5.9	3.6	1.2	2	b.d.l	3.9	4.9	38	7	11.8	1.3
B	15.1	40.4	98.5	26.7	26.0	82.7	113.8	56.5	66.8	73.0	54.4	42.4	152.4	50.8	46.8	6.5	6.0	n.d	n.d	n.d	13.3	106.7	68.6	48.4	43.0	52.9	39.6	37.1	43.14	31.29	4.25	20.69	4.81	15.81	9.03	12.28	38.98	92.9	90.87	115.61	100.76
V*	9.2	48.7	45.6	7.9	61.1	1.0	75.2	23.3	99.3	21.4	1.1	73.4	105.5	52.9	6.7	65.2	78.9	52.8	3.4	62.3	62.9	70.1	63.3	57.6	58.8	59.6	62.2	66.3	62.18	62.24	3.40	23.56	11.26	19.89	8.50	37.15	58.11	62.23	28.37	57.91	4.65
Cr	33.4	3170.0	2480.0	12.2	364.0	2440.0	2170.0	2440.0	2750.0	3020.0	3070.0	2270.0	2760.0	2320.0	1840.0	2630.0	2790.0	1290.0	29.0	2610.0	2300.0	2420.0	2230.0	2300.0	1950.0	2340.0	2420.0	2600.0	2420	2850	166	1780	124	2370	109	2010	2650	2840	2150	2070	2310
Mn	b.d.l	b.d.l	b.d.l	566.0	b.d.l	b.d.l	b.d.l	b.d.l	b.d.l	b.d.l	b.d.l	b.d.l	b.d.l	b.d.l	b.d.l	909.0	912.0	629.0	441.0	931.0	887.0	873.0	833.0	962.0	862.0	806.0	881.0	771.0	854	831	452	832	394	824	521	853	852	786	593	790	687
Co	47.4	116.0	99.1	29.0	33.2	95.1	82.1	94.8	117.0	98.4	105.0	163.0	104.0	101.0	91.9	96.7	88.6	56.3	14.2	105.0	98.5	94.9	106.0	93.0	94.9	101.0	86.5	112.0	89.7	104	8.04	100	6.03	94.4	11.9	83.8	66.8	105	92.2	88.6	106
Ni	147.0	2050.0	1810.0	316.0	347.0	1850.0	1370.0	1650.0	1940.0	1840.0	2030.0	1540.0	1910.0	1780.0	1780.0	1650.0	1470.0	942.0	120.0	1940.0	1700.0	1773.0	1880.0	1660.0	1720.0	1840.0	1610.0	2100.0	1660	1900	223	1968	110	1800	483	1770	1000	2140	1780	1660	2060
Ni*	166.5	2242.3	2035.6	272.7	2192.1	2062.1	1736.2	2004.2	2307.3	2379.3	2362.2	1742.0	2164.3	2141.1	1939.9	1717.5	1358.2	2011.6	145.9	1886.5	1724.3	1912.4	1742.2	1675.3	1689.4	1905.0	1672.7	1838.6	2245	2030	237	2053	138	2166	602	1998	1108	1879	1948	2526	2100
Cu	0.9	9.9	13.	5.9	1.2	5.4	16.	10.	16.	12.	8.9	7.8	14.	18.	13.	36.	25.	2.1	10.	30.	27.	25.	25.	15.	25.	13.	2.9	26.	21.	23.	2.7	8.5	0.9	7.5	8.3	10.	11.	28.	10.	20.	2.2

			6				5	8	8	7			3	8	3	1	9		5	8	3	8	7	8	1	1		6	8	3				8	5	8	7	9	8	7	8
Zn	11.3	43.5	39.2	26.5	23.4	27.4	38.8	46.5	38.1	52.1	50.1	40.4	59.9	51.7	104.0	59.2	51.0	16.9	28.5	54.6	47.9	51.2	50.5	51.5	40.0	47.1	41.9	48.1	40.7	55.5	39	38.4	25.9	55.6	25.6	40.9	61.4	41.6	37.4	37.5	48.9
As	b.d.l	b.d.l	8.0	b.d.l	b.d.l	2.1	b.d.l	b.d.l	17.0	b.d.l	b.d.l	38.0	b.d.l	10.0	2;àà	b.d.l	b.d.l	b.d.l	b.d.l	b.d.l	b.d.l	b.d.l	b.d.l	b.d.l	b.d.l	b.d.l	b.d.l	b.d.l	b.d.l	b.d.l	b.d.l	b.d.l	b.d.l	b.d.l	b.d.l	b.d.l	b.d.l	b.d.l	b.d.l	b.d.l	b.d.l
Rb	0.1	0.2	0.4	0.2	0.1	0.5	1.0	0.1	0.6	0.1	0.1	0.6	1.2	0.4	0.6	0.1	0.0	0.0	0.0	0.0	0.2	0.8	0.6	0.1	0.2	0.6	0.6	0.2	0.32	0.305	0.08	b.d.l	0.04	0.015	0.079	0.028	0.031	0.358	0.039	0.138	0.008
Sr	0.7	2.4	6.1	0.9	0.5	4.1	13.4	1.6	3.5	1.4	1.5	13.5	5.0	2.0	4.4	8.9	5.5	1.1	0.4	9.6	12.4	13.9	4.7	3.6	2.0	18.8	28.4	1.6	2.82	5.05	0.50	1.60	0.40	0.80	0.54	1.33	1.59	17.00	3.74	3.68	1.02
Y	0.4	1.2	1.7	0.3	1.4	0.3	3.1	0.6	1.3	0.5	0.3	2.3	1.4	1.4	0.3	2.5	3.7	1.5	0.1	2.9	2.8	2.8	2.6	2.5	2.3	1.7	1.6	2.2	2.09	2.55	0.235	0.942	0.139	0.838	0.238	1.29	0.978	1.63	1.11	1.7	0.152
Zr	1.7	2.9	3.0	6.3	2.3	0.7	6.0	1.1	0.8	0.8	0.6	2.9	0.8	0.5	0.4	2.8	3.9	2.8	0.6	3.1	4.0	6.3	4.7	4.8	3.3	7.9	1.0	6.0	0.84	1.38	0.48	1.22	1.31	0.45	0.18	0.47	0.84	1.38	0.67	1.56	0.53
Nb	1.2	0.9	0.5	0.1	0.4	0.3	0.3	0.2	0.1	0.1	0.1	0.1	0.0	0.0	0.1	0.0	0.0	0.0	0.0	b.d.l	0.3	0.0	0.0	0.0	0.0	0.1	0.0	0.0	b.d.l	0.88	0.02	b.d.l	b.d.l	b.d.l	0.019	0.01	0.008	b.d.l	0.015	b.d.l	0.013
Mo	0.3	0.3	0.2	0.0	0.1	0.2	0.2	0.2	0.1	0.2	0.1	b.d.l	b.d.l	b.d.l	b.d.l	0.0	0.0	0.0	0.0	0.1	0.1	0.1	0.1	0.1	0.1	0.1	0.1	0.1	0.04	0.28	0.03	0.05	0.02	0.05	0.03	0.04	0.02	0.06	0.09	0.03	0.05
Cd	b.d.l	0.0	0.0	0.0	0.1	0.0	0.1	0.0	0.1	0.0	0.0	0.0	0.0	0.0	0.0	0.0	0.0	b.d.l	0.1	0.0	0.0	0.0	0.0	0.0	0.0	0.0	0.0	0.0	0.019	0.017	0.02	0.011	0.017	0.008	0.024	0.032	0.017	0.025	0.011	0.01	0.008
Sn	0.2	0.1	0.1	0.1	0.1	0.2	0.2	0.1	0.1	0.1	0.1	0.1	0.1	0.0	0.4	0.1	0.1	0.1	0.1	0.1	0.1	0.1	0.2	0.2	0.1	0.1	0.1	0.1	0.11	0.17	0.09	0.04	0.07	0.05	0.06	0.07	0.09	0.14	0.06	0.07	0.15

Sb	0.1	0.2	0.1	0.0	0.1	0.1	b.d.l	b.d.l	0.2	0.1	0.1	0.1	0.1	0.1	0.1	b.d.l	b.d.l	b.d.l	b.d.l	b.d.l	b.d.l	0.0	0.0	0.1	0.1	0.1	0.0	0.0	0.039	0.082	0.012	b.d.l	0.009	0.005	0.012	0.006	0.008	0.057	0.112	0.012	0.039
Cs	0.2	0.4	1.0	0.3	0.0	1.3	1.7	0.1	0.6	0.0	0.3	1.1	3.0	0.6	0.5	0.0	0.0	b.d.l	0.0	0.0	0.1	0.2	0.2	0.0	0.0	1.1	1.3	0.1	0.293	0.247	b.d.l	0.023	b.d.l	0.011	0.007	0.005	0.008	0.966	0.101	0.15	b.d.l
Ba	0.7	2.5	2.8	1.6	1.2	1.3	3.3	1.2	2.2	0.8	0.5	1.6	1.9	0.8	1.6	0.1	b.d.l	0.9	1.7	0.3	0.6	b.d.l	1.0	1.0	0.6	2.7	1.5	0.9	0.58	1.59	1	0.3	0.9	0.33	2.45	1.94	1.93	5.31	2.67	1.23	0.14
La	0.0	0.1	0.1	0.1	0.0	0.1	0.2	0.1	0.0	0.0	0.1	0.2	0.0	b.d.l	0.2	0.0	0.0	0.1	0.1	0.1	0.6	0.1	0.1	0.1	0.1	0.0	0.1	0.0	0.013	1.63	0.071	0.051	0.026	0.008	0.118	0.017	0.028	0.047	0.026	0.013	0.042
Ce	0.1	0.2	0.3	0.1	0.1	0.2	0.7	0.1	0.0	0.1	0.2	0.6	0.0	0.0	0.4	0.2	0.3	0.2	0.2	0.4	1.4	0.4	0.4	0.4	0.4	0.1	0.1	0.1	0.043	2.77	0.1	0.081	0.045	0.018	0.143	0.024	0.035	0.197	0.079	0.018	0.186
Pr	0.0	0.0	0.1	0.0	0.0	0.0	0.1	0.0	0.0	0.0	0.0	0.1	b.d.l	b.d.l	0.0	0.1	0.1	0.1	0.0	0.1	0.2	0.1	0.1	0.1	0.1	0.0	0.0	0.0	0.018	0.279	0.013	0.01	0.006	0.005	0.027	0.007	0.011	0.041	0.016	0.008	0.038
Nd	0.1	0.3	0.3	0.1	0.2	0.2	0.8	0.1	0.1	0.0	0.1	0.5	0.0	0.1	0.2	0.4	0.5	0.3	0.1	0.5	0.9	0.6	0.5	0.5	0.5	0.1	0.1	0.2	0.173	1.06	0.065	0.079	0.031	0.059	0.121	0.083	0.099	0.275	0.122	0.101	0.222
Sm	0.0	0.1	0.1	0.0	0.1	0.0	0.3	0.0	0.1	0.0	0.0	0.2	0.1	0.1	0.0	0.2	0.3	0.1	0.0	0.2	0.3	0.2	0.2	0.2	0.2	0.1	0.1	0.1	0.126	0.23	0.019	0.045	0.012	0.043	0.03	0.071	0.068	0.129	0.063	0.087	0.056
Eu	0.0	0.1	0.1	0.0	0.0	0.1	0.1	0.0	0.0	0.0	0.0	0.1	0.1	0.0	0.1	0.1	0.1	0.1	0.0	0.1	0.1	0.1	0.1	0.1	0.1	0.0	0.0	0.0	0.073	0.057	0.017	0.013	0.006	0.015	0.007	0.018	0.023	0.062	0.026	0.042	0.018
Gd	0.0	0.2	0.2	0.0	0.2	0.0	0.5	0.1	0.1	0.0	0.1	0.3	0.1	0.1	0.0	0.3	0.4	0.2	0.0	0.3	0.4	0.4	0.3	0.3	0.3	0.2	0.2	0.2	0.239	0.332	0.034	0.101	0.019	0.085	0.04	0.152	0.123	0.207	0.118	0.187	0.041

Tb	0.0	0.0	0.0	0.0	0.0	0.0	0.1	0.0	0.0	0.0	0.0	0.1	0.0	0.0	0.0	0.1	0.1	0.0	0.0	0.1	0.1	0.1	0.1	0.1	0.1	0.0	0.0	0.0	0.048	0.059	0.006	0.018	0.003	0.018	0.006	0.03	0.024	0.039	0.024	0.037	0.005
Dy	0.1	0.2	0.3	0.1	0.3	0.0	0.6	0.1	0.2	0.1	0.1	0.4	0.2	0.2	0.1	0.4	0.6	0.3	0.0	0.5	0.5	0.5	0.5	0.4	0.4	0.3	0.3	0.4	0.371	0.434	0.037	0.156	0.023	0.147	0.043	0.228	0.181	0.289	0.197	0.303	0.032
Ho	0.0	0.1	0.1	0.0	0.1	0.0	0.1	0.0	0.1	0.0	0.0	0.1	0.1	0.1	0.0	0.1	0.1	0.1	0.0	0.1	0.1	0.1	0.1	0.1	0.1	0.1	0.1	0.1	0.083	0.096	0.007	0.033	0.004	0.033	0.008	0.051	0.04	0.062	0.044	0.068	0.006
Er	0.0	0.2	0.2	0.0	0.2	0.0	0.4	0.1	0.2	0.1	0.0	0.3	0.2	0.2	0.0	0.3	0.5	0.2	0.0	0.4	0.3	0.4	0.3	0.3	0.3	0.2	0.2	0.3	0.265	0.307	0.022	0.116	0.015	0.11	0.024	0.163	0.124	0.201	0.141	0.217	0.02
Tm	0.0	0.0	0.0	0.0	0.0	b.d.l	0.1	0.0	0.0	0.0	b.d.l	0.0	0.0	0.0	b.d.l	0.0	0.1	0.0	0.0	0.0	0.0	0.1	0.0	0.0	0.0	0.0	0.0	0.0	0.039	0.046	0.003	0.017	0.002	0.016	0.003	0.023	0.018	0.027	0.022	0.033	0.003
Yb	0.1	0.2	0.2	0.0	0.2	0.0	0.4	0.1	0.2	0.1	0.0	0.3	0.2	0.2	0.0	0.3	0.5	0.2	0.0	0.3	0.3	0.4	0.3	0.3	0.3	0.2	0.2	0.3	0.273	0.341	0.026	0.133	0.018	0.121	0.025	0.168	0.13	0.208	0.158	0.246	0.029
Lu	0.0	0.0	0.0	0.0	0.0	b.d.l	0.1	0.0	0.0	0.0	b.d.l	0.0	0.0	0.0	0.0	0.0	0.1	0.0	0.0	0.0	0.1	0.1	0.0	0.0	0.0	0.0	0.0	0.0	0.041	0.052	0.004	0.02	0.003	0.018	0.004	0.028	0.02	0.03	0.024	0.04	0.005
Hf	0.2	0.2	0.2	2.3	0.1	0.0	0.3	0.1	0.1	0.2	0.1	0.2	0.1	0.1	0.1	0.3	0.3	0.2	0.1	0.2	0.2	0.9	0.4	0.4	0.1	1.3	0.1	0.9	0.073	0.074	0.09	0.68	0.4	0.032	b.d.l	0.042	0.081	0.067	0.029	0.301	0.02
Ta	0.0	0.0	0.0	0.0	0.0	0.0	0.0	0.0	0.0	0.0	0.0	0.0	0.0	0.0	0.0	0.0	0.0	0.0	b.d.l	b.d.l	0.0	0.0	0.0	0.0	0.0	0.0	0.0	0.0	b.d.l	0.038	b.d.l	b.d.l	0.005	b.d.l	b.d.l	b.d.l	b.d.l	b.d.l	b.d.l	b.d.l	b.d.l
Pb	0.1	0.2	0.3	0.8	2.5	0.3	0.3	0.1	1.0	1.0	0.2	0.5	0.2	0.2	0.4	0.0	0.1	0.0	6.0	0.1	0.1	b.d.l	0.1	0.3	0.1	0.2	0.2	0.2	0.237	0.162	0.58	b.d.l	0.53	0.056	0.306	0.041	0.274	0.515	0.413	b.d.l	0.132

Th	0.6	0.3	0.2	0.2	0.1	0.1	0.1	0.1	0.1	0.4	0.1	0.1	0.1	0.0	0.0	0.1	0.0	0.0	0.0	0.0	0.1	0.0	0.1	0.0	0.0	0.1	0.0	0.1	0.014	0.104	0.03	0.01	0.01	0.009	0.013	0.009	0.009	0.005	0.01	0.012	0.005
U	b.d.l	b.d.l	b.d.l	0.0	b.d.l	b.d.l	b.d.l	b.d.l	b.d.l	b.d.l	b.d.l	0.5	b.d.l	b.d.l	b.d.l	0.0	0.0	b.d.l	0.0	b.d.l	0.0	0.0	0.0	0.0	0.0	0.0	0.0	b.d.l	0.003	0.049	0.053	b.d.l	0.013	0.001	0.032	0.111	0.003	-b.d.l	0.006	0.001	0.028

Table 3: Representative major element concentrations (in wt.%) of serpentine minerals measured by µXRF. The structural formula for all serpentine minerals and veins have been calculated on the basis of 7 oxygens, except for antigorite for which calculations have been done on the basis of 6.823 oxygen, corresponding to m=17 in the antigorite general formulae Mg 3m−3 Si 2mO 5m(OH) 4m−6.

Unit	Upper Platta					Lower Platta					Totalp				Tasna			
Sample	Fal18-06	Fal18-02	Fal18-03	Fal18-06	Fal18-06	Mar18-01	Mar18-01	Mar18-01	Mar18-01	Mar18-01	Tot19-02	Tot19-02	Tot19-02	Tot19-07	Tas19-02	Tas19-03	Tas19-08	Tas19-02
Texture	mesh (S1)	bastite (S1)	banded vein (S3)	lamellar vein (S4)	fibrous vein (S5)	mesh (S1)	bastite (S1)	banded vein (S3)	lamellar vein (S4)	fibrous vein (S5)	mesh (S1)	bastite (S1)	spherical vein (S2)	banded vein (S3)	mesh (S1)	bastite (S1)	banded vein (S3)	lamellar vein (S4)
Type	lizardite	lizardite	polygonal	antigorite	chrysotile	lizardite	lizardite	lizardite	antigorite	chrysotile	lizardite	lizardite	polyhedral	polygonal	lizardite	lizardite	lizardite	antigorite
Primary minerals	ol	opx	-	-	-	ol	opx	-	-	-	ol	cpx	-	-	ol	cpx	-	-
SiO_2	41.54	39.40	41.24	42.87	41.41	40.52	40.14	42.10	42.26	42.28	40.57	38.67	40.70	42.51	42.05	40.68	42.50	43.29
TiO_2	0.03	0.09	0.66	0.03	0.02	0.04	0.04	0.04	0.03	0.03	0.03	0.09	0.03	0.04	0.25	0.10	0.04	0.05

Al_2O_3	0.27	4.70	2.12	0.23	0.29	1.34	1.18	0.67	0.96	0.88	1.98	5.52	3.53	0.89	0.64	2.79	1.50	0.97	
Fe_2O_3	5.14	3.91	4.01	4.57	4.60	5.02	5.00	3.06	4.26	3.82	4.90	4.64	2.79	2.53	4.02	4.14	1.57	3.46	
MnO	0.13	0.09	0.20	0.21	0.16	0.16	0.14	0.12	0.27	0.18	0.12	0.11	0.09	0.11	0.16	0.11	0.07	0.13	
MgO	39.80	38.12	38.39	38.94	41.09	39.59	39.90	41.07	38.93	39.84	39.17	37.52	39.59	40.83	39.42	38.22	40.75	38.38	
CaO	0.09	0.17	0.61	0.06	0.18	0.06	0.06	0.07	0.06	0.08	0.15	0.54	0.44	0.21	0.57	0.85	1.19	0.43	
K_2O	b.d.l	b.d.l	b.d.l	b.d.l	b.d.l	b.d.l	b.d.l	b.d.l	b.d.l	b.d.l	b.d.l	b.d.l	b.d.l	b.d.l	b.d.l	b.d.l	b.d.l	b.d.l	
Na_2O	b.d.l	b.d.l	b.d.l	b.d.l	b.d.l	b.d.l	b.d.l	b.d.l	b.d.l	b.d.l	b.d.l	b.d.l	b.d.l	b.d.l	b.d.l	b.d.l	b.d.l	b.d.l	
Cr_2O_3	0.09	0.79	0.14	0.03	0.06	0.48	0.91	0.07	0.05	0.07	0.03	0.21	0.02	0.03	0.07	0.36	0.01	0.05	
NiO	0.32	0.06	0.02	0.08	0.05	0.20	0.14	0.03	0.08	0.05	0.43	0.09	b.d.l	b.d.l	0.15	0.06	0.02	0.10	
Total	87.39	87.29	87.39	87.02	87.32	87.38	87.47	87.21	86.91	87.22	87.36	87.32	87.19	87.16	87.32	87.27	87.20	86.88	
p.f.u																			
Si	1.968	1.855	1.941	1.978	1.953	1.922	1.907	1.971	1.947	1.985	1.922	1.829	1.904	1.984	1.981	1.920	1.980	1.980	
Ti	0.001	0.003	0.024	0.001	0.001	0.001	0.001	0.001	0.001	0.001	0.001	0.003	0.001	0.001	0.009	0.004	0.001	0.002	
Al	0.015	0.261	0.118	0.013	0.016	0.075	0.066	0.037	0.051	0.049	0.110	0.308	0.195	0.049	0.036	0.155	0.058	0.053	
Fe^{2+}	0.180	0.154	0.105	0.164	0.144	0.189	0.162	0.120	0.174	0.150	0.194	0.184	0.109	0.099	0.110	0.162	0.020	0.116	
Fe^{3+}	0.022	0.000	0.048	0.011	0.014	0.009	0.034	0.000	0.000	0.000	0.000	0.000	0.000	0.000	0.044	0.001	0.038	0.015	

Mn	0.005	0.004	0.008	0.008	0.007	0.006	0.006	0.005	0.012	0.007	0.005	0.005	0.003	0.005	0.006	0.004	0.003	0.005	
Mg	2.811	2.678	2.694	2.679	2.889	2.799	2.826	2.867	2.663	2.789	2.766	2.646	2.762	2.841	2.768	2.689	2.830	2.617	
Ca	0.004	0.009	0.031	0.003	0.009	0.003	0.003	0.003	0.002	0.004	0.007	0.027	0.022	0.011	0.029	0.043	0.059	0.021	
K	-	-	-	-	-	-	-	-	-	-	-	-	-	-	-	-	-	-	
Na	-	-	-	-	-	-	-	-	-	-	-	-	-	-	-	-	-	-	
Cr	0.003	0.029	0.005	0.001	0.002	0.019	0.034	0.003	0.000	0.003	0.001	0.008	0.001	0.001	0.003	0.014	0.000	0.002	
Ni	0.012	0.002	0.001	0.003	0.002	0.008	0.006	0.001	0.001	0.002	0.016	0.001	0.000	0.000	0.006	0.002	0.001	0.004	
Mg#	0.940	0.946	0.963	0.942	0.953	0.937	0.946	0.960	0.939	0.949	0.934	0.935	0.962	0.966	0.962	0.943	0.993	0.958	
Fe^{3+}/Fe_T	0.107	0.000	0.314	0.053	0.053	0.045	0.174	0.000	0.000	0.000	0.000	0.000	0.000	0.000	0.286	0.006	0.655	0.117	

Table 4: Representative trace element concentrations (in ppm) of serpentine minerals measured by HR-LA-ICP-MS.

Unit	Upper Platta				Lower Platta					Total p				Tasna			
Sample	Fal 18-06ua23	Fal 18-06ua15	Fal 18-06ua35	Fal 18-06ca6	Mar 18-01ua39	Mar 18-01ua36	Mar 18-01ua46	Mar 18-01ua50	Mar 18-01ca16	Tot 19-02vb6	Tot 19-02ca_49	Tot 19-02ca_50	Tot 19-07cb25	Tas 19-02ub1	Tas 19-03ub21	Tas 19-02ub8	Tas 19-08cb6
Texture	mesh (S1)	bastite (S1)	lamellar vein (S4)	crack-seal (S5)	mesh (S1)	bastite (S1)	banded vein (S3)	lamellar vein (S4)	crack-seal (S5)	mesh (S1)	relic cpx	spherical vein (S2)	banded vein (S3)	mesh (S1)	bastite (S1)	lamellar vein (S4)	banded vein (S3)
Type	lizardite	lizardite	antigorite	chrysotile	lizardite	lizardite opx	lizardite	antigorite	chrysotile	lizardite	lizardite	polyhedral	polygonal	lizardite	lizardite	antigorite	lizardite
Primary minerals	ol	opx	-	-	ol	-	-	-	-	ol	cpx	-	-	ol	cpx	-	-
Li	2.85	13.79	11.15	13.71	3.98	2.71	4.96	2.54	12.32	0.21	3.90	2.24	1.66	7.33	26.9	6.13	0.36
B	48.3	36.6	94.5	37.9	43.6	30.9	34.9	37.3	35.3	19.4	15.2	18.5	46.7	25.1	52.7	23.7	15.9
V	5.89	76.84	10.23	4.37	17.2	85.5	17.3	29.3	9.75	6.56	163.7	7.06	7.79	112	129	18.2	18.3
Cr	136	3465	2.12	304	554	4809	358	38.2	253	8.76	2853	32.82	78.57	2665	4054	44.0	75.0
Co	111	14.6	6.68	43.83	73.6	52.5	9.36	11.0	8.97	162	10.8	1.27	2.19	56.9	53.0	35.9	147.

														6	0		6
Ni	2951	1019	210.4	708.5	1977	1053	188	224	233	2987	179.8	16.57	20.4	1663	909	1222	2897
Zn	19.2	24.3	19.0	18.2	59.1	65.9	52.2	69.0	38.8	22.0	9.7	7.11	5.47	26.8	35.0	24.2	21.4
As	2.85	0.15	1.33	0.95	1.67	1.06	0.10	0.22	0.19	n.d	0.13	0.13	0.06	0.09	0.06	<0.05	0.04
Rb	0.10	0.18	1.51	0.17	0.75	0.38	0.56	1.35	1.07	0.07	0.03	0.05	0.19	0.51	1.61	1.48	0.01
Sr	1.99	5.39	1.25	3.16	4.10	3.09	2.88	2.05	4.22	1.90	17.43	0.62	4.93	3.29	2.16	1.56	1.26
Y	0.37	2.00	0.14	0.32	0.28	0.18	0.20	0.11	0.34	0.43	12.85	0.14	0.42	1.36	1.28	0.85	0.78
Zr	0.11	3.95	0.07	0.30	0.12	0.09	0.12	0.24	0.11	0.53	10.81	0.26	1.96	0.25	0.77	0.37	0.46
Nb	0.02	0.03	0.01	0.02	0.10	0.09	0.07	0.04	0.06	0.00	0.01	0.00	0.00	0.02	0.01	0.01	0.00
Cs	0.28	0.54	5.00	0.16	0.55	0.33	0.46	1.38	0.72	n.d	0.01	0.01	0.05	1.11	1.40	4.29	0.00
Ba	0.81	3.47	0.59	1.28	1.22	0.86	0.74	0.55	1.15	0.10	0.14	0.09	0.63	0.99	0.36	0.91	0.20
La	0.06	0.06	0.04	0.05	0.30	0.15	0.15	0.07	0.13	0.01	0.11	0.00	0.01	0.03	0.00	0.02	0.00
Ce	0.20	0.25	0.14	0.14	0.40	0.31	0.29	0.15	0.23	0.06	0.77	0.01	0.03	0.08	0.02	0.07	0.01
Pr	0.03	0.04	0.02	0.03	0.04	0.03	0.03	0.01	0.02	0.01	0.21	0.00	0.01	0.01	0.01	0.01	0.00
Nd	0.15	0.23	0.12	0.14	0.14	0.09	0.11	0.04	0.09	0.07	1.60	0.03	0.04	0.10	0.07	0.06	0.05
Sm	0.04	0.12	0.03	0.05	0.03	0.03	0.01	0.01	0.02	0.03	0.87	0.01	0.02	0.05	0.06	0.03	0.04
Eu	0.06	0.05	0.04	0.08	0.09	0.05	0.05	0.03	0.08	0.01	0.35	0.01	0.01	0.02	0.04	0.02	0.01
Gd	0.07	0.23	0.03	0.08	0.03	0.02	0.02	0.01	0.04	0.04	1.39	0.03	0.04	0.11	0.12	0.10	0.09
Tb	0.01	0.05	0.00	0.02	0.00	0.00	0.00	0.00	0.01	0.01	0.30	0.01	0.01	0.03	0.03	0.02	0.02
Dy	0.06	0.35	0.02	0.07	0.03	0.02	0.02	0.02	0.04	0.06	2.16	0.02	0.07	0.23	0.20	0.13	0.11
Ho	0.01	0.08	0.00	0.01	0.01	0.01	0.00	0.00	0.01	0.01	0.48	0.01	0.02	0.06	0.05	0.03	0.03
Er	0.03	0.25	0.01	0.03	0.02	0.01	0.01	0.01	0.02	0.05	1.47	0.02	0.05	0.19	0.14	0.10	0.10
Tm	0.00	0.04	0.00	0.01	0.00	0.00	0.00	0.00	0.01	0.01	0.22	0.00	0.01	0.02	0.03	0.02	0.01

Yb	0.02	0.30	0.01	0.03	0.04	0.02	0.02	0.01	0.03	0.06	1.44	0.01	0.07	0.19	0.21	0.09
Lu	0.00	0.05	0.00	0.01	0.01	0.00	0.00	0.00	0.01	0.01	0.21	0.01	0.01	0.03	0.04	0.02	0.02
Hf	<0.003	0.15	<0.003	0.00	0.00	<0.002	0.00	0.00	0.00	0.02	0.45	0.01	0.06	0.03	0.05	0.03	0.03
Ta	<0.001	0.00	<0.001	0.01	0.00	0.00	0.00	0.00	0.00	<0.0002	0.00	<0.002	0.00	<0.0010	<0.0006	<0.00008	<0.002
Pb	0.26	0.02	<0002	0.06	0.52	0.17	0.01	0.01	0.04	0.14	0.06	0.04	0.14	0.07	0.05	0.01	0.03
Th	0.00	0.01	0.00	0.00	0.00	0.00	0.00	0.00	0.00	0.00	0.00	0.00	0.00	0.00	0.00	0.00	0.00
U	0.00	0.00	<0.001	0.01	0.00	0.00	0.00	0.00	0.00	0.00	0.00	<0.0002	0.00	0.00	0.00	0.01	0.00

Fig. 1.

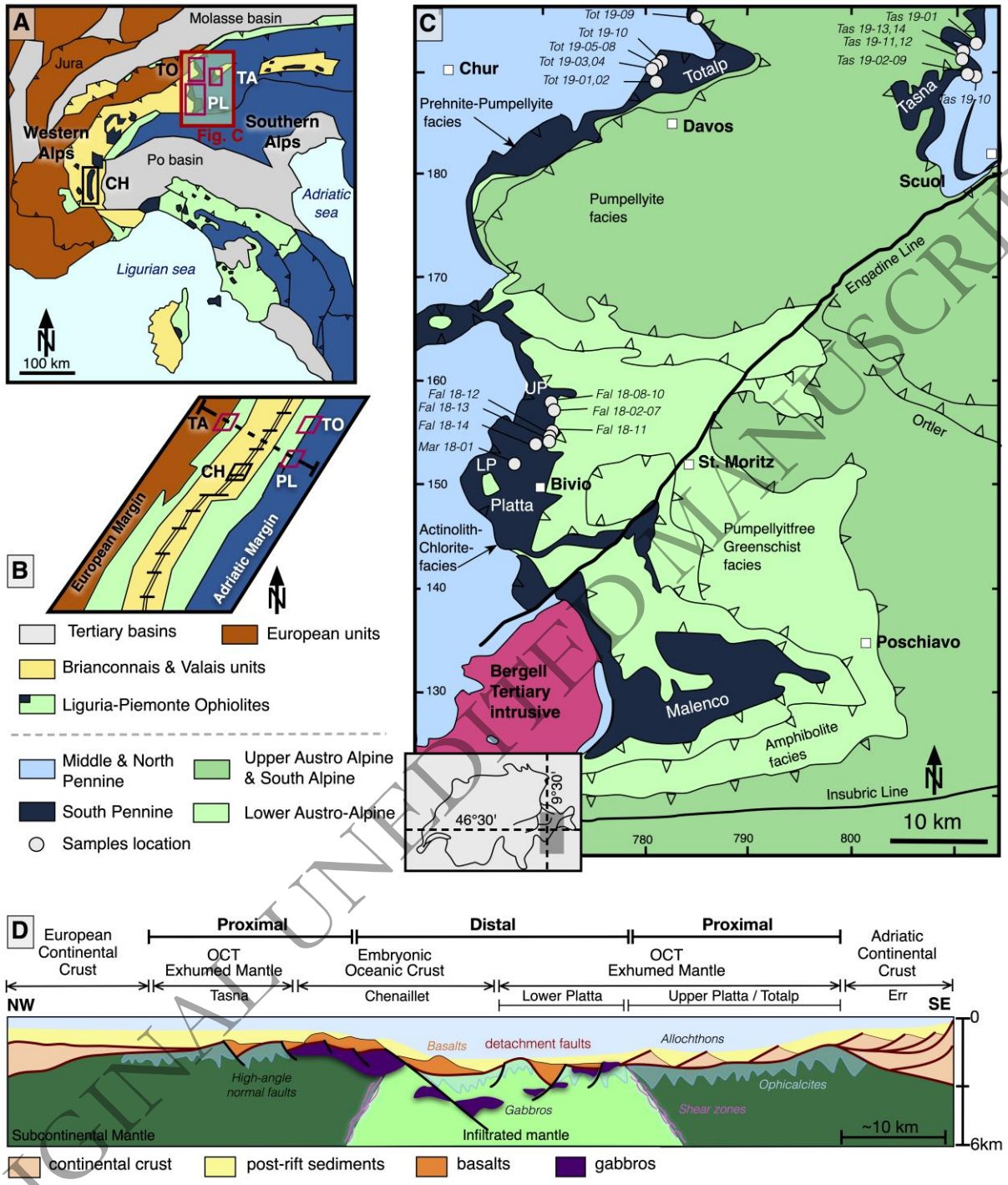

1663 **Fig. 2.**

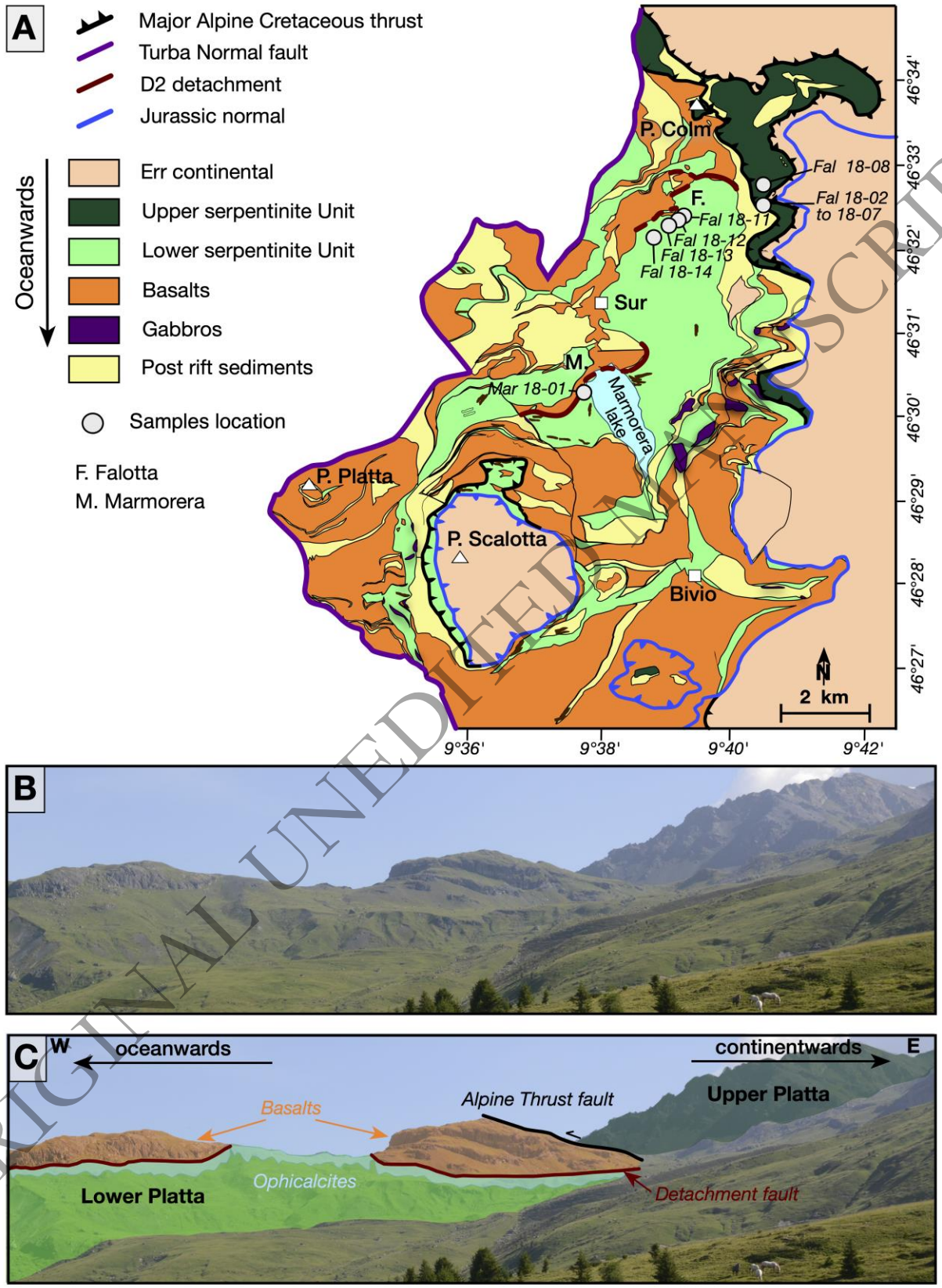

1664

1665

1666 **Fig. 3.**

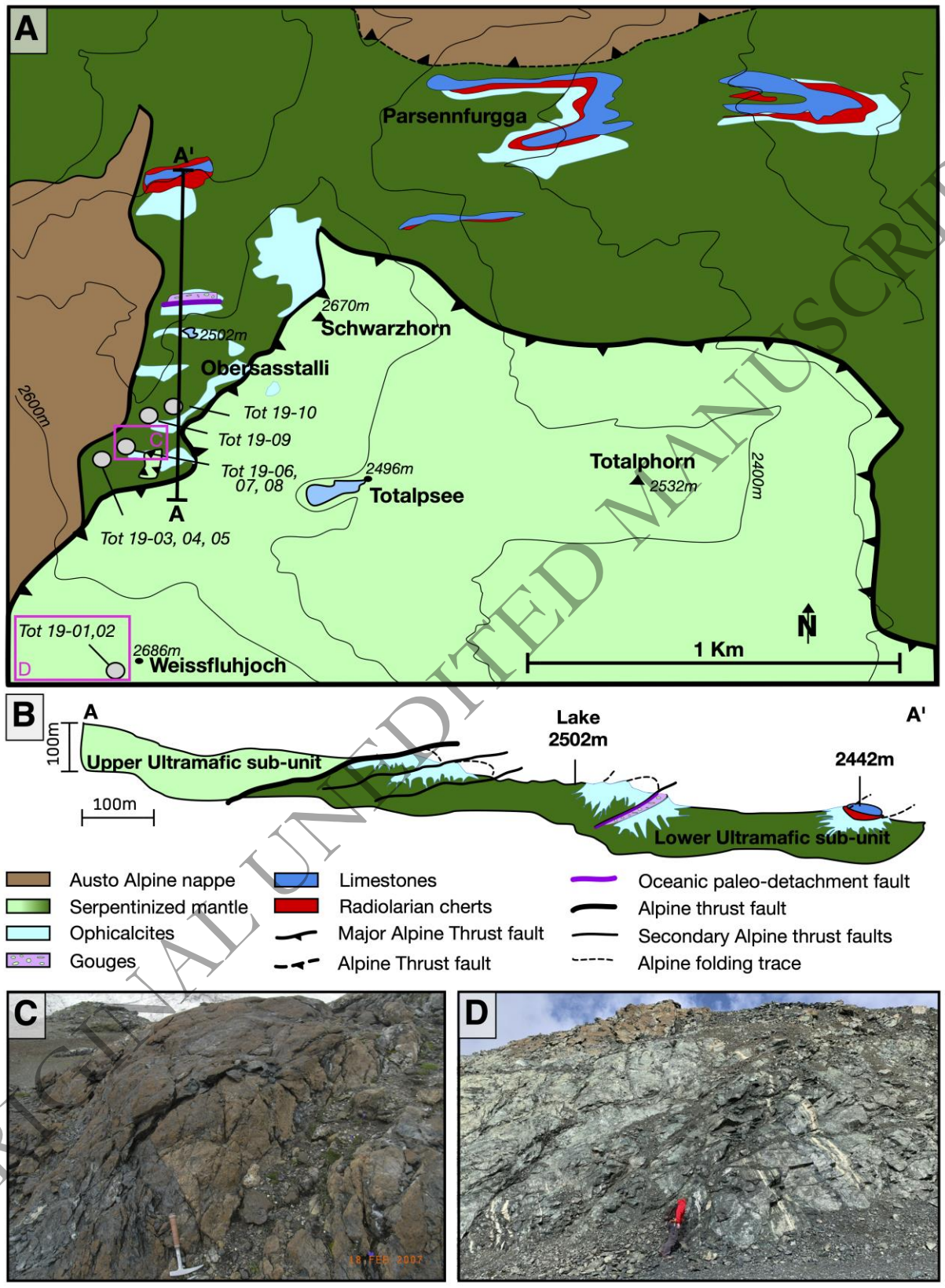

1667

1668

1669

1670 **Fig. 4.**

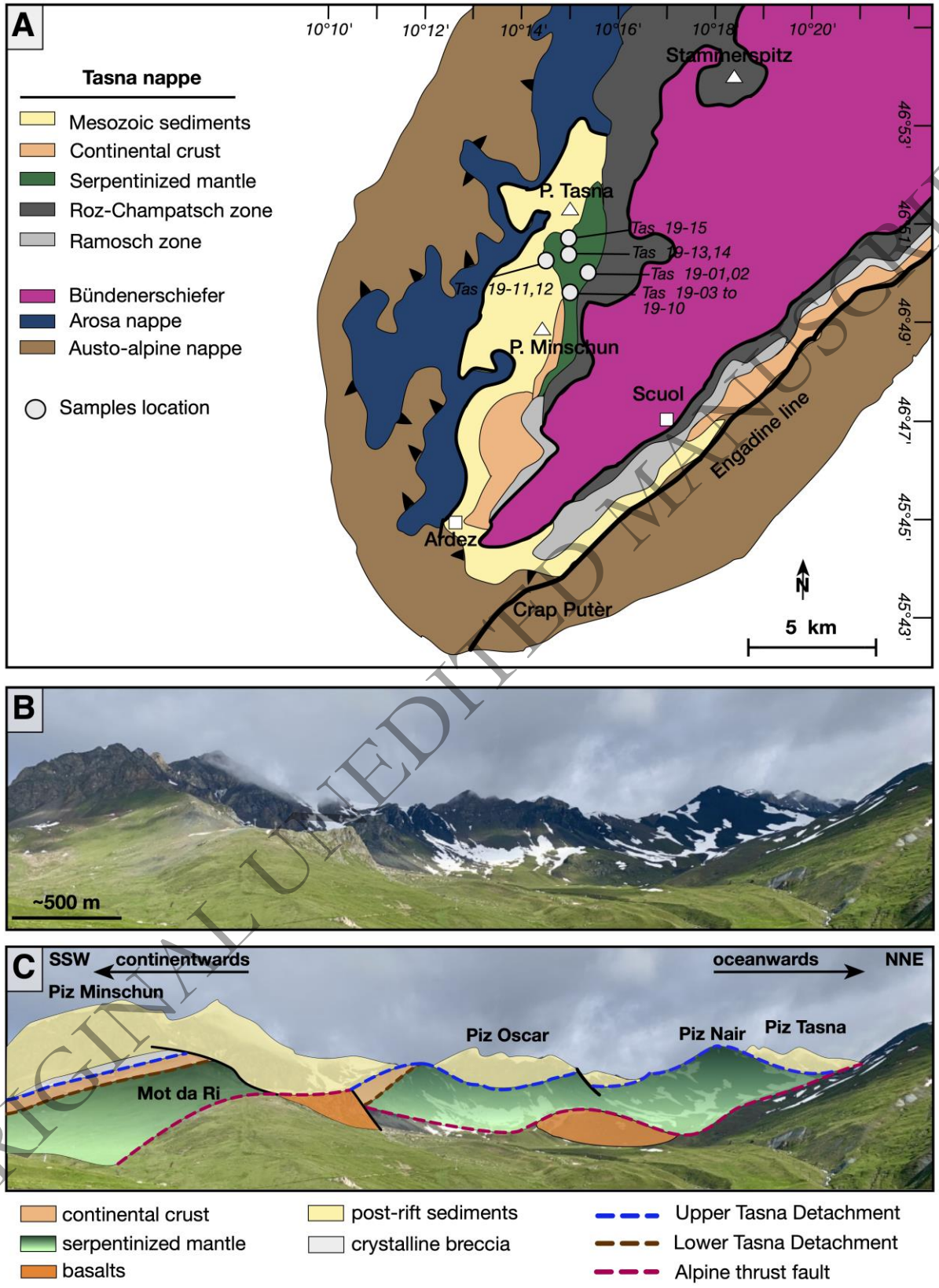

1671

1672

1673

1674 **Fig. 5.**

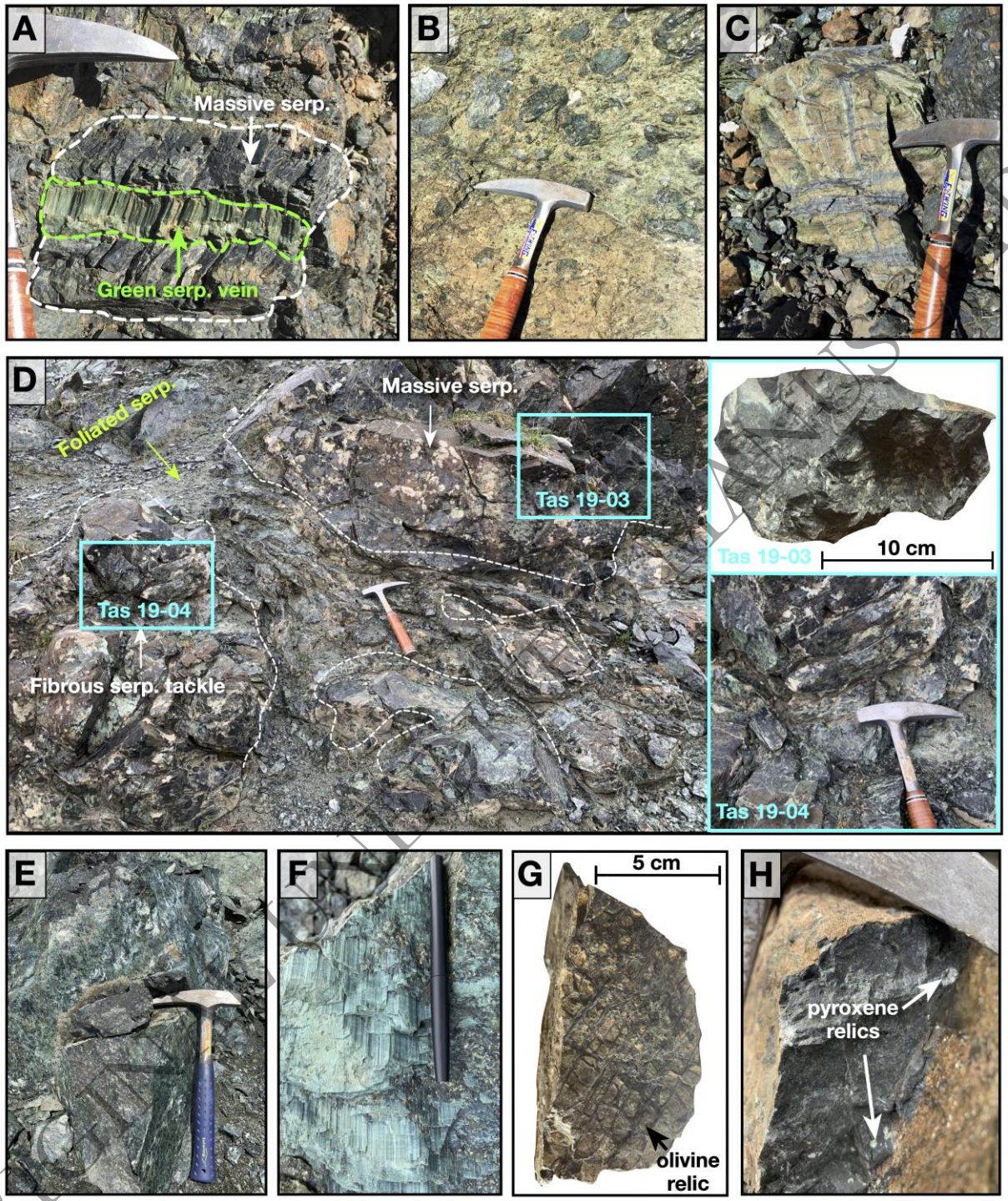

1675

1676

1677

1678

1679

1680 **Fig. 6.**

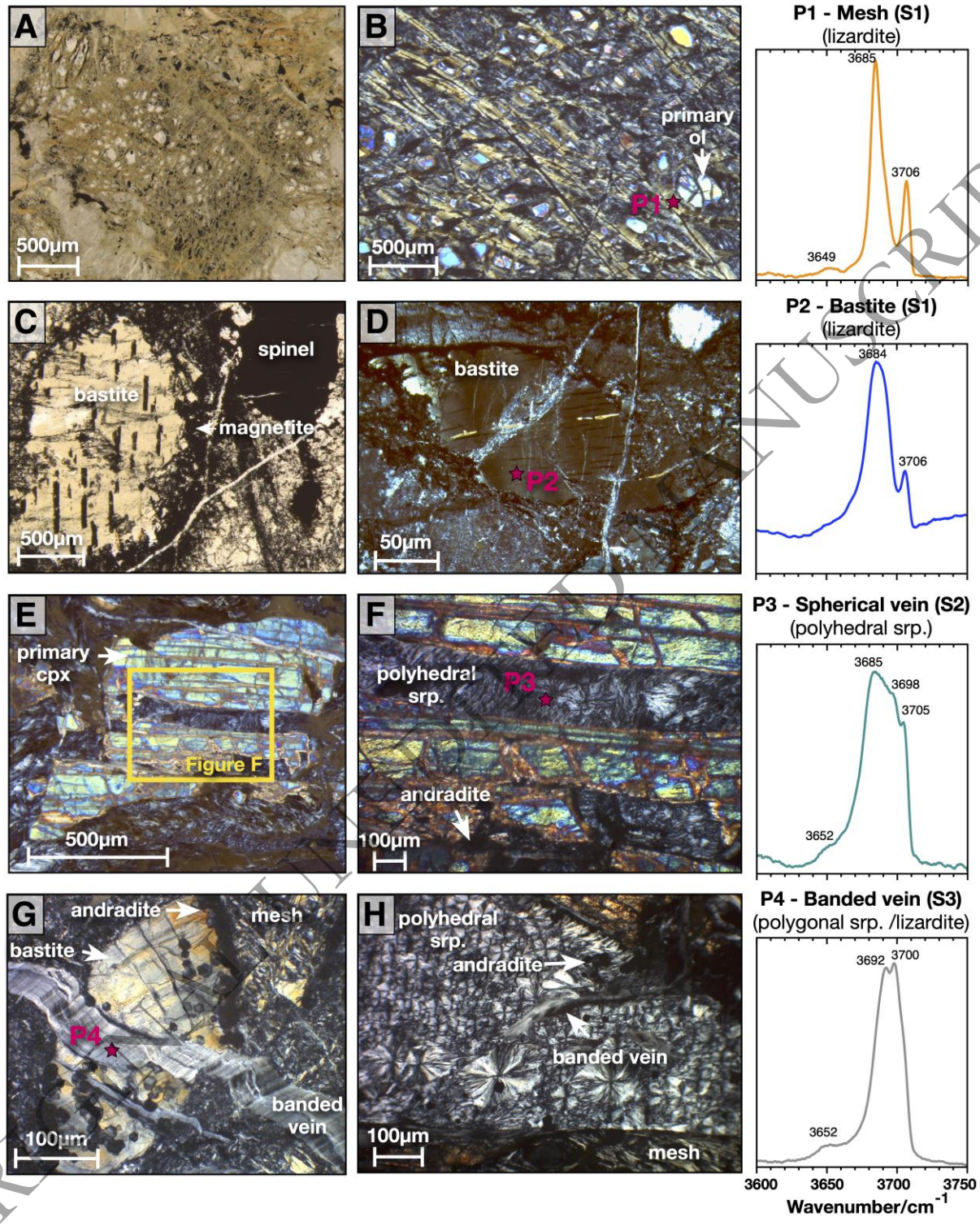

1681

1682

1683

1684

1685 **Fig. 7.**

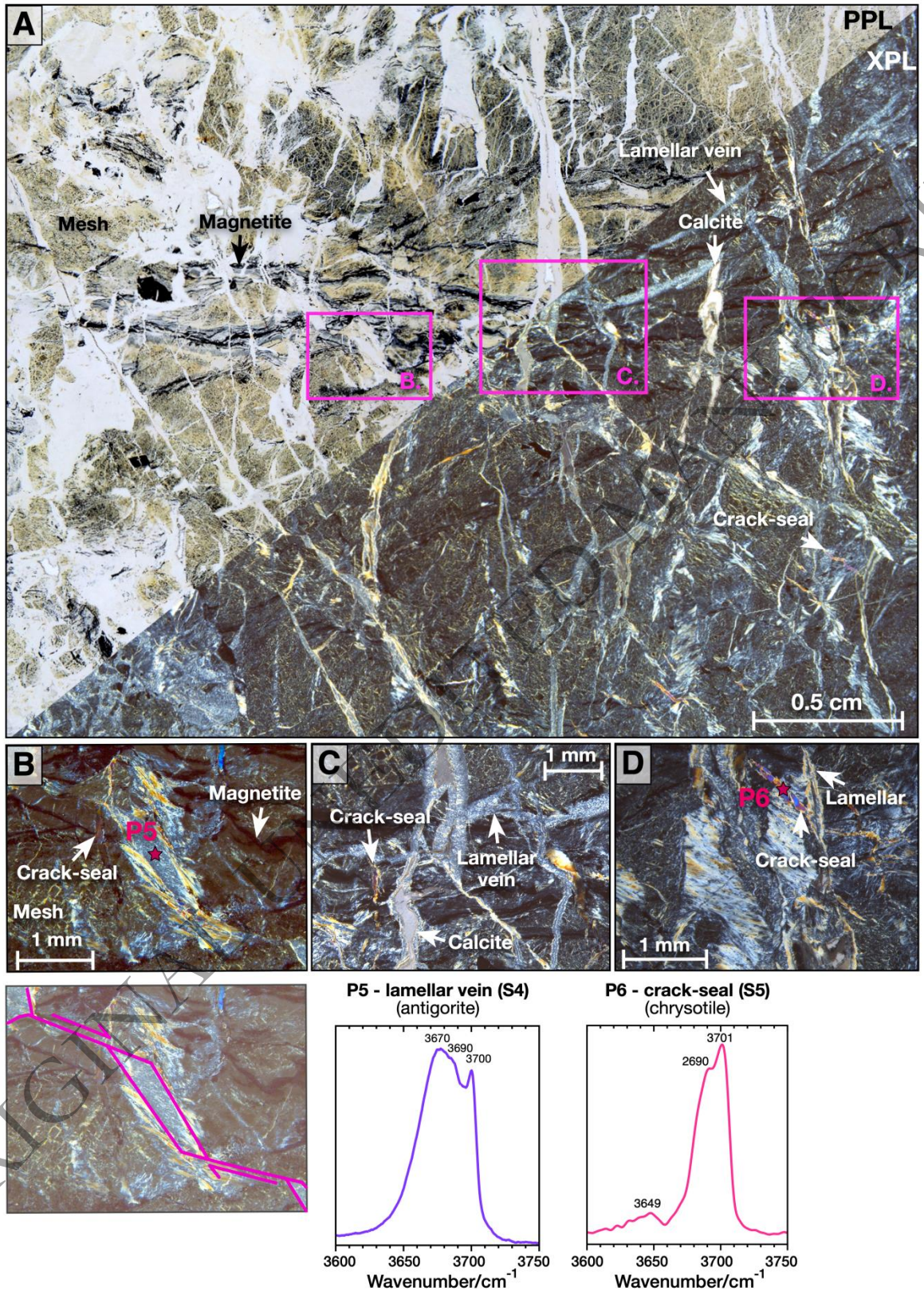

1686

1687

1688

1689 **Fig. 8.**

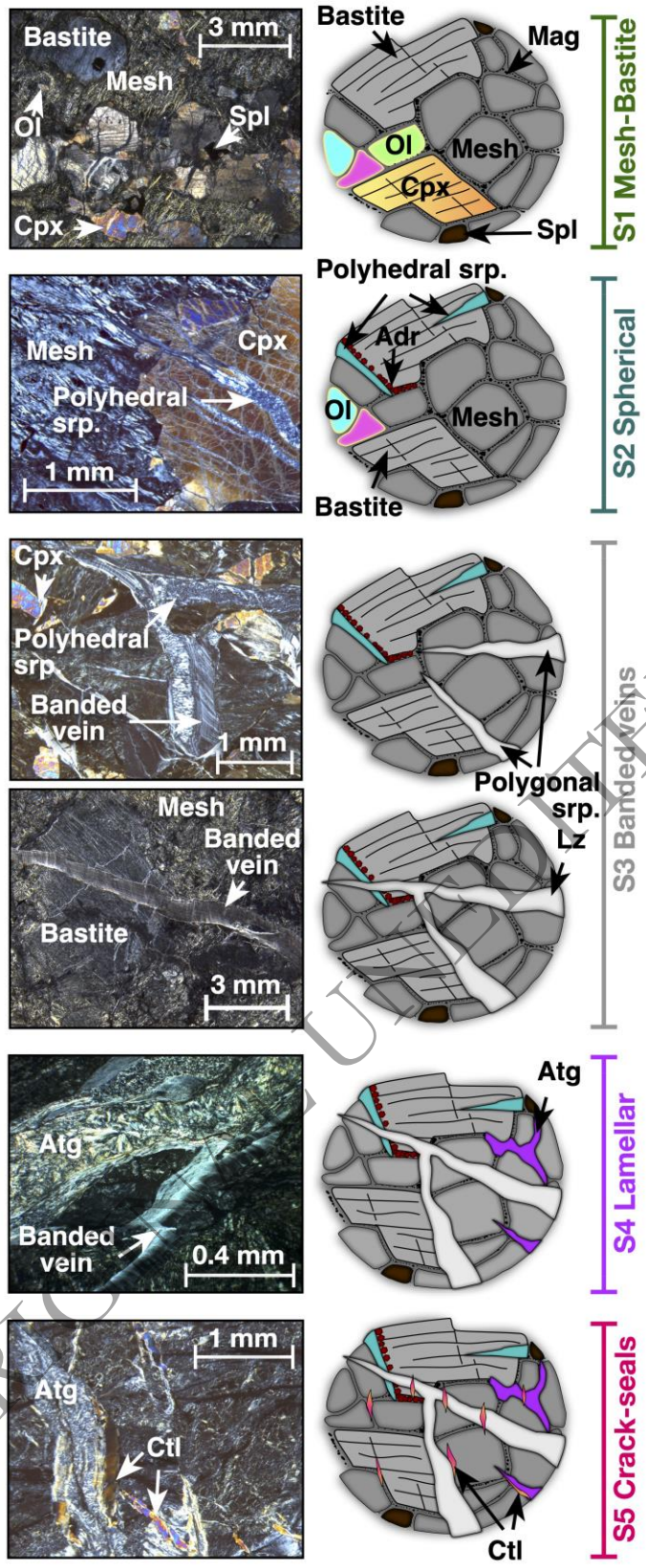

1690

1691

1692 **Fig. 9.**

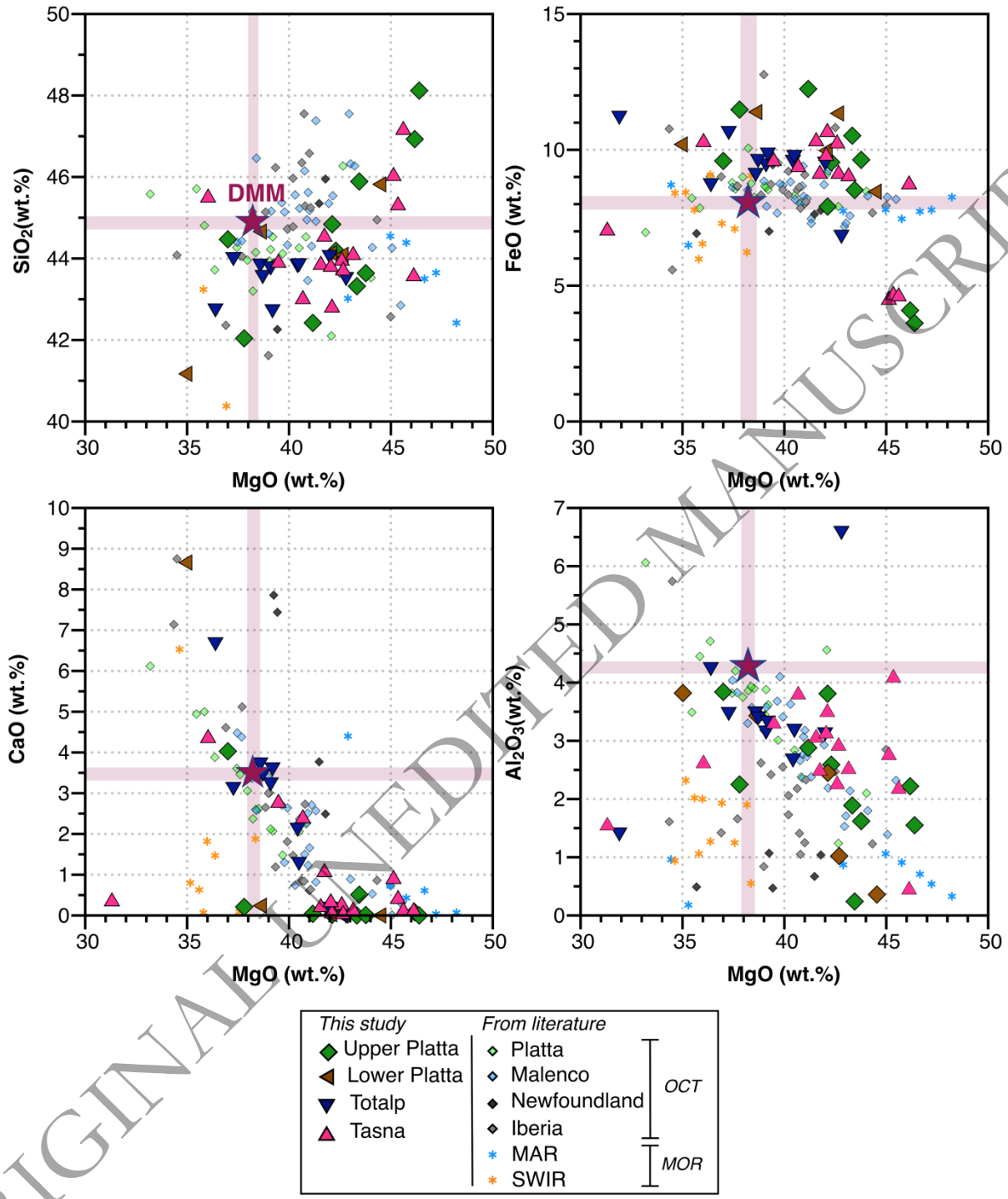

1693

1694

1695

1696

1697

Fig. 10.

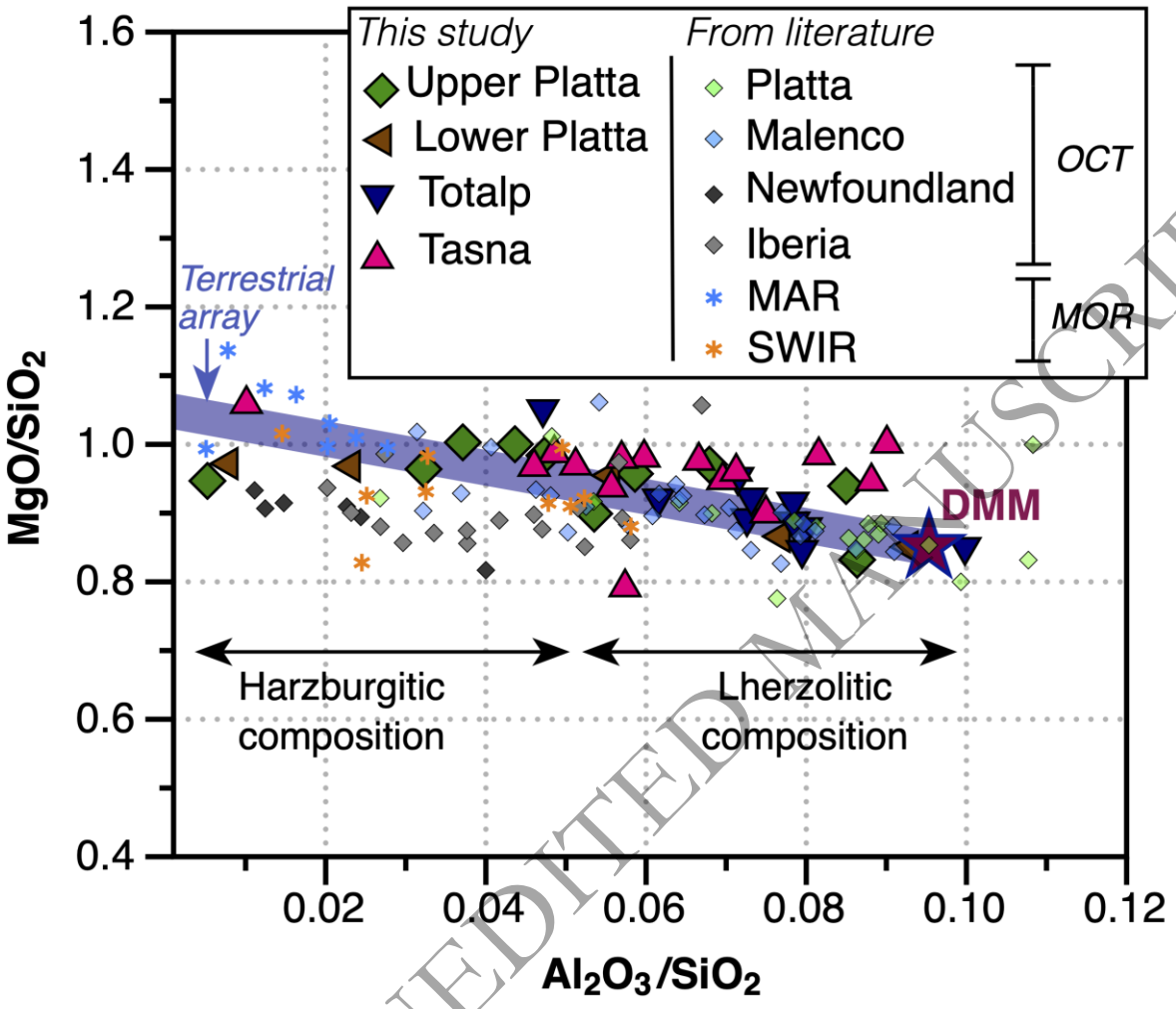

1710 **Fig. 11.**

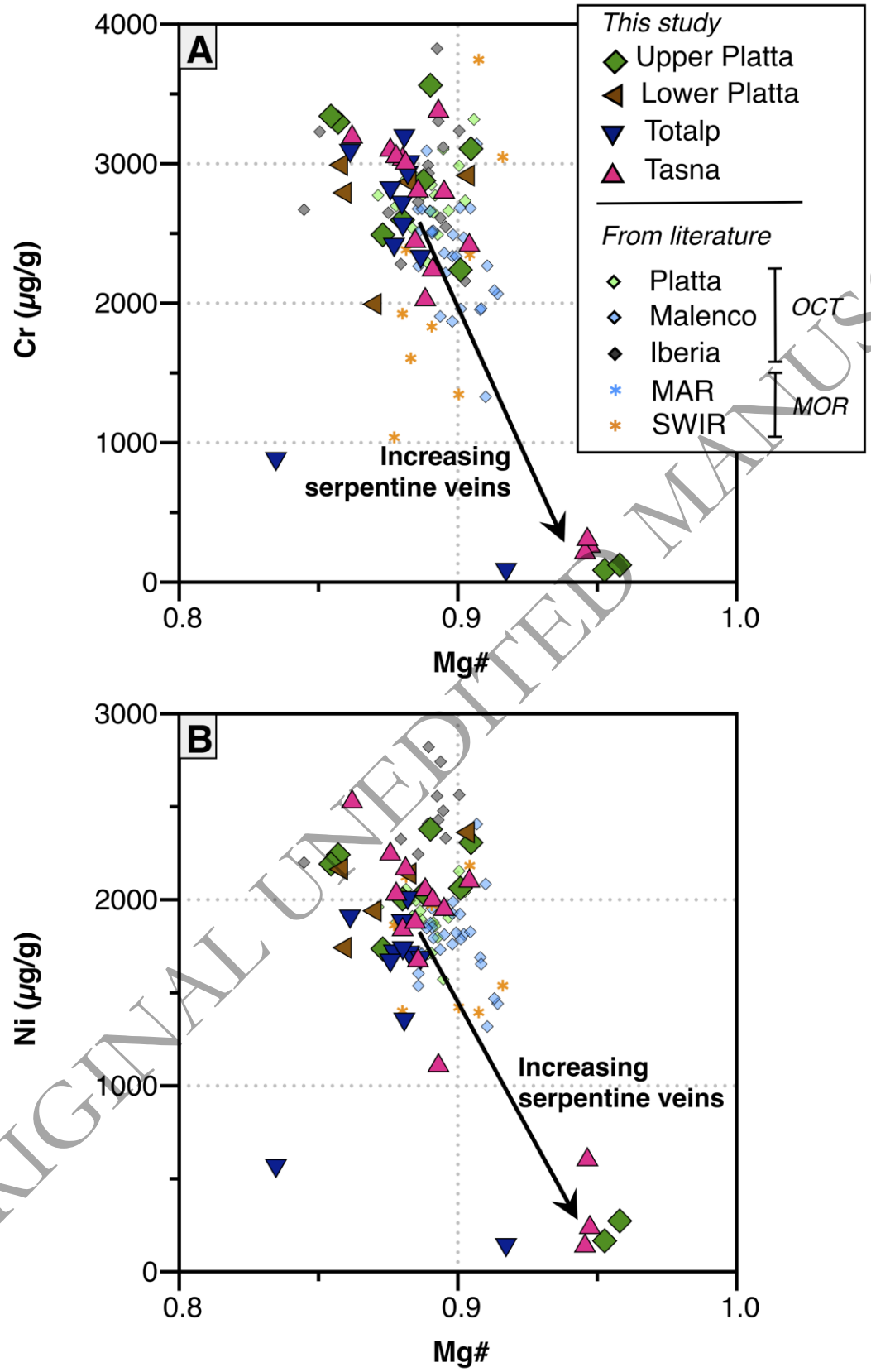

1711

1712

Fig. 12.

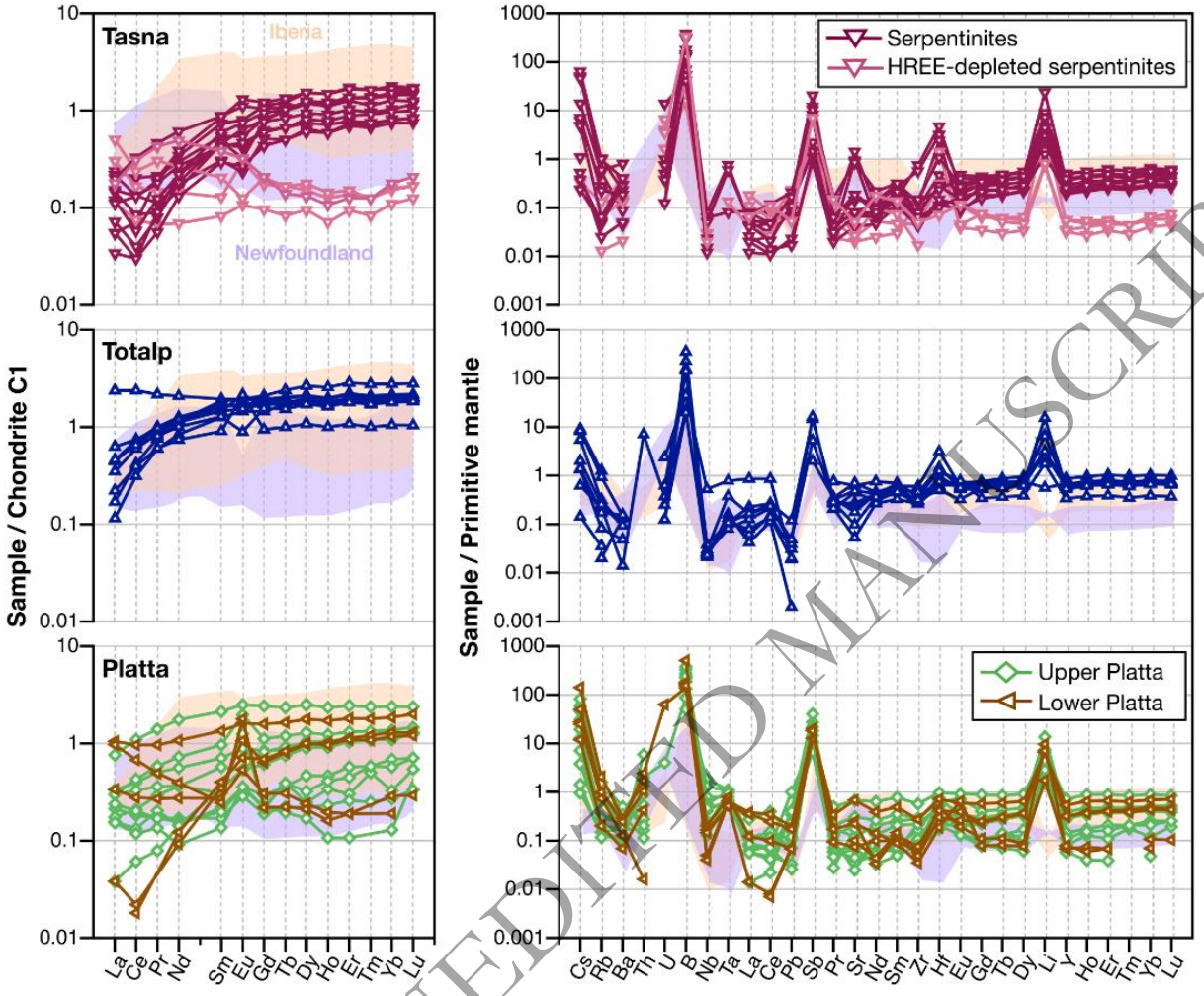

1725 **Fig. 13.**

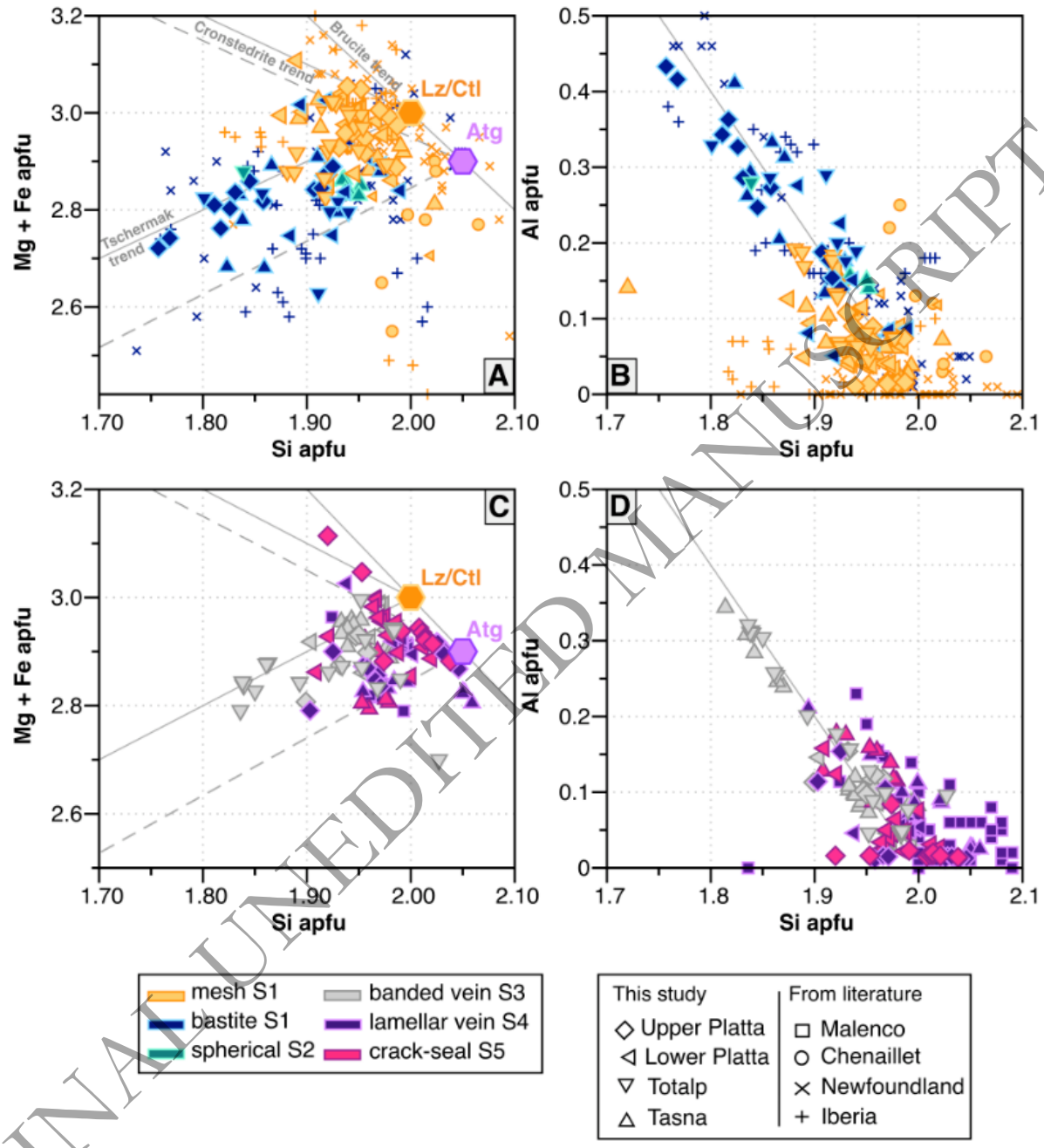

1726

1727

1728

1729

1730

1731

1732

1733 **Fig. 14.**

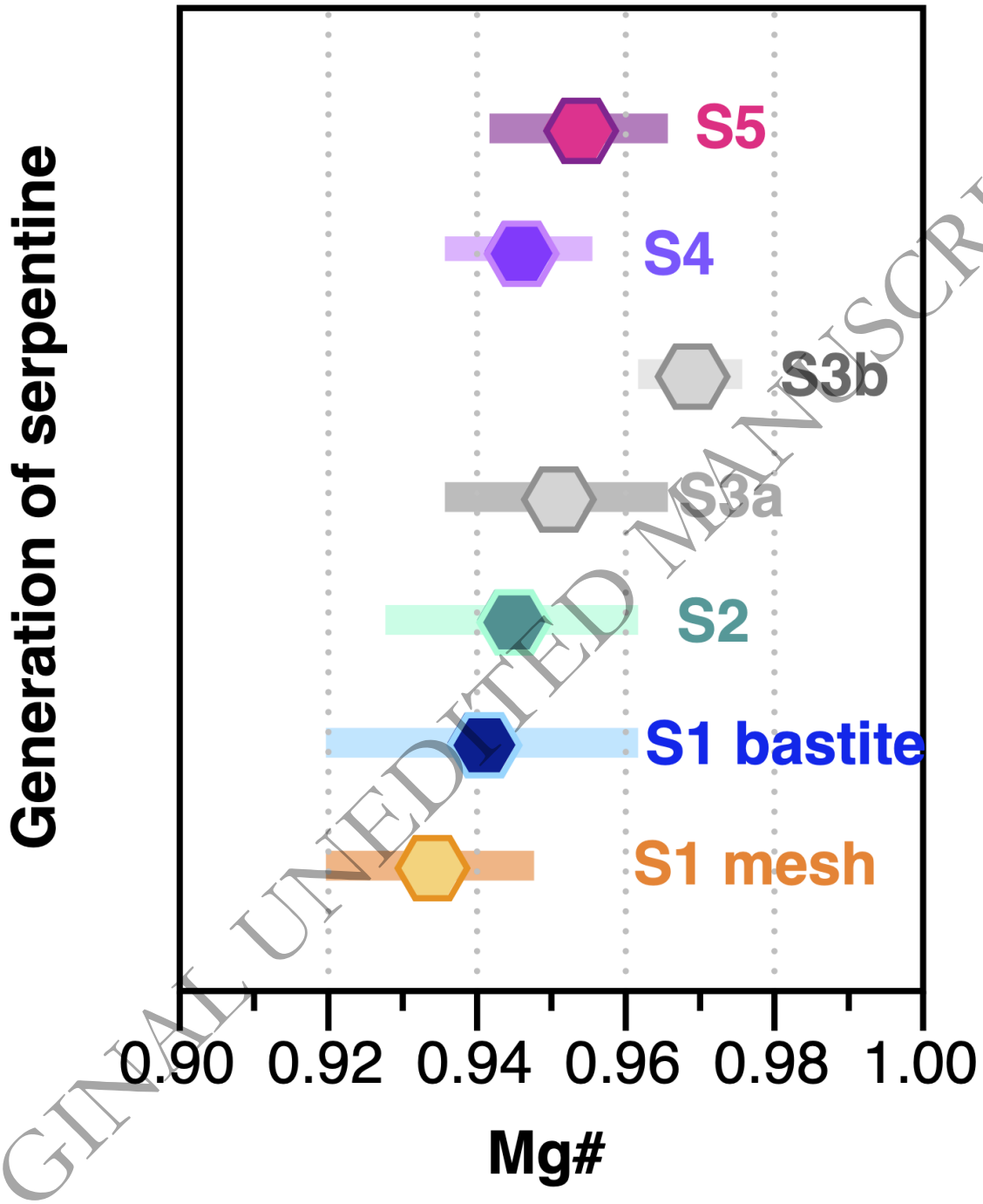

1734

1735

1736

1737

1738

1739 **Fig. 15.**

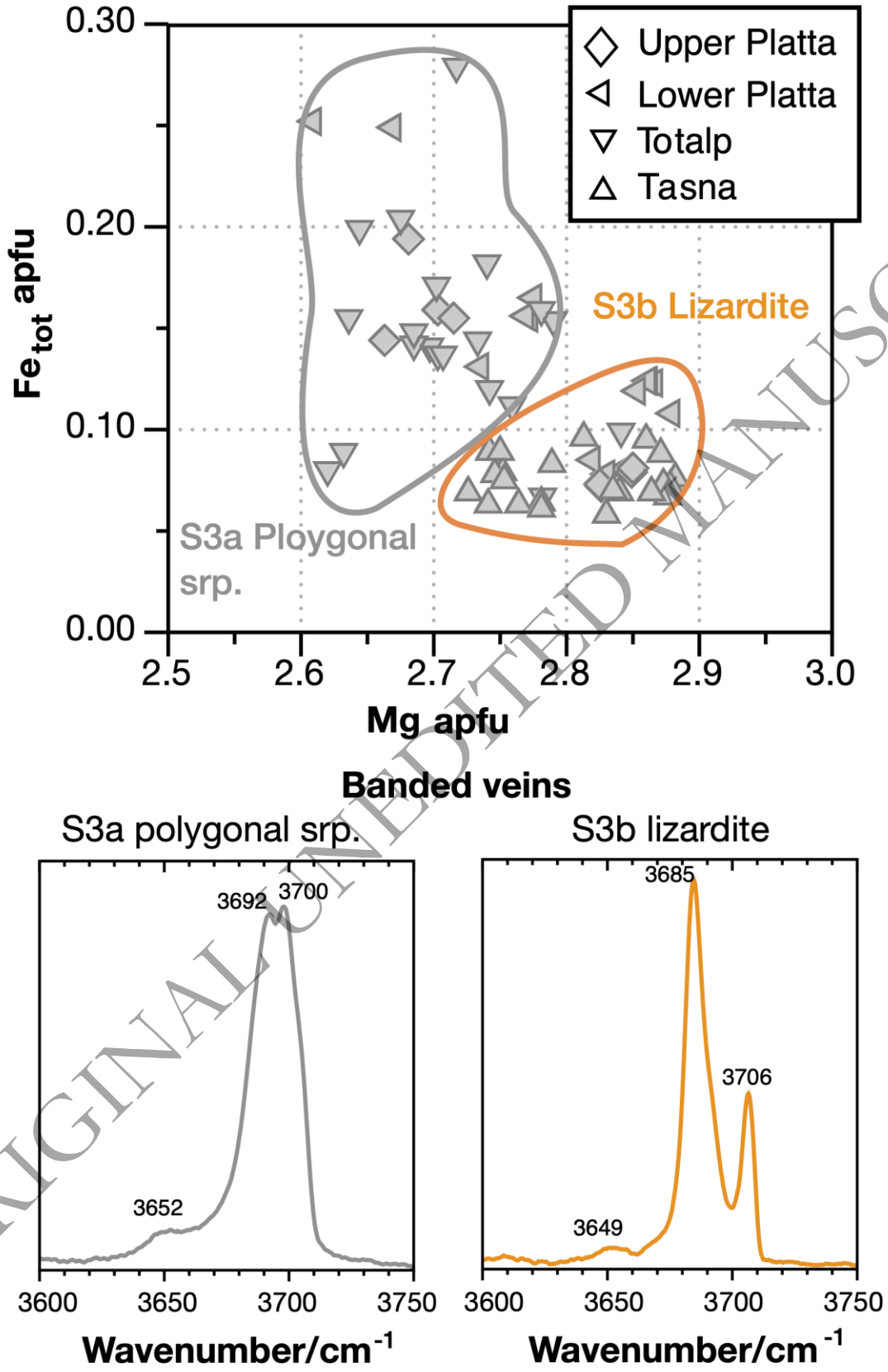

1740

1741

1742 **Fig. 16.**

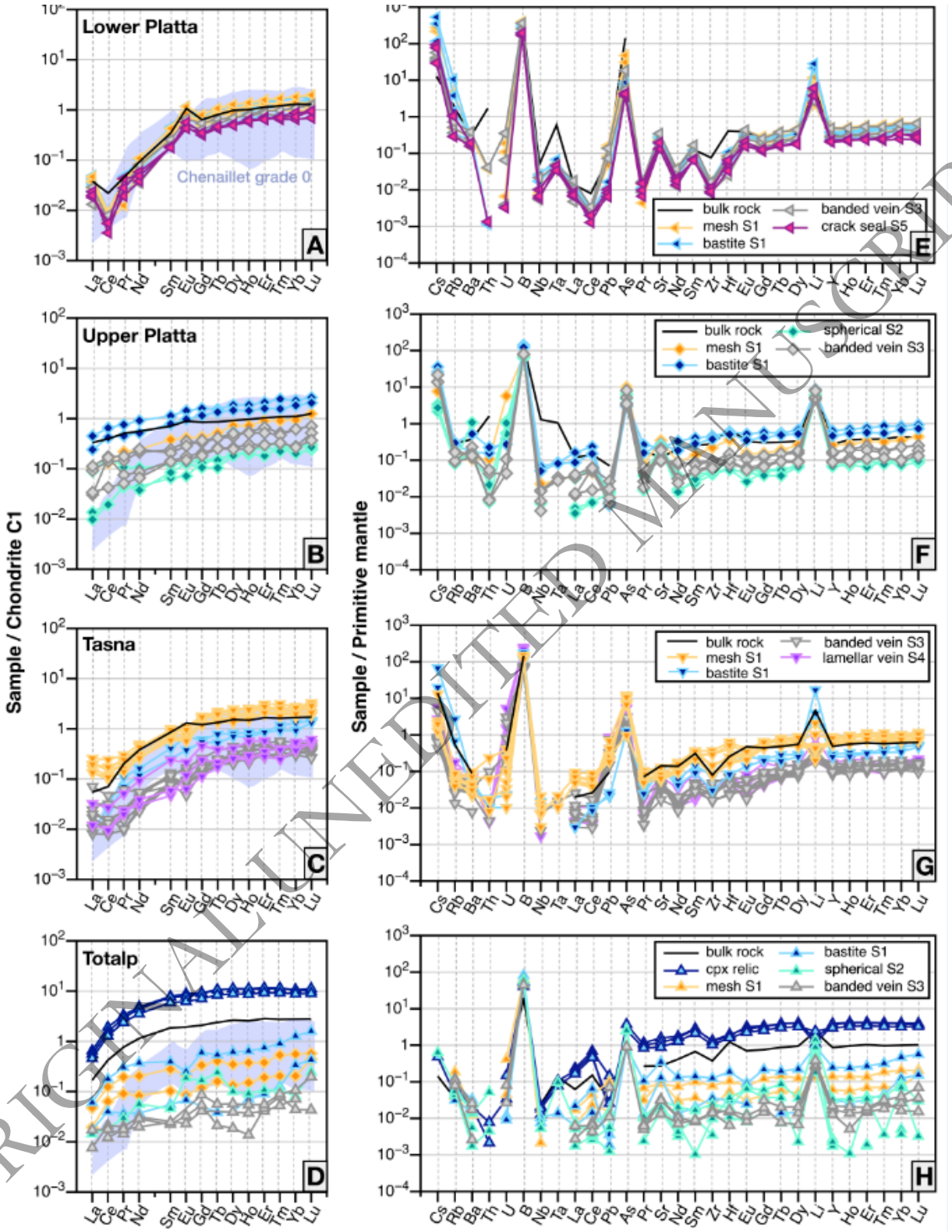

1743

1744

1745

1746

Fig. 17.

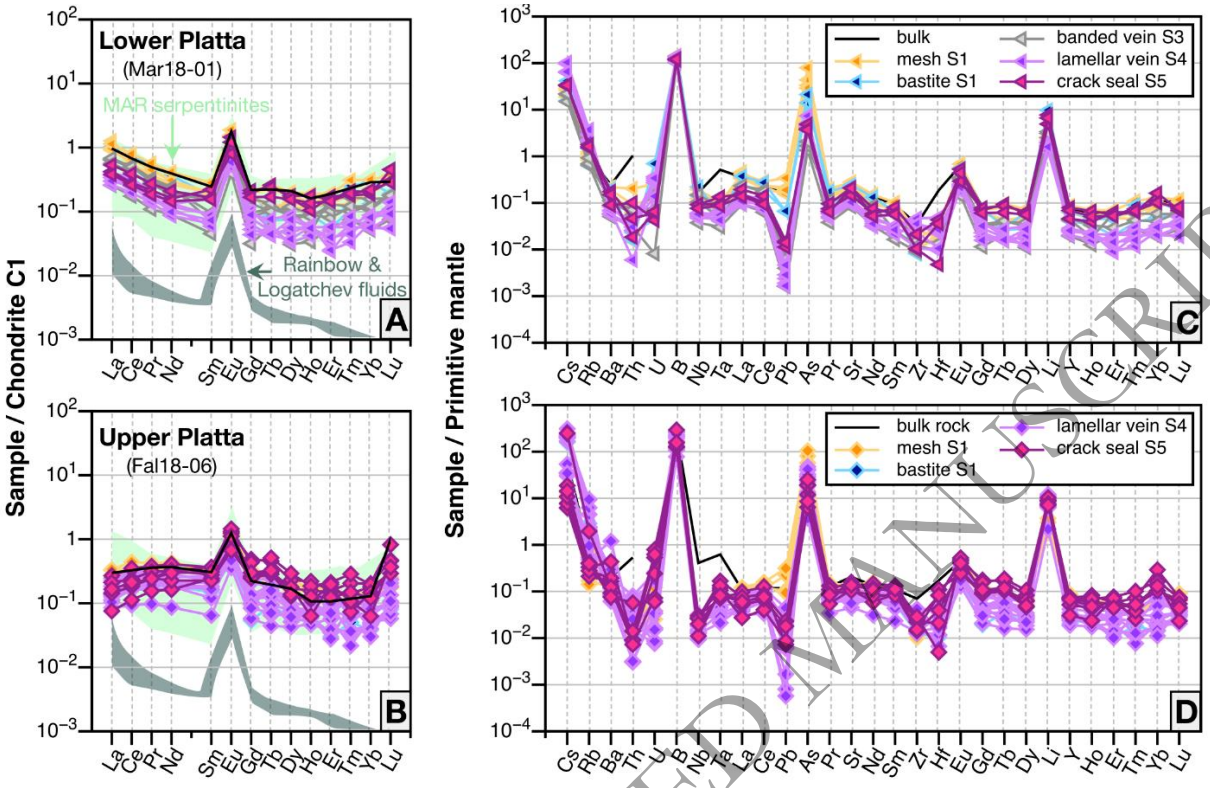

1762 **Fig. 18.**

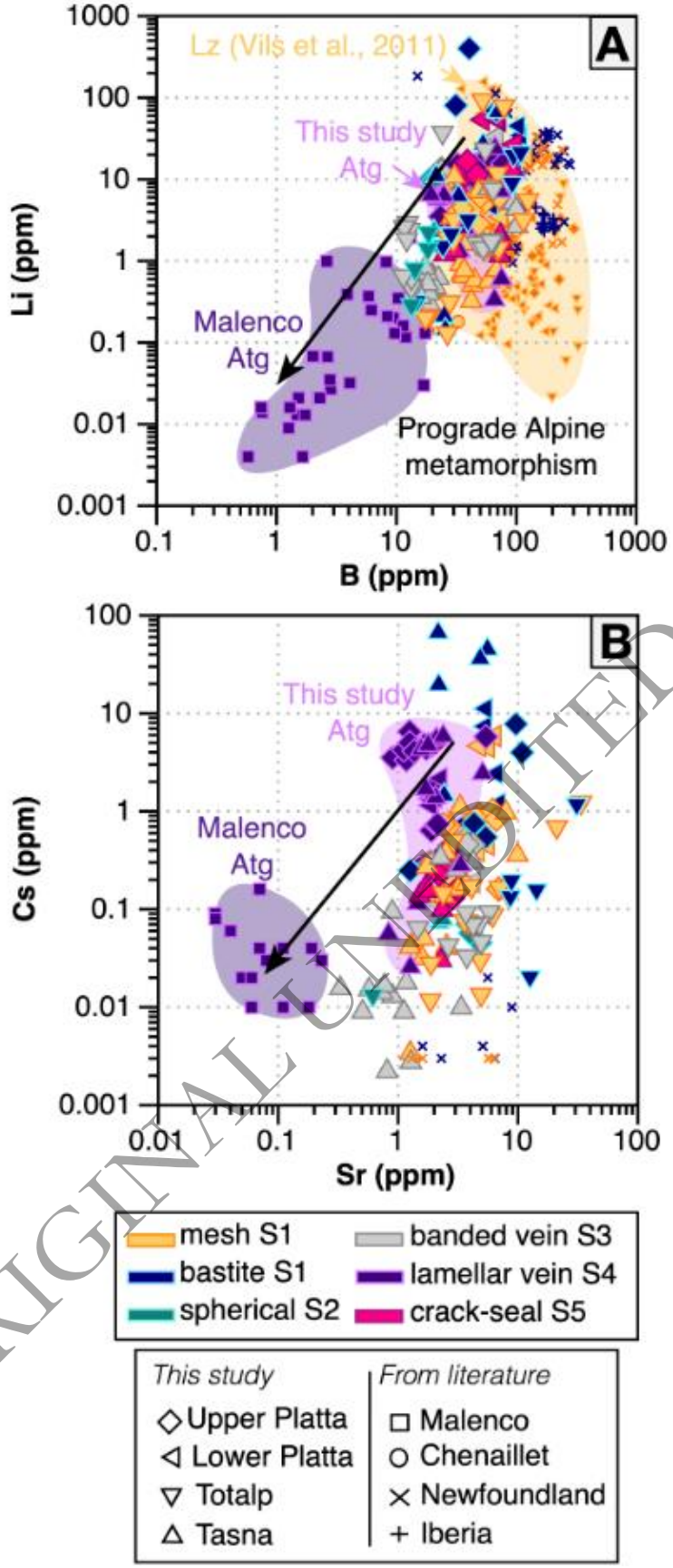

1763

1764 **Fig. 19.**

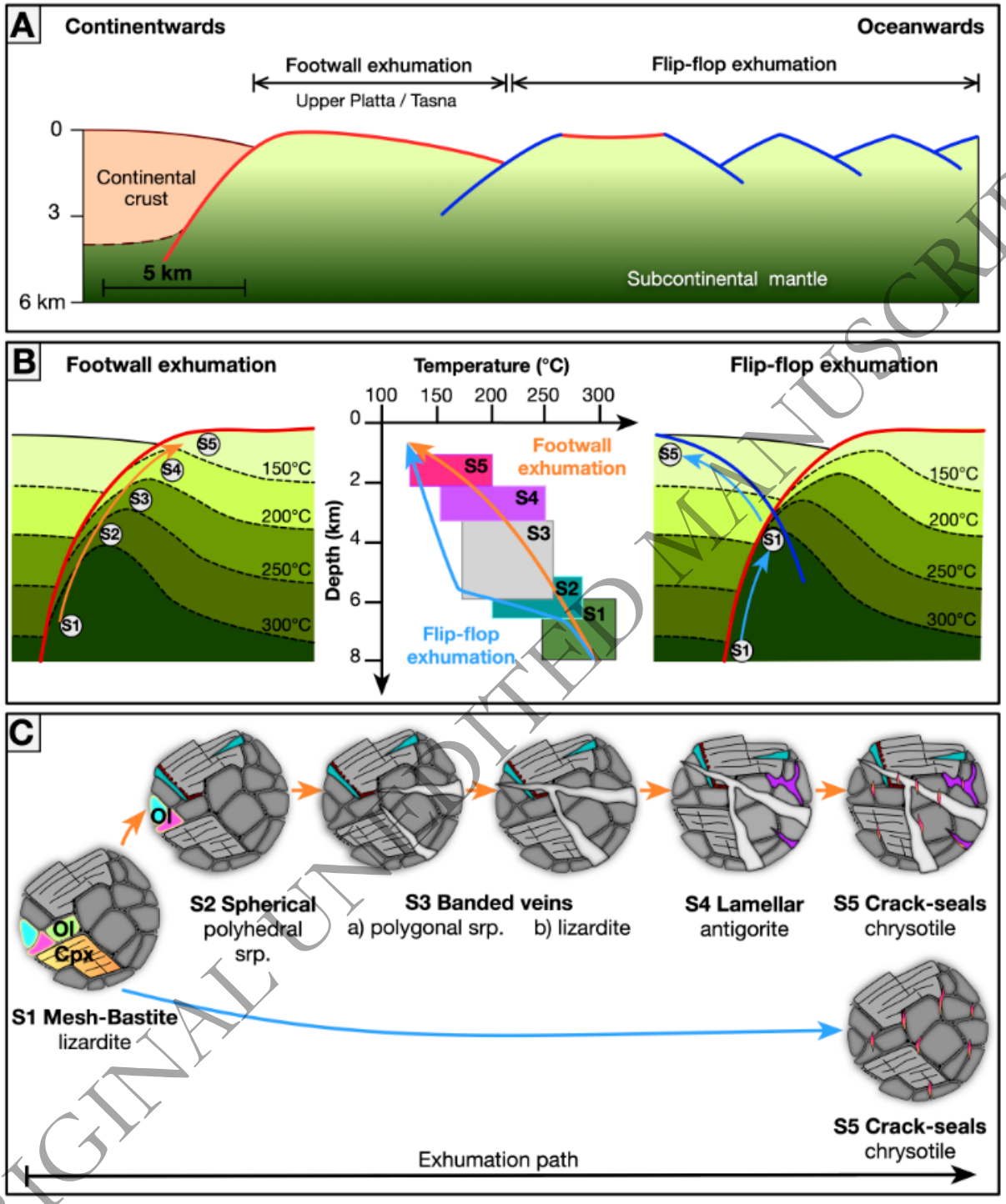

1765

Deltech Furnaces

Sustained operating temperatures to 1800° Celsius

www.deltechfurnaces.com

Gas Mixing System

An ISO 9001:2015 certified company

Custom Vertical Tube

ASME NQA-1 2008 Nuclear Quality Assurance

Standard Vertical Tube

Control systems are certified by Intertek UL508A compliant

Bottom Loading Vertical Tube